SANDIA REPORT
SAND20XX-XXXX
Printed Click to enter a date

Sandia National Laboratories

Big Hill Geomechanical Analysis Using M-D Viscoplastic Material Model

Byoung Yoon Park

Prepared by
Sandia National Laboratories
Albuquerque, New Mexico 87185 and Livermore, California 94550

Issued by Sandia National Laboratories, operated for the United States Department of Energy by National Technology & Engineering Solutions of Sandia, LLC.

Available to DOE and DOE contractors from

U.S. Department of Energy

Office of Scientific and Technical Information

P.O. Box 62

Oak Ridge, TN 37831

Telephone: (865) 576-8401

Facsimile: (865) 576-5728

E-Mail: reports@osti.gov

Online ordering: http://www.osti.gov/scitech

Available to the public from

U.S. Department of Commerce

National Technical Information Service

5301 Shawnee Rd

Alexandria, VA 22312

Telephone: (800) 553-6847

Facsimile: (703) 605-6900

E-Mail: orders@ntis.gov

Online order: https://classic.ntis.gov/help/order-methods/

ABSTRACT

The integrity of wellbores at the interbed between the caprock and salt is a serious concern in the Big Hill site. For the remediation and life extension of wellbores, more accurate predictions from the global model are needed. The Big Hill global model is improved using the M-D viscoplastic contact surface model and the mesh containing the interbed layer with contact surfaces between the salt and caprock layers, and fault blocks in overburden and caprock layers. The model calibration has been performed based on the cavern volumetric closures obtained from the Caveman calculations. The results agree well from 1991 to the early 2000s. The difference starts to widen after that, it might be because of frequent fluid movement and raw water injection. Therefore, the predictions from this improved model could be used to examine the structural integrity of caverns in Big Hill salt dome.

ACKNOWLEDGEMENTS

This research is funded by SPR programs administered by the Office of Fossil Energy of the U.S. Department of Energy.

The author would like to thank Steven R. Sobolik, and Anna C. Snider Lord of Sandia provided technical reviews and valuable comments. Barry Roberts and David Hart of Sandia provided the seismic and sonar data for meshing the dome and caverns; and the wellhead and oil-brine interface depth data, respectively. Sandia department manager Donald Conley and SPR project manager Anna C. Snider Lord who supported this work. As always, the support of Diane Willard of DOE is greatly appreciated. Paul Malphurs of DOE also is greatly appreciated, as is his comprehensive review of this report. This report has been improved by these individuals.

CONTENTS

LIST OF FIGURES

LIST OF TABLES

This page left blank

EXECUTIVE SUMMARY

The integrity of wellbores at the interbed between the caprock and salt is a serious concern at the Big Hill (BH) site. For the remediation and life extension of wellbores, more accurate predictions from the global model are needed. This simulation uses the multi-mechanism deformation (M-D) viscoplastic model as a salt constitutive model. The original M-D model considers three separate steady-state creep mechanisms and an overlying transient creep mechanism. Recent efforts by Reedlunn [2016; 2018] and Reedlunn et al. [2021] have resulted in some new understandings of steady-state creep, particularly at low stress states. This work has resulted in an upgrade to the M-D model in Adagio that is called the M-D viscoplastic model.

The BH site has a shear zone (fault without fracture plane) that is important to the geomechanical behavior of the system. Modeling approaches to simulate the behavior of this shear zone, as well as the behavior of the horizontally oriented plane (interbed) between caprock and salt dome, have evolved through several approaches. This study describes how the new contact surface model was applied to the BH slippage planes.

The M-D viscoplastic contact surface (VCS) model, which uses the M-D viscoplastic constitute model for the salt and the mesh containing the interbed layer with contact surfaces between the salt and caprock layers, and fault blocks in overburden and caprock layers, is used in this study. In most caverns, the volumetric closures calculated from the VCS model match Caveman[1] (CM)'s better than the original M-D model's. This might be because the VCS model uses the steady-state creep at low stress states, and the sliding mechanism between the caprock and salt, and fault blocks.

However, the results for five caverns do not agree well. Therefore, the calibration of the parameter values is needed to match the simulation model to the field environment. The parameter values have been calibrated through several back-fitting analyses and determined. In all caverns except BH114, the volumetric closures calculated from the VCS model and CM agree well from 1991, when the caverns began operating, to the early 2000s. But after that, the difference starts to widen. CM's results show that the slope of volumetric closure tends to increase during 2000's compared to them during 1990's.

According to the record of raw water injection into each cavern, the injected amount was not very large by 2005, so there is little change in the volume of the caverns that were leached by the injected raw water. Therefore, it seems that the volumetric closure results up to the early 2000s in most caverns are in good match to CM's results. It may have contributed to the increase in the slope of the CM curve due to the volume of the caverns increased as the raw water injection amount was increased afterwards. However, the amount of injected water does not match the slope increase in normalized cavern closure in the same proportion.

One of the issues we are going to have that will make it difficult to compare Caveman and Adagio is that they do different things. Adagio uses either historic or user-specified pressures on the interior surface of the cavern and tests the salt reaction to that. Caveman tries to calculate the increased pressure on the fluid due to salt creep and fluid compressibility to calculate the change in volume in daily increments. Furthermore, whenever a fluid exchange is entered into Caveman, the overall volume of the cavern is changed by that amount; in the case of raw water, an additional 15% of the water volume is added to the cavern. This happens on a "daily" basis in the program. In Adagio, the cavern

[1] A software to implement a cavern pressure monitoring program which includes thermal, salt creep, and salt dissolution models and is able to predict the cavern pressurization rate based on the operational history of the cavern.

volume is increased only when a predesigned, meshed block of salt is removed from the calculation. It is not surprising that there is going to be greater discrepancy between Caveman and Adagio during times of frequent fluid movement and raw water injection.

In conclusion, Cavemen's calculation results could not be consistent with those from the BH geomechanical model. However, it could be used as a reference for examining the calculation results of the model. Since the simulation results up to the early 2000s agree well with Cavemen's results, the results calculated from this model could be used to examine the structural integrity of caverns in BH dome.

ACRONYMS AND TERMS

Acronym/Term	Definition
3D	Three-Dimensional
BH	Big Hill
CM	Caveman
D-P	Drucker-Prager
DOE	U.S. Department of Energy
EFF	Extended File Format
E-W	East-West
FE	Finite Element
HPC	Sandia High Performance Computer
M-D	Multi-Mechanism Deformation, Munson-Dawson
MDV	Multi-mechanism Deformation Viscoplastic
MIT	Mechanical Integrity Test
MMB	Million Barrels
MVS	Mining Visualization System
N-S	North-South
OBI	Oil-Brine Interface
ONI	Oil-Nitrogen Interface
PLC	Power Law Creep
Sandia	Sandia National Laboratories
SMF	Structure factor Multiplication Factor
SPR	Strategic Petroleum Reserve
VCS	M-D Viscoplastic Contact Surface
VSE	Viscoplastic Soft Element model
WHP	Wellhead Pressure
WIPP	Waste Isolation Pilot Plant

This page left blank

1. INTRODUCTION

1.1. Background

The U.S. Strategic Petroleum Reserve (SPR), operated by the U.S. Department of Energy (DOE), stores crude oil in solution-mined caverns in the salt dome formations of the Gulf Coast. There is a total of 60 storage caverns located at four different sites in Texas and Louisiana as shown in Figure 1. Sandia National Laboratories (hereafter 'Sandia') has served as a technical advisor on the SPR to DOE since 1980. As part of that responsibility, Sandia has long used computational geomechanical models to analyze the viscoplastic, or creep, behavior of the salt in which the oil storage caverns reside.

Salt creep causes storage caverns to deform inward, thus losing volume. This loss of volume affects the salt above and around the caverns, puts stresses and strains on borehole casings, and creates surface subsidence which affects surface infrastructure. Therefore, accurate evaluation of salt creep behavior drives decisions about cavern operations. When oil is withdrawn from a cavern in salt using freshwater, the cavern enlarges. As a result, the pillar separating caverns in the SPR fields is reduced over time due to usage of the reserve. The enlarged cavern diameters and smaller pillars reduce underground stability. It is necessary to establish a limit for the remaining pillar thickness between caverns without threatening the structural integrity of the caverns. The integrity of wellbores at the interbed between the caprock and salt is a serious concern in the Big Hill (BH) site. For the remediation and life extension of wellbores, more accurate predictions from the global model are needed.

Figure 1. Big Hill Strategic Petroleum Reserve site location map.

1.2. Objectives

This report presents the results of enhancements to the Munson-Dawson (M-D, and their impact on dome-scale model calculations. The M-D constitutive model was originally developed in the 1980's to

predict the thermomechanical behavior of rock salt. Benjamin Reedlunn [2018] enhanced the model (which he calls M-D viscoplastic). There are three significant enhancements to the M-D model. (1) New transient and steady-state rate terms were added to capture the creep behavior at low stresses (below about 8 MPa). Most laboratory creep measurements used to capture creep model parameters are conducted at deviatoric stresses of 10 MPa and higher. Tests at lower deviatoric stresses are usually not conducted because their small strain rates would cause the tests to be very slow taking months to complete. However, only a thin section around the caverns is typically in the >10 MPa stress range; the vast majority of the salt between the caverns experiences deviatoric stresses in the 1-10 MPa range. Recent efforts by Reedlunn [2016; 2018] and Reedlunn et al. [2021] connected with the WIPP project have determined that this missing characterization of salt creep may explain the difficulty both SPR and WIPP modelers have had matching observed in situ creep behavior with parameters obtained only from laboratory experiments. (2) The equivalent stress measure was changed from the Tresca to the Hosford yield surfaces[2] which allows for additional computational stability that can result in more accurate and faster converging calculations. (3) The M-D model's numerical implementation was overhauled, because it frequently failed to converge, causing long simulation times.

The BH site has a shear zone (fault without fracture plane) that is important to the geomechanical behavior of the system. Modeling approaches to simulate the behavior of this shear zone, as well as the behavior of the horizontally oriented plane (interbed) between caprock and salt dome, have evolved through several approaches. Adagio[3] had an original contact surface algorithm for modeling contact and sliding behavior between two solid surfaces, however the number of elements in the BH model exceeded the number of elements allowed in the algorithm. As an alternative, a thin, soft layer of elements was used for the interfaces between lithologies and assumed to behave mechanically like a contact surface. The soft element layer has a limitation, however, in that no matter how small of an elastic modulus value is used, the magnitude of the opening is constrained in response to subsidence across the top of salt. The author believes that this is an artificial constraint imposed by the model that would not be observed in the real system. In the meantime, the Sandia High Performance Computer (HPC) team continued to improve the contact surface algorithm and may now be applied to the BH model. The current study describes how the new contact surface model was applied to the BH slippage planes.

The causes of the damaged well casing segments at BH at the salt-caprock interface are a result of vertical and horizontal movements between the caprock and salt dome. The top of salt subsides because the volume of caverns below decreases with time due to salt creep closure, while the caprock subsides at a slower rate because the caprock is thick and stiffer. This discrepancy yields a deformation of the well. The deformed wellbore may fail at some time. It is expected that the wellbore deformation value in the interbed between caprock and salt can be calculated more realistically if a more realistic fault opening is realized.

The major fault (shear zone) is included in this model to perhaps better represent the large-scale deformation considered. To realize the fault which extends approximately North-South along the

---

[2] A yield surface is a five-dimensional surface in the six-dimensional space of stresses. The yield surface is usually convex and the state of stress of inside the yield surface is elastic. When the stress state lies on the surface the material is said to have reached its yield point and the material is said to have become plastic. There are many kinds of surfaces such as Tresca, Hosford, von Mises, Mohr-Coulomb, Drucker-Prager, and so on.

[3] Adagio is the most recently Sandia-developed 3D solid mechanics finite element code. It is written for parallel computing environments.

entire length of the caprock, the contact surfaces for the fault are inserted into the overburden layer and two caprock layers. The friction coefficients between two couples of contact surfaces (one is for the fault, the other is for the slippage between the caprock and salt dome) are assumed to be 0.2.

1.3. Advancement

This report is the upgraded version of Park [2019]. The following important advances are considered in this new computational simulation over the historical simulations:

1. This simulation uses the multi-mechanism deformation viscoplastic (MDV) model as a salt constitutive model. Plastic deformation of intact salt is isochoric and only occurs in the presence of shear stress. The original M-D model [Munson et al. 1989] considers three separate steady-state creep mechanisms and an overlying transient creep mechanism. Recent efforts by Reedlunn [2016, 2018] and others have resulted in some new understandings of steady-state creep, particularly at low stress states. This work has resulted in an upgrade to the M-D model in Adagio that is called the M-D Viscoplastic model.
2. This simulation considers the contact surfaces between the caprock and salt top, and for the fault from the surface to the salt top. It will realize the slide between the caprock and salt dome, and the fault blocks.
3. This simulation uses the updated daily wellhead pressure (WHP) and oil-brine interface (OBI) depth histories of SPR caverns that were recorded at the field office from 4/20/1990 through 2/1/2021. The real wellhead pressure plus the oil/brine pressure gradient was applied on the inside boundary of each SPR cavern as a function of depth.

1.4. Software

Create geometries and mesh generation:

Cubit 16.02 64 bit
Revised 2022-02-01
Copyright 2019 Sandia Corporation

Combine meshed blocks:

GJoin2 Version 1.38 (A GENESIS database combination program)
Revised 2021/10/27
Copyright 1988 NTESS

Solver:

Sierra Adagio Version 5.4.2 (A 3-D Nonlinear Solid Mechanics Finite Element (FE) Application for Quasistatic, Implicit Transient Dynamics, and Explicit Transient Dynamics). A 3-D Nonlinear Solid Mechanics Finite Element Application for Quasistatic, Implicit Transient Dynamics, and Explicit Transient Dynamics
Copyright NTESS

Post-processors:

Algebra Version 1.51 (An Algebraic Manipulation Program for Post-Processing of Finite Element Analyses Exodus II Version)

Revised 2022/03/23

Blot II-2 Version 3.141 (A Deformed Mesh / Contour Plot Program with X-Y Plotting Capabilities for Post-Processing of Finite Element Analyses)
Revised 2021/03/31

2. SITE DESCRIPTION

Figure 2 shows a plan view of the BH site with contour lines defining the approximate location of the salt dome top. The locations of fourteen SPR cavern currently in-use (101-114) and five potential expansion caverns (X1-X5) are indicated. The figure also specifies the undeveloped area north of the DOE property line (Sabine Pass Terminal). The diameters in N-S and E-W directions are measured as approximately 7000 ft and 5800 ft, respectively.

The West-East cross-section #1 through the northern-most row of caverns (Cavern 101-105) provides a geologic representation near the middle of the dome (Figure 3). The site has a thin overburden layer consisting of sandy soil; and an exceptionally thick caprock sequence comprised of two layers. The upper caprock is comprised mainly of gypsum and limestone, whereas the lower caprock is mostly anhydrite.

A major fault (shear zone) extends approximately North-South along the entire length of the caprock and for an unknown depth into the salt. This fault zone has a pronounced effect on the subsidence measured above the site and is a consideration for future cavern placement [Ehgartner and Bauer, 2004]. The salt dome is essentially two large salt spines. The two masses of salt are operating somewhat independently and while pushing up creating the shear zone separating the two spines and resulting in faulting in the caprock above. The shear zone is a region separating two salt spines, typically characterized by containing impurities, compositional changes, physical property variations, and possibly inclusions of hydrocarbons

Figure 4 shows a three-dimensional representation of the BH salt dome constructed by digitally piecing together the separate models of the flank and top of salt. Figure 5 shows the salt dome with caprock as viewed from North-East. For numerical analysis purposes, the top layer of overburden is modeled as having a thickness of 300 ft, the upper caprock 900 ft thick, and the lower caprock 420 ft thick. The interbed layer of 20 ft thick is assumed to exist between the lower caprock and salt dome. The bottom boundary of the present analysis model is set at 6000 ft below the ground surface, so the height of salt dome is 4360 ft.

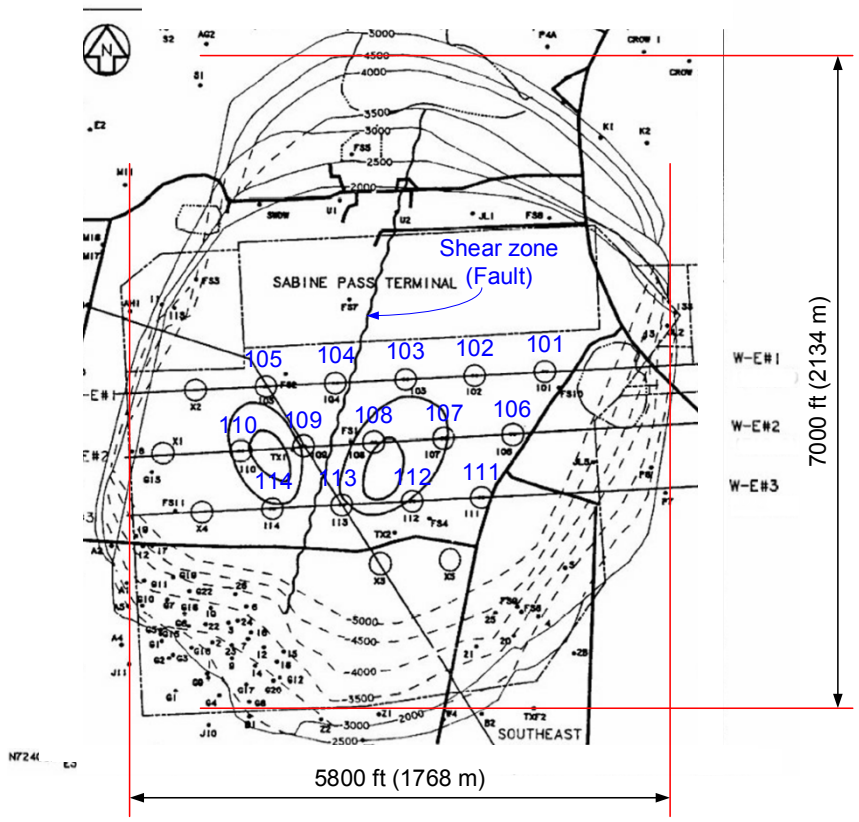

Figure 2. Big Hill site plan view [Magorian and Neal, 1988]

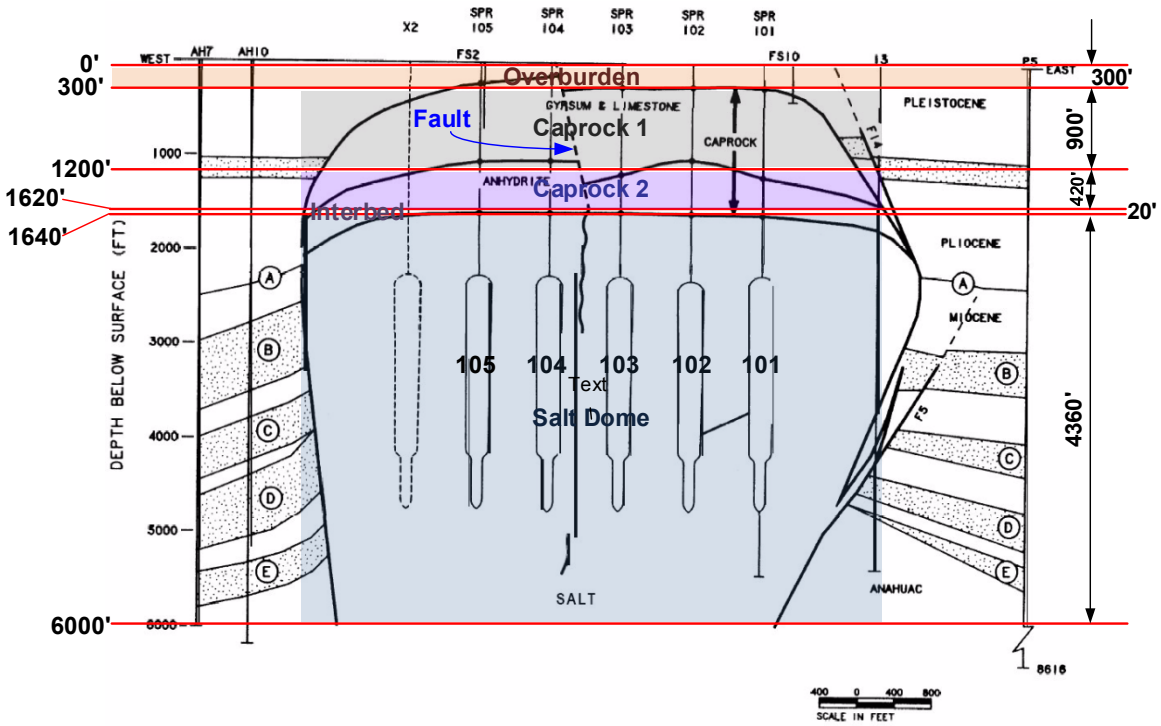

Figure 3. Cross-section (W-E #1 in Figure 2) near middle of dome [Magorian and Neal, 1988] looking north.

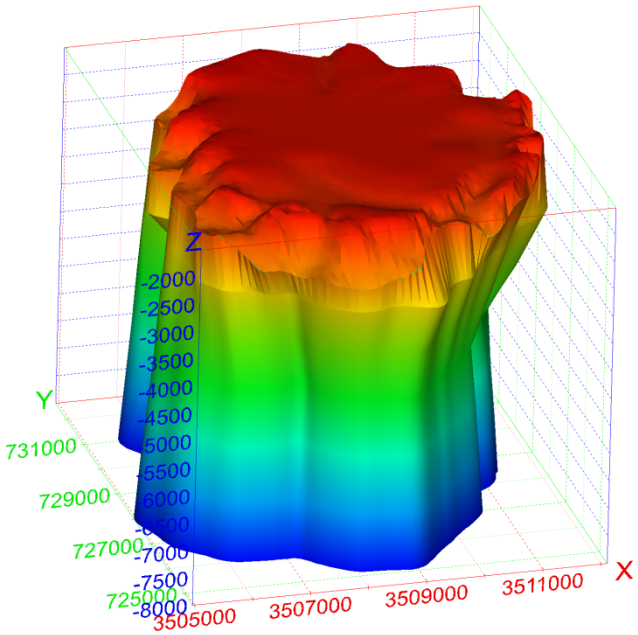

Figure 4. Three-dimensional representation of the Big Hill salt dome. The color depicts the elevation. No overburden or caprock is shown.

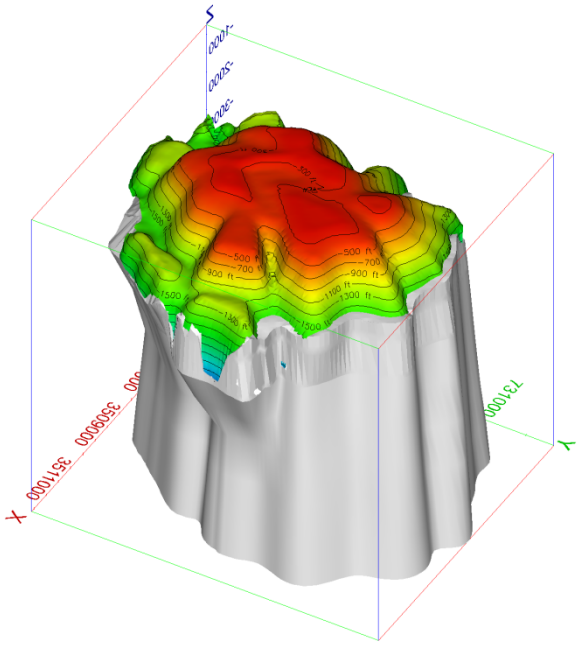

Figure 5. View of the caprock colored by elevation. The salt dome is shown in grey. View is from North-East at an inclination of 40º from the horizontal.

This page left blank

3. GEOMETRICAL CONDITIONS

3.1. Basic Rule

Finite element codes such as Sierra/Adagio are designed to conduct simulations with finite elements that are either tetrahedral or hexahedral. Three constitutive material models, i.e. the Power Law Creep (PLC) model, the Multi-Mechanism Deformation model and M-D Viscoplastic model, are available in Adagio to represent salt behavior. These three material models are programmed in Sierra/Adagio using eight-node hexahedral elements. Therefore, the mesh for the BH SPR site must be constructed with hexahedral elements. Hexahedral elements include six convex quadrilateral sides, or facets, with the eight corners where these facets intersect being the eight nodes for the element. The cavern boundaries such as the ceiling, wall, and floor are obtained from sonar measurements, and the irregular geometries of these boundaries ultimately require various shapes of facets. Similarly, the geometry of the flank of the salt dome, obtained from seismic measurements, also consists of complicated shapes of facets. To construct a mesh with convex hexahedral elements for a geological volume keeping the complicated geometry as much as possible, the following rules were established and followed:

1. Each perimeter (cavern and dome) consists of the same number of vertices at each depth interval
2. The reference distance between vertices on a perimeter is:
   a. about 20 ft for caverns
   b. about 80 ft for salt dome
3. The vertical thickness of an element level is kept constant at 20 ft
4. A 16% cavern volumetric increase is used for each drawdown leach

Modeling of the leaching process of the caverns is performed by deleting a pre-meshed layers of elements that make up the walls of the cavern so that the cavern volume is increased by 16 percent per drawdown. A 15% volume increase is typical for a standard freshwater drawdown, but the BH salt quality is different than that of other sites and has been observed to leach at a higher volumetric rate. So, a 16% volume increase is used for a drawdown. Also, typical leaching processes tend to increase a cavern radius more at the bottom of the cavern than at the top, with very little change to the roof and floor of the cavern. For the purposes of this modeling effort for Big Hill, leaching is assumed to add 16% to the volume of the cavern, and to occur uniformly along the entire height of the cavern, with no leaching in the floor or roof of the caverns. Each leaching layer, or onion skin, is built around the perimeter of the meshed cavern volume using the same rules stated previously. The detailed steps and methodologies to construct the FE mesh were provided by Park and Roberts [2015].

3.2. Finite Element Mesh

Figure 6 shows an overview of the hexahedral finite element mesh of the stratigraphy and cavern field at the BH SPR site. The dome, caverns, caprock, interbed, interface, and surrounding rock blocks are combined into the entire BH-model as Figure 22. The contact zone is modeled by a thin, soft element interbed layer block to evaluate the caverns' geomechanical effect on wellbore integrity. In the wellbore damaged interval, the casings of cement and steel are curved rather than cut. It can be assumed that the caprock bottom and salt top are not completely contacted together, but there is some space between them. Alternatively, it can be assumed that the strengths of the caprock and salt are much smaller than that of the wellbore steel casing. Since it is difficult to directly simulate these assumptions in the FE model, a soft element layer is inserted between the caprock and salt in this model. This is a different tool than putting a contact surface module to simulate sliding between them.

The mesh consists of 4,469,466 nodes and 4,423,500 elements with 362 element blocks, 10 node sets (on the boundaries of the entire mesh, to enforce zero normal displacement boundary conditions), and 90 side sets (on the interior surfaces of the caverns and cavern onion skin layers to enforce cavern pressure boundary conditions and contact surfaces between overburden blocks; caprock blocks; interbed blocks; interbed and salt dome blocks).

The blocks and surfaces IDs are defined as follows:

```
#=====================================================================
$ Blocks defined in the mesh
$ Salt dome    1 (Salt)
$ Overburden   20 and 22 in West and East, respectively; 2 in interface (Sand)
$ Caprock 1    30 and 32 in West and East, respectively (Limestone & Gypsum)
$ Caprock 2    40 and 42 in West and East, respectively (Anhydrite)
$ Farfield     5 (Surrounding Rock, Sandstone)
$ Interbed     80 and 82 in West and East, respectively (Sand)
$ Interface    9 (At Salt Dome)
$ Salt columns over/under the caverns:
$              1101 1102 1103 1104 1105
$              1106 1107 1108 1109 1110
$              1111 1112 1113 1114
$              initial 1st     2nd     3rd     4th     5th     6th(ext) 7th (extra 3 layers)
$ BH101 roof   110107  110117  110127  110137  110147  110157  110167   110177
$       body   11010   11011   11012   11013   11014   11015   11016    11017
$       floor  110109  110119  110129  110139  110149  110159  110169   110179
$ BH102 roof   11020   110217  110227  110237  110247  110257  110267   110277
$       body   11020   11021   11022   11023   11024   11025   11026    11027
$       floor  110209  110219  110229  110239  110249  110259  110269   110279
$ .
$ .
$ .
$ BH114 roof   111407  111417  111427  111437  111447  111457  111467   111477
$       body   11140   11141   11142   11143   11144   11145   11146    11147
$       floor  111409  111419  111429  111439  111449  111459  111469   111479
$---------------------------------------------------------------------
$ Side sets defined in Cubit
$ Fault
$ Overburden   Sset 20 for surfaces for Overburden in West
$ Overburden   Sset 22 for surfaces for Overburden in East
$ Caprock 1&2  Sset 30 for surfaces of Caprock 1&2 in West
$ Caprock 1&2  Sset 32 for surfaces of Caprock 1&2 in East
$ Interbed     Sset 30 for surface of interbed in West
$ interbed     Sset 32 for surface of interbed in East
$ Interface between Interbed and Salt
$ Interbed     SSet 80 for bottom surfaces of interbed 80 and 82
$ Salt dome    Sset 40 for top surface of salt dome
$---------------------------------------------------------------------
$ Node sets defined in Cubit
$ East and West sides of model       1
$ North and South sides of model     2
$ Bottom side of model               3
#=====================================================================
```

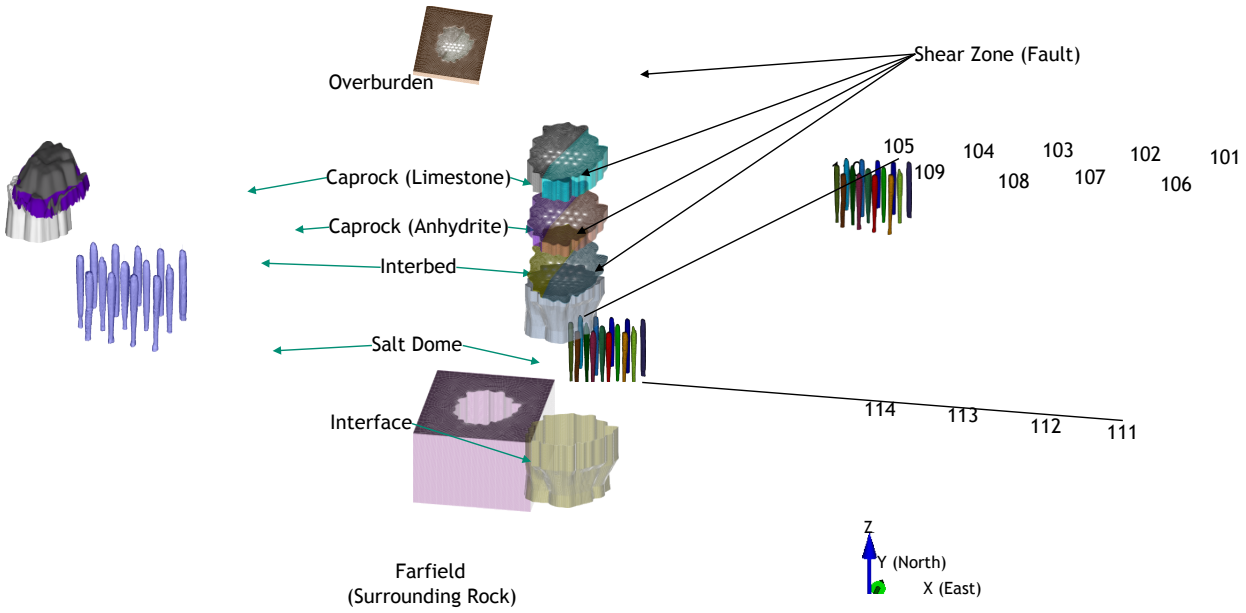

Figure 6. Images of Big Hill salt dome and caprock obtained from the seismic, sonar and borehole survey (left), an overview of the meshes of the stratigraphy (middle), and caverns (right). The cavern ID numbers are also shown. The US Patent (Number: 10657301, Grant date: 5/19/2020) is applied to create the mesh.

3.3. Salt Dome

The salt dome image is generated using the seismic data and 4DIM[4] tool. The three-dimensional hexahedral FE mesh is constructed using the seismic data and the CUBIT mesh generation tool as shown Figure 7. The 3D-coordinates of vertices are resampled from the seismic image. The real salt dome top is not flat as shown in the seismic image in Figure 7. The uneven top surface should create poorly shaped elements. To avoid a poor shape, the vertex data above the elevation of -2240 ft are removed (a process called 'trimming'). The vertex data for the upper salt blocks are translated vertically upward up to -1640 ft from the vertex data of the top of trimmed salt dome block (-2240 ft). The dome mesh consists of 218 element levels each 20 ft thick. The bottom elevation is -6000 ft.

[4] Four-Dimensional Interactive Model Player developed by C Tech.

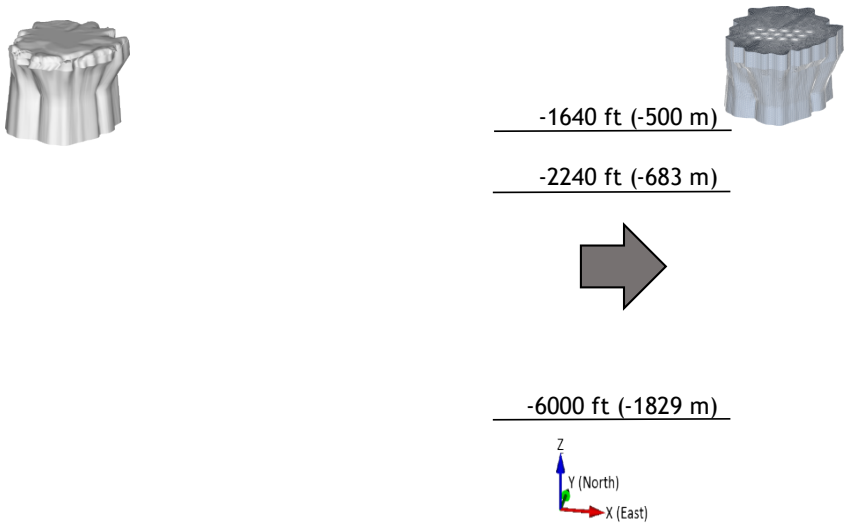

Figure 7. Images of Big Hill salt dome obtained from the seismic survey (left) and hexahedral finite element mesh using the seismic survey data.

3.4. Lithologies Surrounding the Salt Dome

3.4.1. Overburden

The top layer of overburden, which consists of sand and soil, has a thickness of 300 ft. The bottom of the overburden layer (top of the dome) is not flat as shown in Figure 3. The bottom is simplified as a flat to avoid creating poorly shaped elements. Figure 8 shows the meshed overburden block that is 12,400 ft width, 14,600 ft depth, and 300 ft thick. The thickness of each element layer is 20 ft in this model, so the mesh has 15 element levels vertically. This overburden block contains the shear zone (fault) trace which is represented by the contact surfaces.

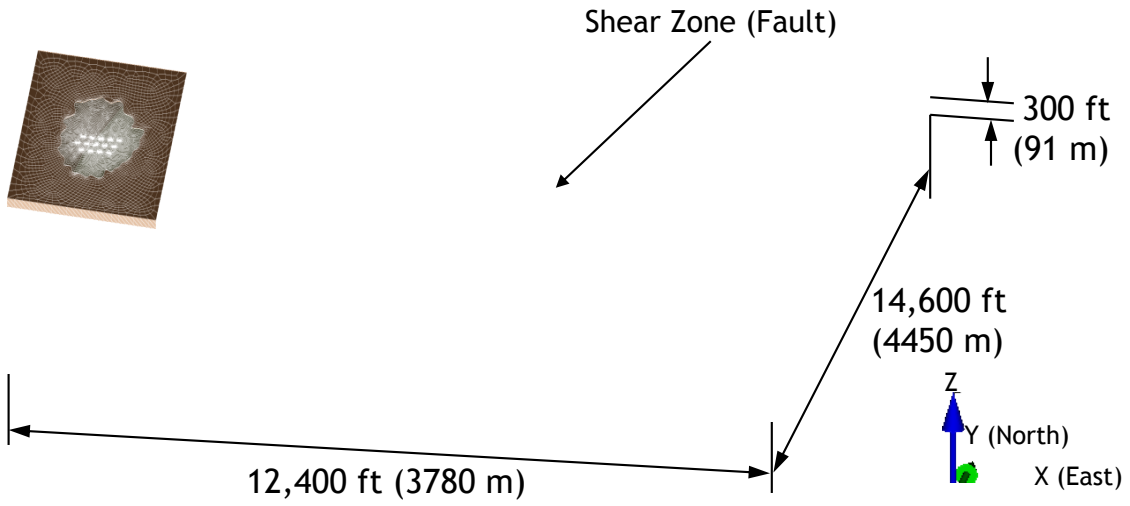

Figure 8. Meshed overburden block.

3.4.2. Caprock

Two layers of caprock exist over the BH salt dome. The upper caprock, consisting of gypsum and limestone, is 900 ft thick. The lower caprock, consisting of anhydrite, is 420 ft thick as shown Figure 3. Figure 9 shows the BH caprock image and hexahedral FE mesh. The image was generated using the seismic and borehole data with the 4DIM tool. Since the seismic is hard to differentiate between the caprock and salt, the caprock map relied heavily on borehole data, but would have been tweaked based on the mapping of the salt with seismic and borehole control. The bottom of the caprock surface is based on the topography of the salt dome top. The actual caprock top and bottom are not flat. The uneven top and bottom may produce poorly shaped elements. To avoid a poor shape, the vertex data for the caprock are translated vertically upward from the vertex data of the flat surface of salt dome top as shown in Figure 7. The thickness of each element layer is 20 ft in this model, so the meshes for the upper and lower caprocks have 45 and 21 element levels vertically, respectively, because the upper and lower caprock layers are simplified as flat slice blocks 900 ft and 420 ft thick for the numerical model as shown in Figure 9. This caprock blocks contains the fault trace which is represented by the contact surfaces.

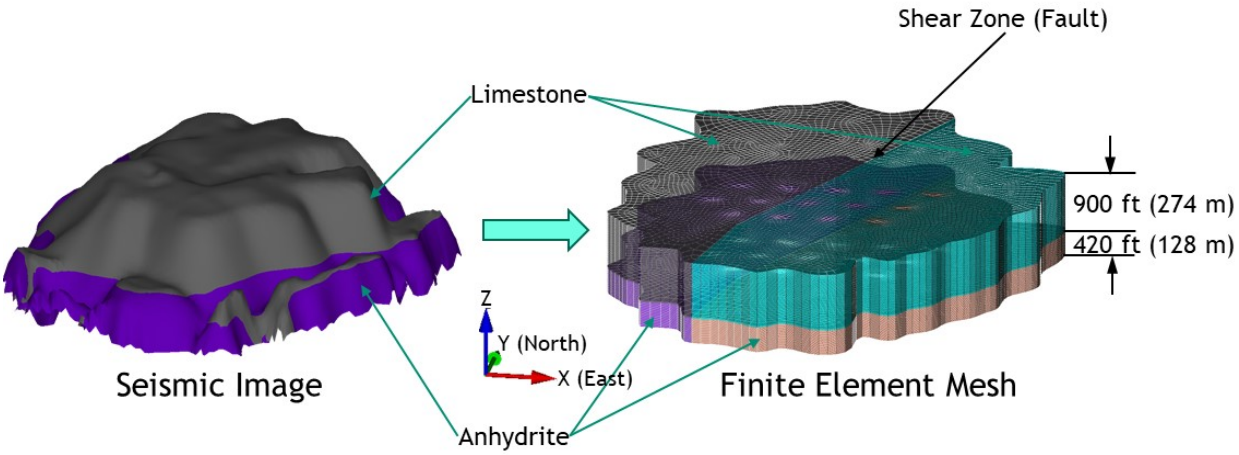

Figure 9. Image of Big Hill caprock obtained from the seismic and borehole survey (left) and hexahedral finite element mesh.

3.4.3. Interbed

The wellbore failures were found in wellbores of Caverns 105 and 109 at the BH SPR site in 2009 and 2010, respectively. Since then, a number of wellbore failures have occurred at the depth of the interbed between the caprock bottom and salt top [Sobolik, 2020]. A three-dimensional finite element model was constructed to investigate horizontal and vertical displacements in each well as it crosses the interbed [Park, 2014a]. The analysis results indicate that the casings of Caverns 105 and 109 failed, respectively, from shear stress that exceeded the casing shear strength due to the horizontal movement of the salt top relative to the caprock, and tensile stress due to the downward movement of the salt top from the caprock. The salt top subsides because the volumes of caverns in the salt dome decrease with time due to salt creep closure, while the caprock does not subside at the same rate as the salt top because the caprock is thick and stiff. This discrepancy causes deformation in the wells.

The contact zone is modeled by a thin, soft element interbed layer block to evaluate the caverns' geomechanical effect on wellbore integrity. In the wellbore damaged interval, the casings of cement and steel are curved rather than cut. It can be assumed that the caprock bottom and salt top are not completely contacted together, but there is some space between them. Alternatively, it can be assumed that the strengths of the caprock and salt are much smaller than that of the wellbore steel casing. Since it is difficult to directly simulate these assumptions in the FE model, a soft element layer is inserted between the caprock and salt in this model. This is a different tool than putting a contact surface module to simulate sliding between them.

Figure 10 shows the BH interbed FE mesh. The real interbed between the salt dome and caprock is not flat. The uneven interbed could cause poorly shaped element to be generated. To avoid a poor shape, the vertex data for the interbed are translated vertically upward from the vertex data of the simplified flat surface of salt dome top. The thickness of interbed layer is assumed to be 20 ft, so it has one element level. The interbed blocks contains the fault trace which is represented by the contact surfaces.

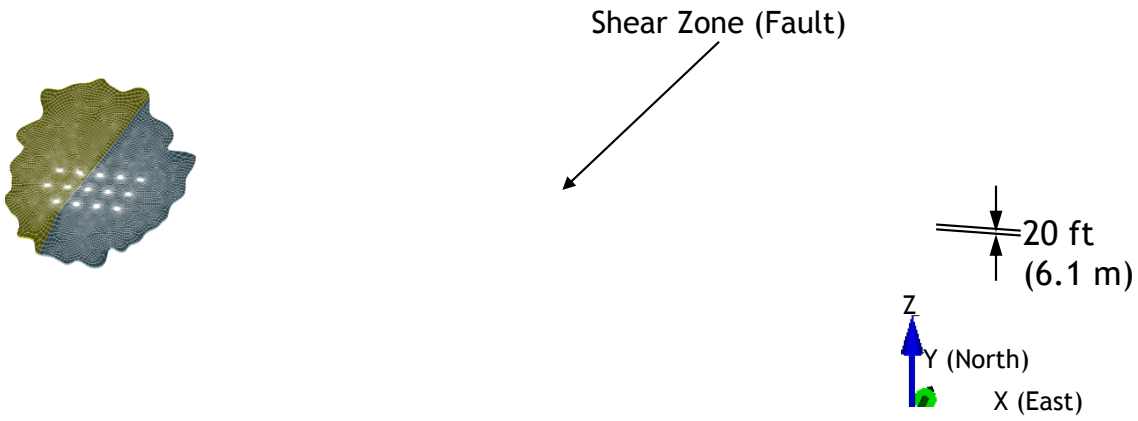

Figure 10. Finite element mesh of interbed between caprock and salt top.

3.4.4. Contact Surfaces

The major fault (shear zone) is included in this model to perhaps better represent the large-scale deformation considered. It is assumed that the fault extends from the surface to the salt top. The fault in the overburden, caprock and interbed layers is considered in this study since we do not know the depth of it in the salt dome. It is also assumed that the fault may be healed even if it extends into the salt. To realize the fault which extends approximately North-South along the entire diameter of the dome, the contact surfaces (surfaces 20 and 22; 30 and 32) for the fault as shown in Figure 11 is inserted into overburden layer (blocks 20 and 22), two caprock layers (blocks 30, 32, 40, and 42), and interbed layer (blocks 80 and 82). The friction coefficient between the contact surfaces is assumed to be 0.2. The surfaces of the eastern and western blocks consist of 6150 (1125+5025) sides (surface elements), respectively.

The contact surfaces (surfaces 40 and 80) are inserted between the interbed (block 80 and 82) and salt dome (block 1) as shown in Figure 12. It will realize the slide between the caprock and salt dome. The friction coefficient between the contact surfaces is assumed to be 0.2 as well. Each surface consists of 12,583 sides (surface elements).

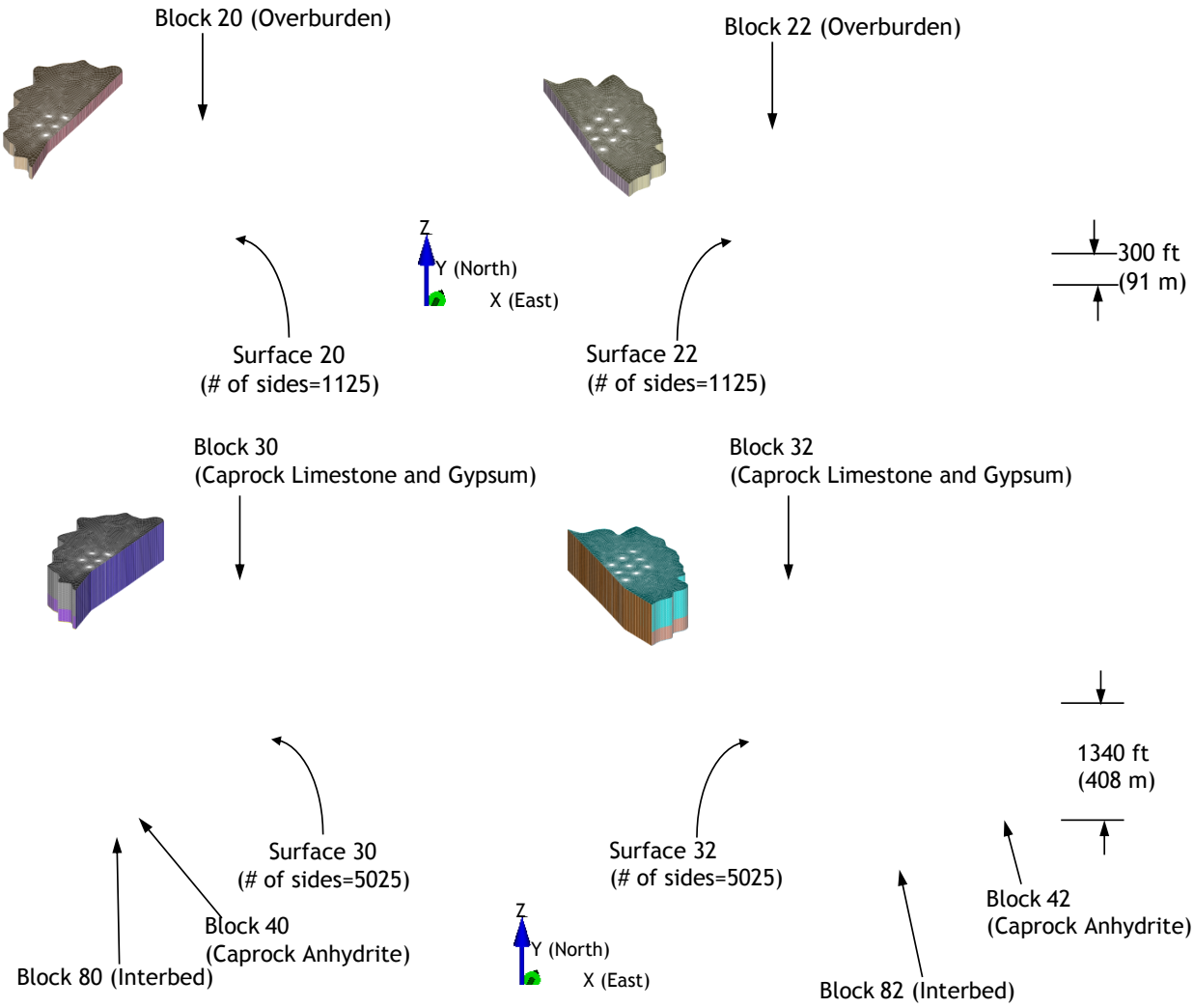

Figure 11. Contact surfaces to realize the shear zone (fault) in the overburden layer (top) and the caprock and interbed layers (bottom).

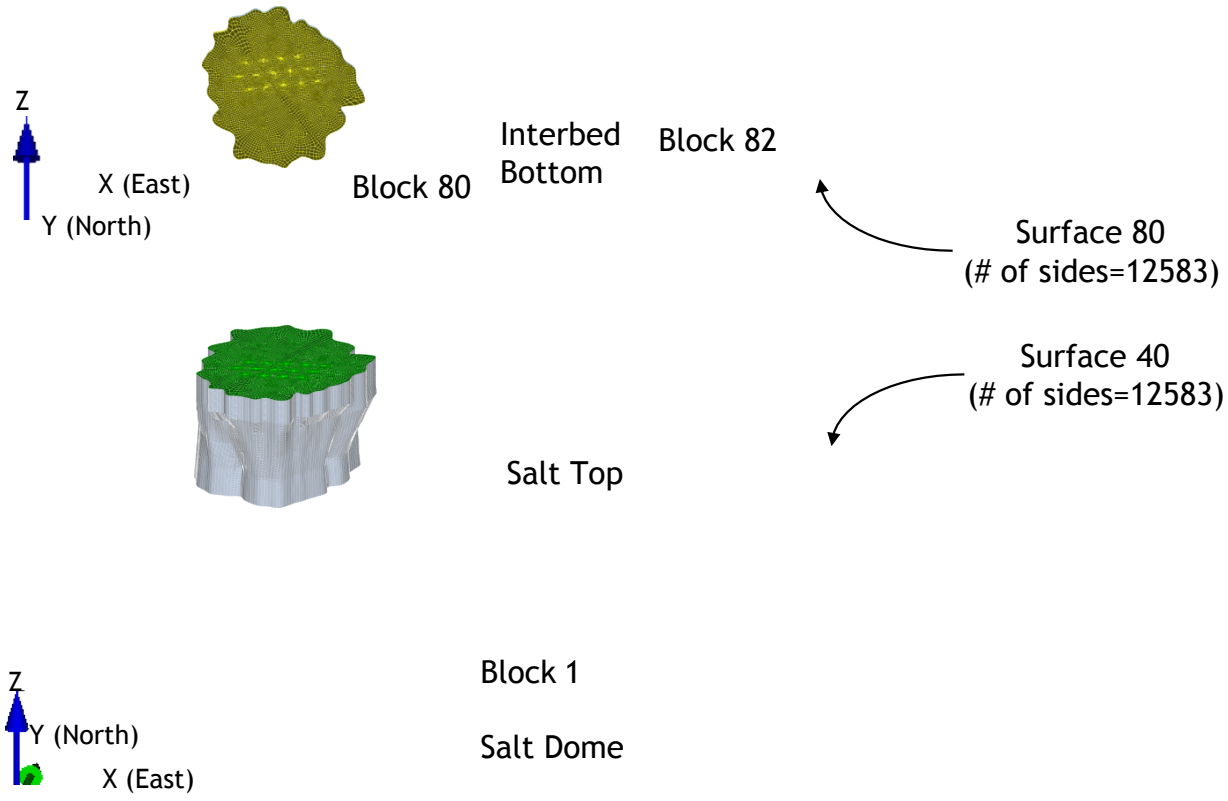

Figure 12. Interbed and contact surfaces to realize the slide between the caprock and salt dome.

3.4.5. Interface between dome and far-field (surrounding rock)

The salt dome is a piercement structure which has penetrated Mesozoic through Quaternary sediments. As in other types of intrusions, the salt dome must displace the overlying sediments as it pushes upward. Any sediment deposited above the dome must be either pushed aside and/or lifted, increasing the chance of erosion occurring on the loosened material. The mechanical failure of the sediments surrounding the dome has caused faults to develop both radially from and tangentially to the dome in a series of graben-horst structures [Hogan, 1980]. To consider the faults surrounding the dome, the interface block is inserted between the dome and sediments surrounding the dome which consists of the caprock, interbed, and salt dome blocks. As with the interbed block in Section 3.4.3, a thin, soft layer of elements is used for the interface between lithologies i.e., this model contains an interface block between the dome and surrounding sediments (hereafter 'surrounding' or 'far-field' rock) as shown Figure 13.

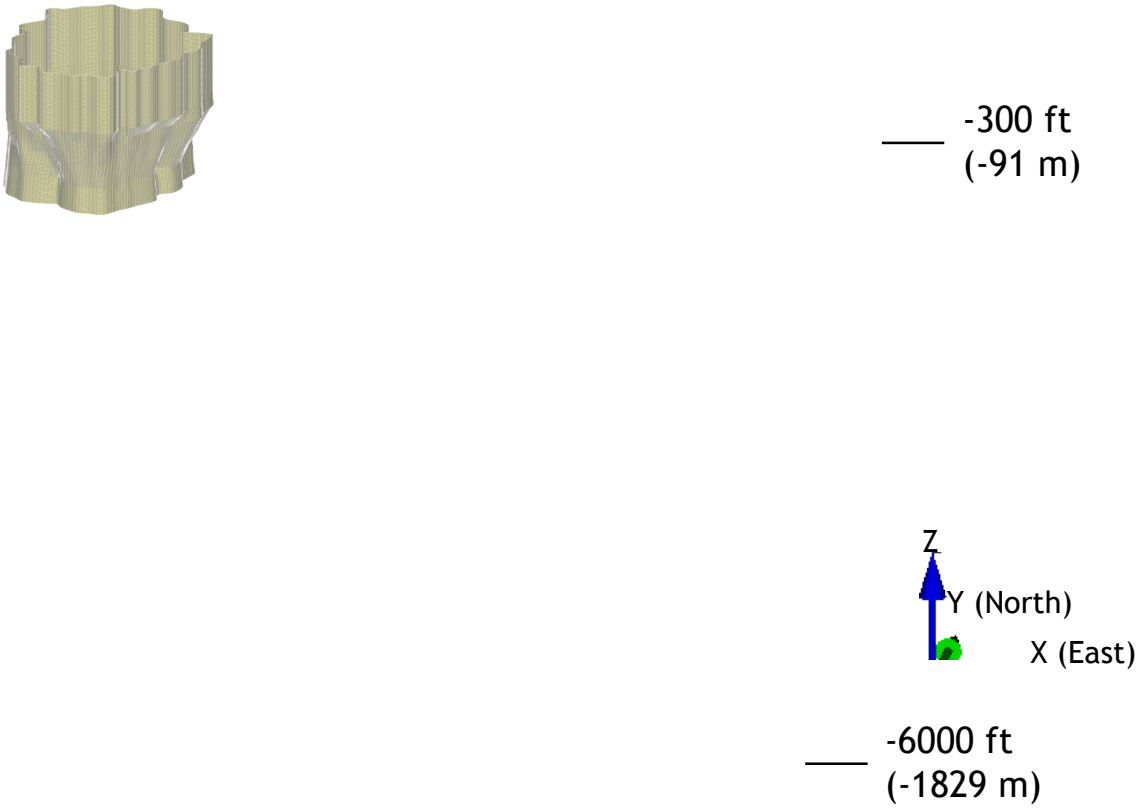

Figure 13. Finite element mesh of interface between dome and far-field.

3.4.6. Far-field rock

For simplification, the rock surrounding the salt dome is assumed to be made of an isotropic, homogeneous, linear elastic material in this model. The surrounding rock block encircles the interface, caprock, interbed, and salt dome blocks. The lengths of the confining boundaries are 14,600 ft in the N-S direction and 12,400 ft in the E-W direction as shown Figure 14. The sizes of the caverns are much smaller than the dome size. The model boundary distances (surrounding rock dimensions) can be regarded as being an infinite distance away from the caverns (i.e., fixed boundaries can be applied).

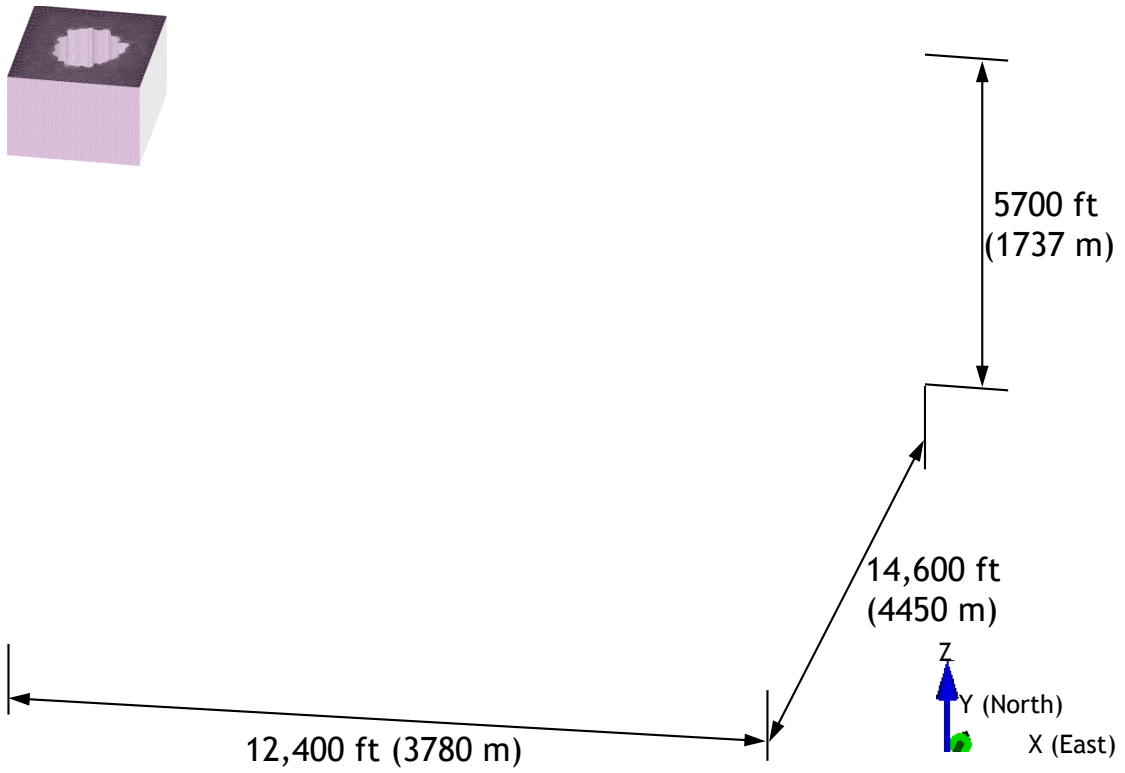

Figure 14. Finite element mesh of surrounding (far-field) rock.

3.5. Caverns

There are 14 SPR caverns in the Big Hill salt dome. Representations of the BH caverns based on sonar data were incorporated into the geomechanical model to provide a more realistic depiction of the caverns. To facilitate this, the cavern sonar data were resampled to a nodal spacing more appropriate for the geomechanical model. The actual sonar data is delivered from the sonar contactors. An additional processing code SONAR7[5] was used to turn these contractor files into a format compatible with the MVS[6] geologic modeling software suite. This is a mature process which has been used for many years at Sandia. This step is necessary to provide a full three-dimensional surface model of the sonar data. The assigned vertices in the FE mesh created in CUBIT need to be at specific depth intervals which may not correspond to the actual sonar sampling locations. Continuous three-dimensional surface models of the survey data are created, which allows sampling at any depth needed. This resampling step is performed through an algorithm coded using Python. Then, the resampled node coordinates data sets for the caverns are generated as the output in this step. The resampled nodal data are converted into CUBIT vertex data through another algorithm coded using Python. The

[5] A data conversion program developed by Sandia. SONAR7 converts sonar data sets with various formats provided by different vendors into the extended file format (EFF) and other MVS compatible formats.

[6] MVS (Mining Visualization System) is C Tech's flagship product for state-of-the art analysis and visualization. MVS was designed from the ground up to meet the demanding requirements of underground and surface mining analysis. Its tools are also used by civil engineers and advanced environmental modelers.

mesh is constructed using cavern slice blocks of 20-ft thick layers generated using the coordinates of vertices.

Table 1 lists the elevations of cavern top and bottom, cavern volumes in the mesh with the dates when the sonar data were obtained. The 3D hexahedral element meshes for 14 caverns constructed using various functions in CUBIT are shown in Figure 15.

Table 1. Elevations of cavern tops and bottoms, cavern volumes, and sonar survey dates.

Cavern ID	Sonar Survey Date	Top Elevation (ft)	Bottom Elevation (ft)	Volumes in the Mesh (MMB)	Volumes in the Mesh (ft^3)
BH-101	09/11/2012	-2240	-4120	14.14	79,398,740
BH-102	08/29/2013	-2280	-4020	12.40	69,604,013
BH-103	10/04/2011	-2260	-3820	12.41	69,664,667
BH-104	05/02/2012	-2260	-4160	13.28	74,541,296
BH-105	07/16/2013	-2260	-3960	12.92	72,528,615
BH-106	03/31/2015	-2280	-4060	12.53	70,348,964
BH-107	09/17/2019	-2240	-4040	11.91	66,886,820
BH-108	12/17/2019	-2320	-4060	10.77	60,482,152
BH-109	02/10/2020	-2260	-4140	12.28	68,955,817
BH-110	03/23/2020	-2260	-4140	12.09	67,880,161
BH-111	04/29/2015	-2240	-4200	13.16	73,909,534
BH-112	05/07/2015	-2280	-4180	12.55	70,483,655
BH-113	09/24/2015	-2260	-4120	11.72	65,808,317
BH-114	10/24/2013	-2320	-4100	12.41	69,687,984

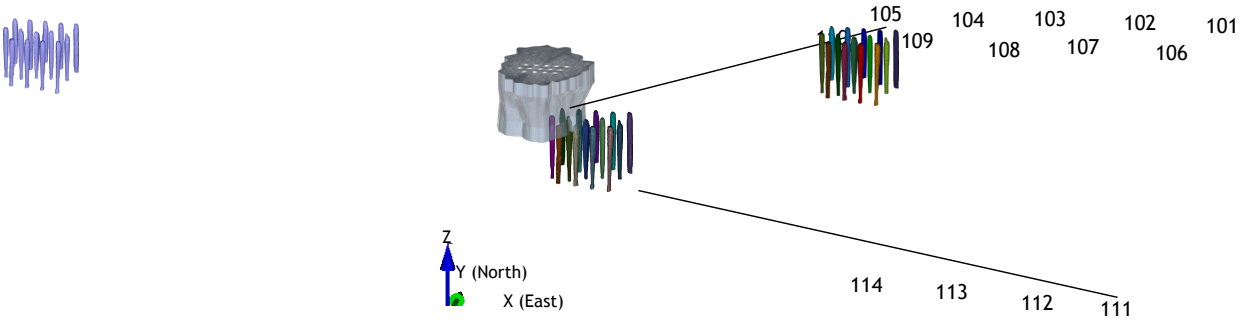

Figure 15. Sonar Images and hexahedral finite element meshed block of 14 caverns in the Big Hill salt dome. The cavern ID numbers are also shown.

As mentioned in Section 3.1, modeling of the leaching process of the caverns is performed by deleting a pre-meshed layer of elements along the walls of the cavern so that the cavern volume is increased by 16 percent per drawdown. Figure 16 shows the cavern cavities of BH101 and BH104 as developed from sonar data for instance, along with drawdown layers (leaching onion skins) and extra layers. In this simulation, each SPR cavern is modeled as having five drawdown layers to be removed to account for the future oil drawdown activities.

Figure 17 shows the geometry of BH-101 with the salt dome. The salt dome mesh has 14 cylinders for the caverns. The mesh is designed so that the cavity geometry of each cavern is placed in each cylinder. The perimeter of the cylinder encompassing each cavern consists of 36 elements, and this design is applied to all 14 caverns. When the geometry of a cavern changes due to oil sale, the cylinder

mesh is recreated by placing a cavity capturing the changed geometry in the cylinder and replace the newly created cylinder into the cylinder hole of the cavern in the salt dome mesh.

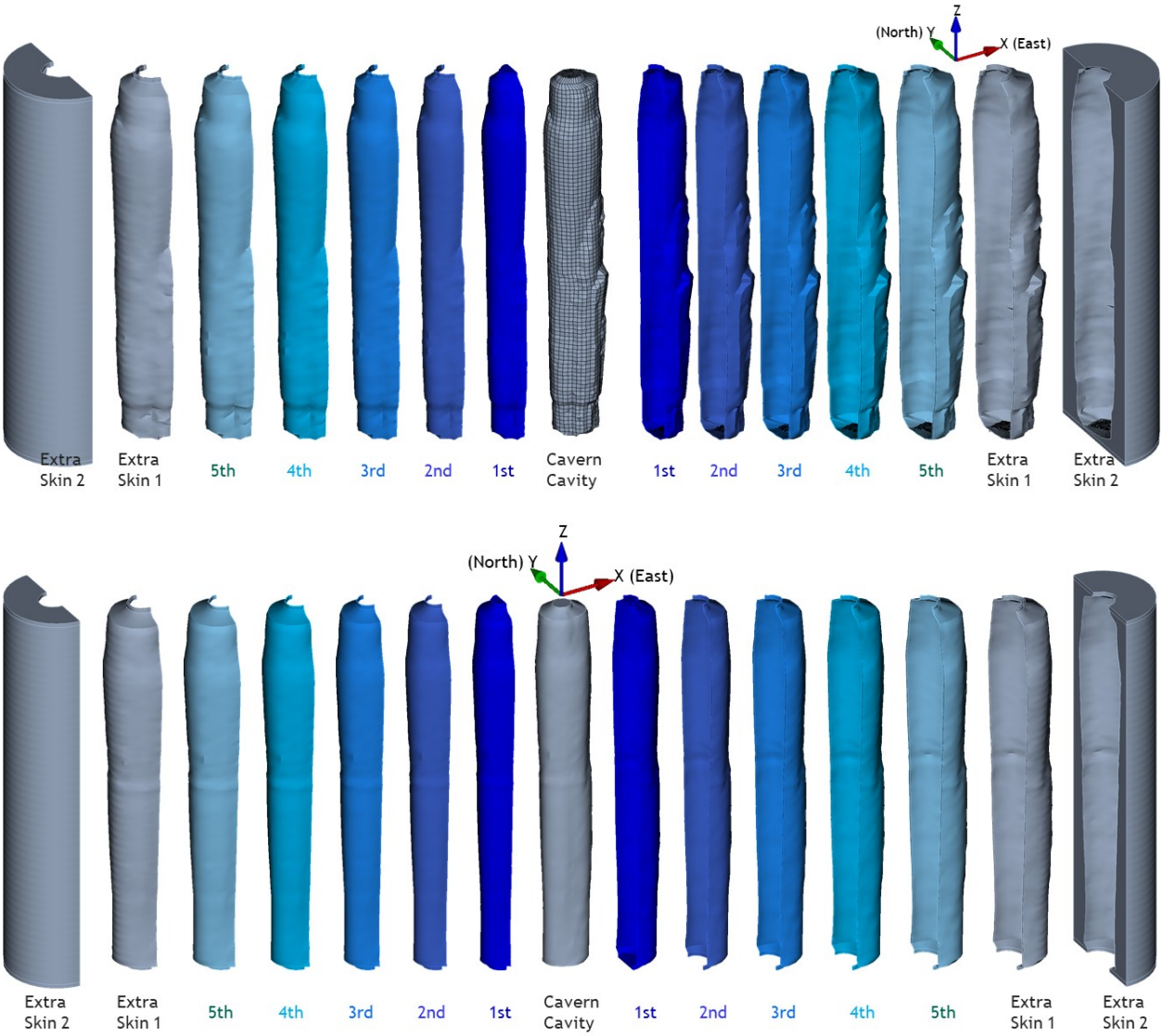

Figure 16. BH101 (top) and BH104 (bottom) cavern cavities with five drawdown onion skins (leaching layers) and two extra skins each.

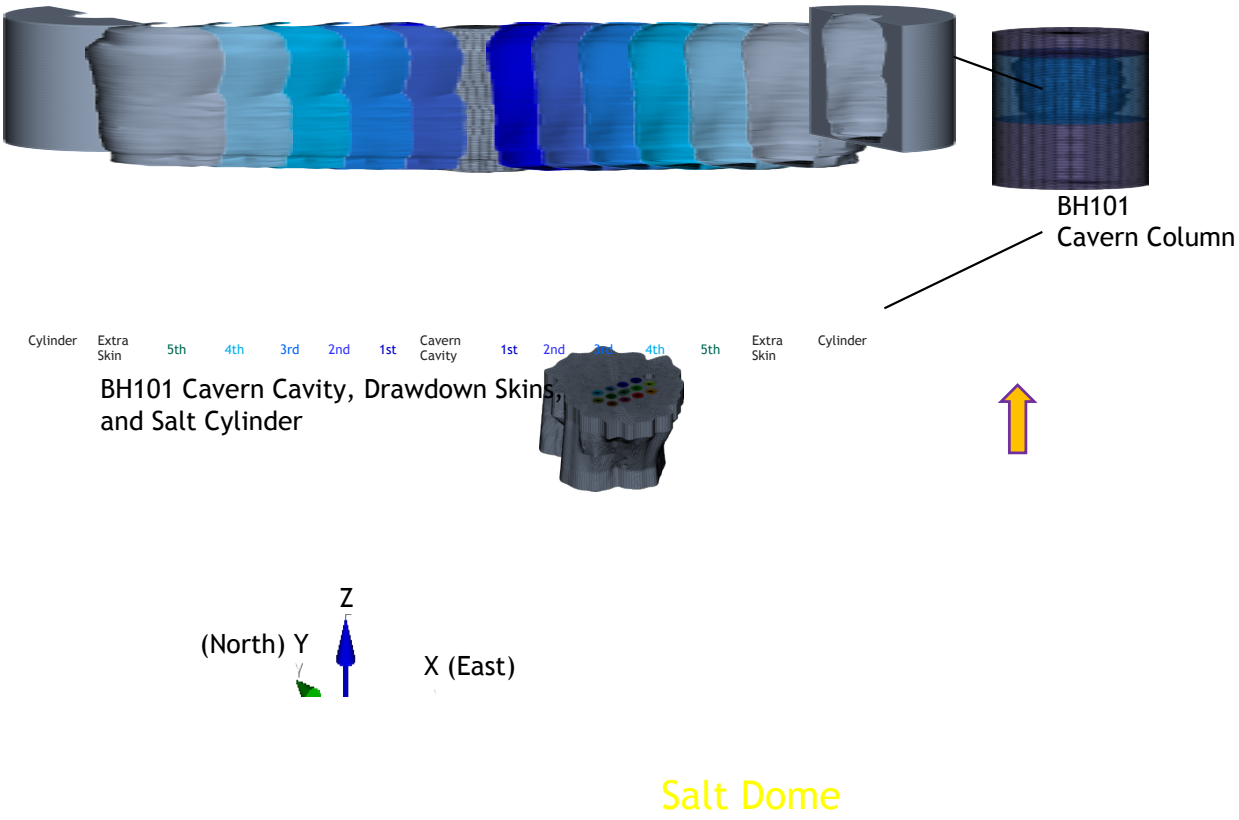

Figure 17. Geometry of BH-101. The salt dome has 14 cylinder-columns. The cavity of each cavern is placed in each cylinder. The perimeter of the cylinder surrounding each cavern consists of 36 elements, and this design is applied to all 14 caverns.

4. MECHANICAL CONDITIONS

4.1. Assumptions

In any numerical simulation of physical processes, it is frequently necessary to invoke a number of assumptions which render the analysis tractable. Analyses involving geologic materials are well known to be very challenging due to the extreme variability of rock quality (e.g., degree of fracturing) and the inability to fully characterize the in-situ response of the rock when subjected to events such as leaching and mining. While laboratory tests can be performed under controlled conditions to give insight into the stress-strain behavior, there are always questions about the degree of sample disturbance caused during the retrieval of the sample from the ground or even the relevance of the tests since the lab samples do not usually incorporate features such as discontinuities.

The finite element mesh developed for these analyses represents a region 12,400 ft by 14,600 ft in lateral dimensions and extending vertically from the ground surface down to the depth of 6000 ft. There are various assumptions for the computer simulations documented in this section:

- Use the simplified geometry of the planar layer for each interface between the lithologies,
- All materials are assumed to be isotropic and homogeneous,
- Use the material properties of anhydrite obtained from Waste Isolation Pilot Plant (WIPP) because the data of BH anhydrite are not known,
- Use the material properties of overburden for the interbed between the caprock and salt,
- Use the material properties of overburden for the fault from the surface to the salt top,
- A thin, soft layer of elements is used for the interface block between the dome and surrounding rock,
- The friction coefficient between the contact surfaces for the fault and interbed is assumed to be 0.2,
- Use a thickness of 20 ft for the interbed between the caprock and salt, and
- Every lithology is bonded to each other.

4.2. Wellhead Pressure

The modeling simulates the cavern responses forward in time from the cavern's initial creation. The real wellhead histories of 14 caverns have been recorded from the dates as listed in Table 2. For the purposes of the present simulation, it is assumed that the initial leaches of the caverns started on the dates one year before the wellhead pressure recording started i.e., they were leached to full size over a one-year period.

The peak wellhead pressures over 1000 psi in Figure 18 were created during mechanical integrity tests (MIT). To investigate well casing integrity for oil leakage, nitrogen gas is injected into the well. Nitrogen gas pressure at the wellhead causes pressure peaks because the nitrogen density is much less than oil density. The nitrogen gas pushes the oil-nitrogen interface (ONI) down towards the casing shoe, so the nitrogen replaces the oil between the wellhead and ONI. The density difference between oil and nitrogen can be offset by increased wellhead pressure, and then the resulting cavern pressure is only slightly different than normal oil wellhead pressure. The cavern volumetric closure rate due to salt creep depends on the difference between cavern internal and lithostatic pressures. The peak

pressures due to MIT do not affect the cavern internal pressure much, so the peak pressures can be ignored. The wellhead histories in Figure 18 were modified for use in the analysis as shown Figure 19. The real wellhead pressure plus oil/brine pressure gradient were applied on the inside boundary of each SPR cavern. Figure 20 shows the individual wellhead pressure histories used for 14 SPR caverns in this simulation.

Before initial leaching of a cavern starts, the model is given a stabilization period (1/1/1900 – 4/20/1989). To avoid the numerical shock, gravity is applied gradually into the mesh for ten seconds. After that, the model is allowed to consolidate with gravity for 89 years so that every element is stabilized numerically. The analysis simulates caverns that were leached to full size over a one-year period by means of gradually switching from salt to fresh water in the caverns. It is assumed that the SPR caverns were filled with petroleum and brine after the initial leaching. Creep is then permitted to occur over the entire simulation period (1/1/1900 – 2/1/2021).

Table 2. Dates of initial leach completion, wellhead pressure recording started, and assumed initial leach started

Cavern ID	Date of Initial Leach Completion	Date of Wellhead Pressure Recording Started	Assumed Date Initial Leach Started
BH101	09/17/1990	09/19/1990	09/19/1989
BH102	10/19/1990	10/20/1990	10/20/1989
BH103	11/27/1990	11/29/1990	11/29/1989
BH104	10/21/1990	10/21/1990	10/21/1989
BH105	05/13/1990	05/14/1990	05/14/1989
BH106	10/15/1990	10/17/1990	10/17/1989
BH107	04/23/1990	04/25/1990	04/25/1989
BH108	06/13/1990	06/14/1990	06/14/1989
BH109	07/23/1990	07/25/1990	07/25/1989
BH110	04/18/1990	04/20/1990	04/20/1989
BH111	07/14/1991	07/15/1991	07/15/1990
BH112	06/17/1991	06/19/1991	06/19/1990
BH113	04/30/1991	05/02/1991	05/02/1990
BH114	08/26/1991	08/29/1991	08/29/1990

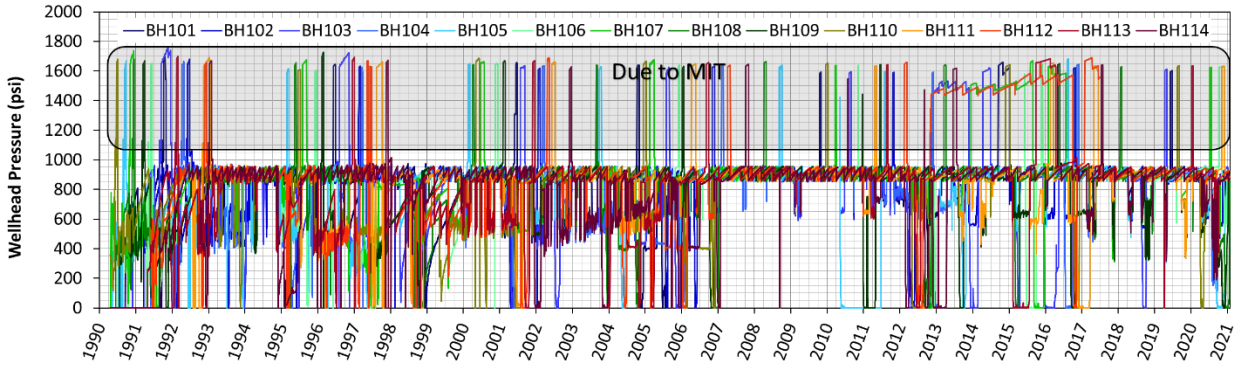

Figure 18. Wellhead pressure histories recorded from 14 Big Hill SPR caverns provided by the field office.

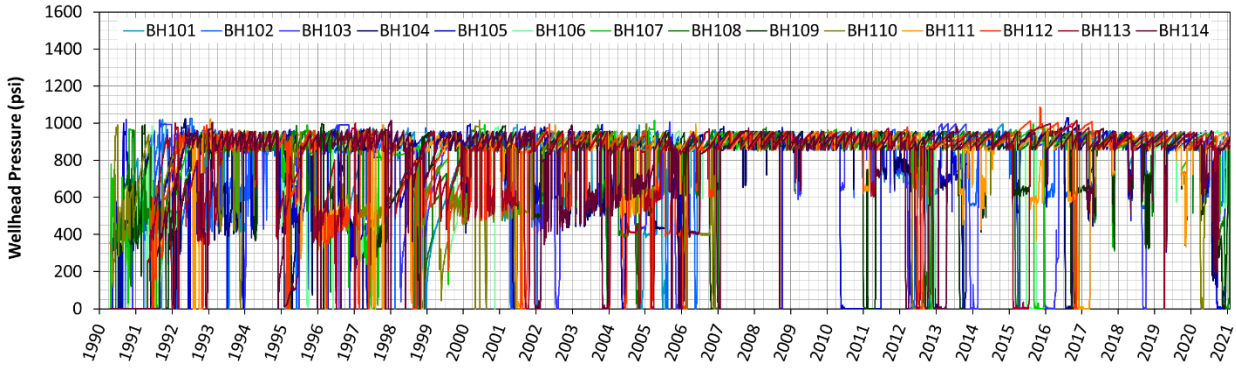

Figure 19 Modified wellhead pressure histories for the 14 Big Hill SPR caverns

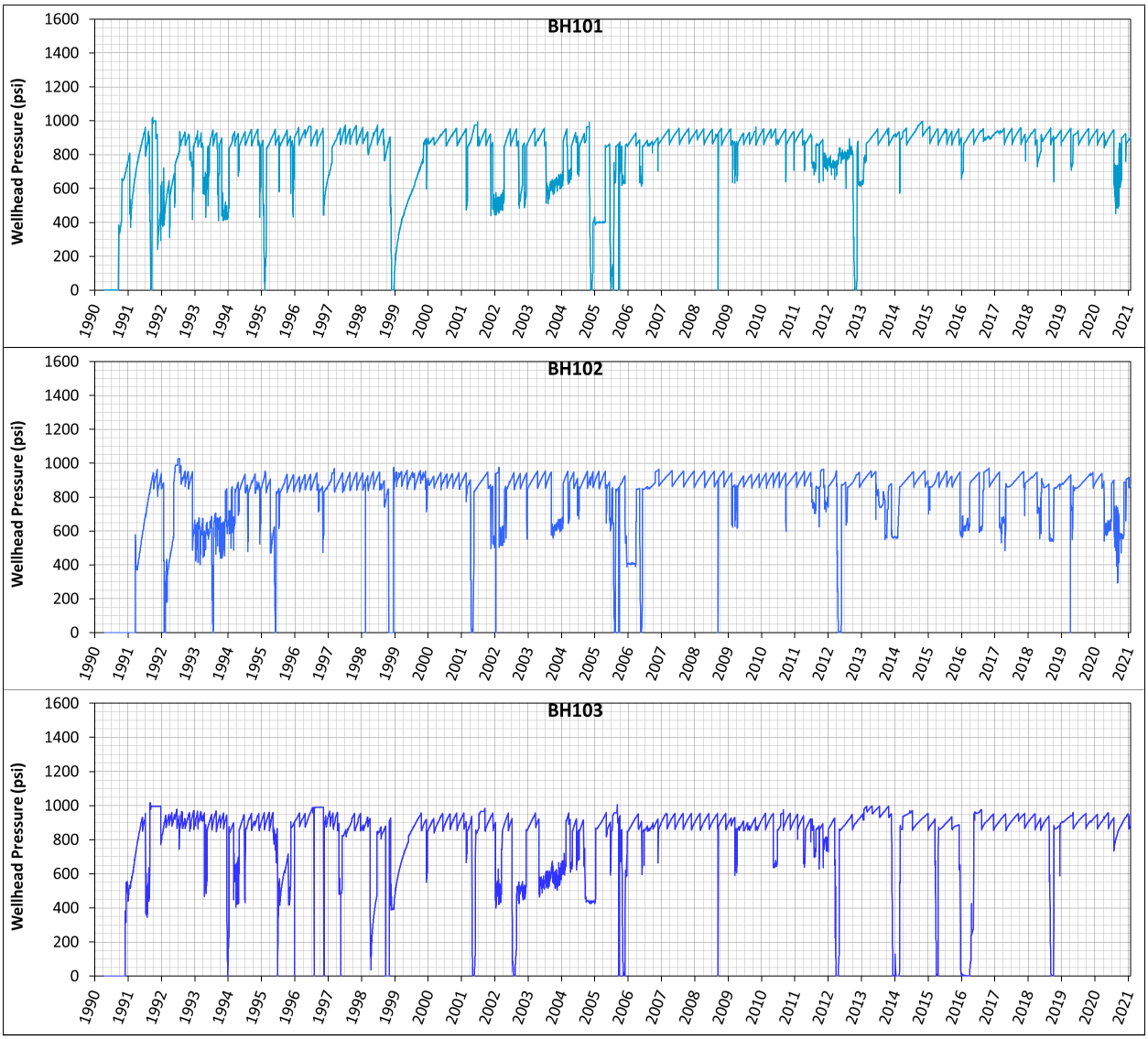

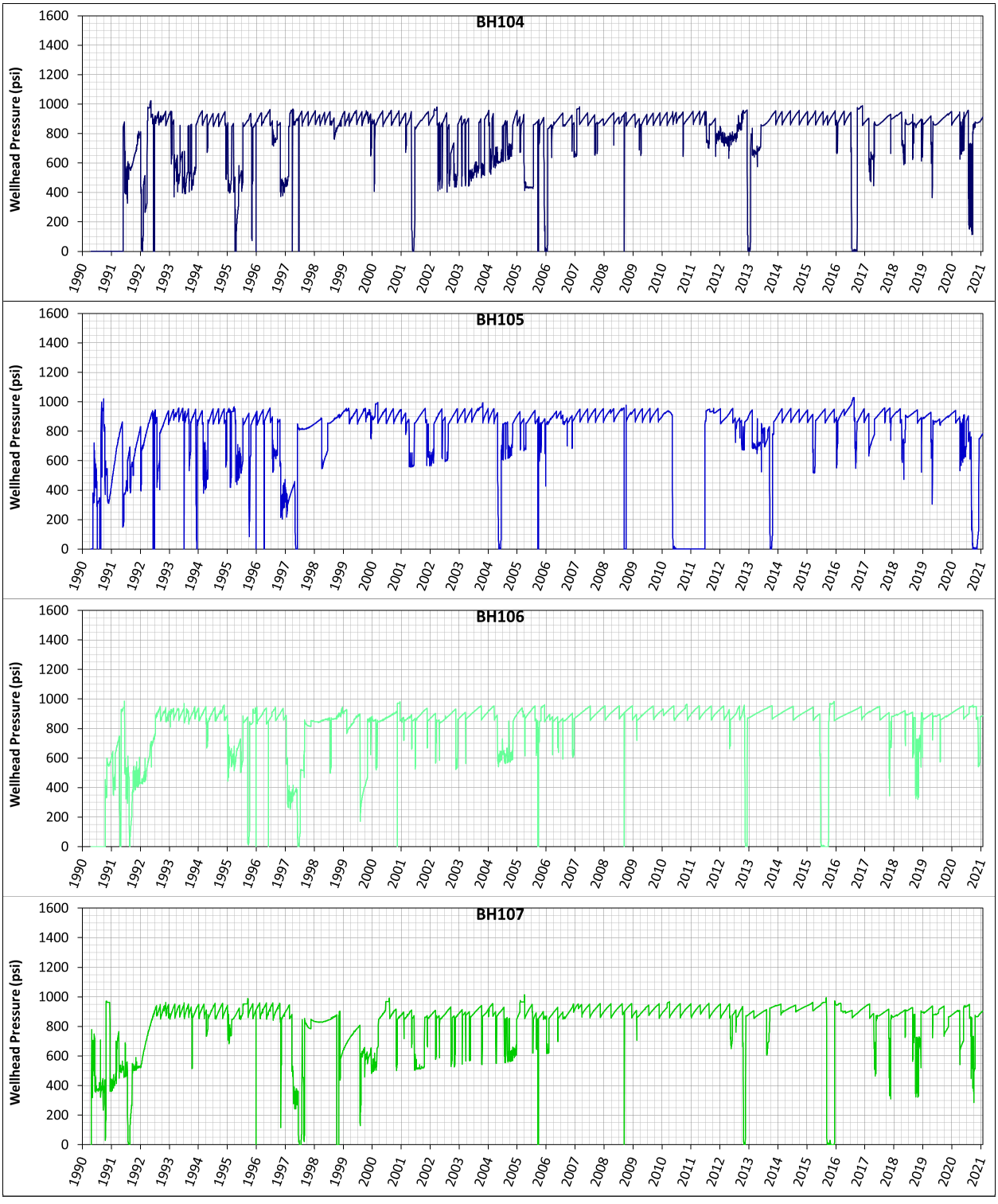
BH104
BH105
BH106
BH107
Wellhead Pressure (psi)
0
200
400
600
800
1000
1200
1400
1600
1990
1991
1992
1993
1994
1995
1996
1997
1998
1999
2000
2001
2002
2003
2004
2005
2006
2007
2008
2009
2010
2011
2012
2013
2014
2015
2016
2017
2018
2019
2020
2021

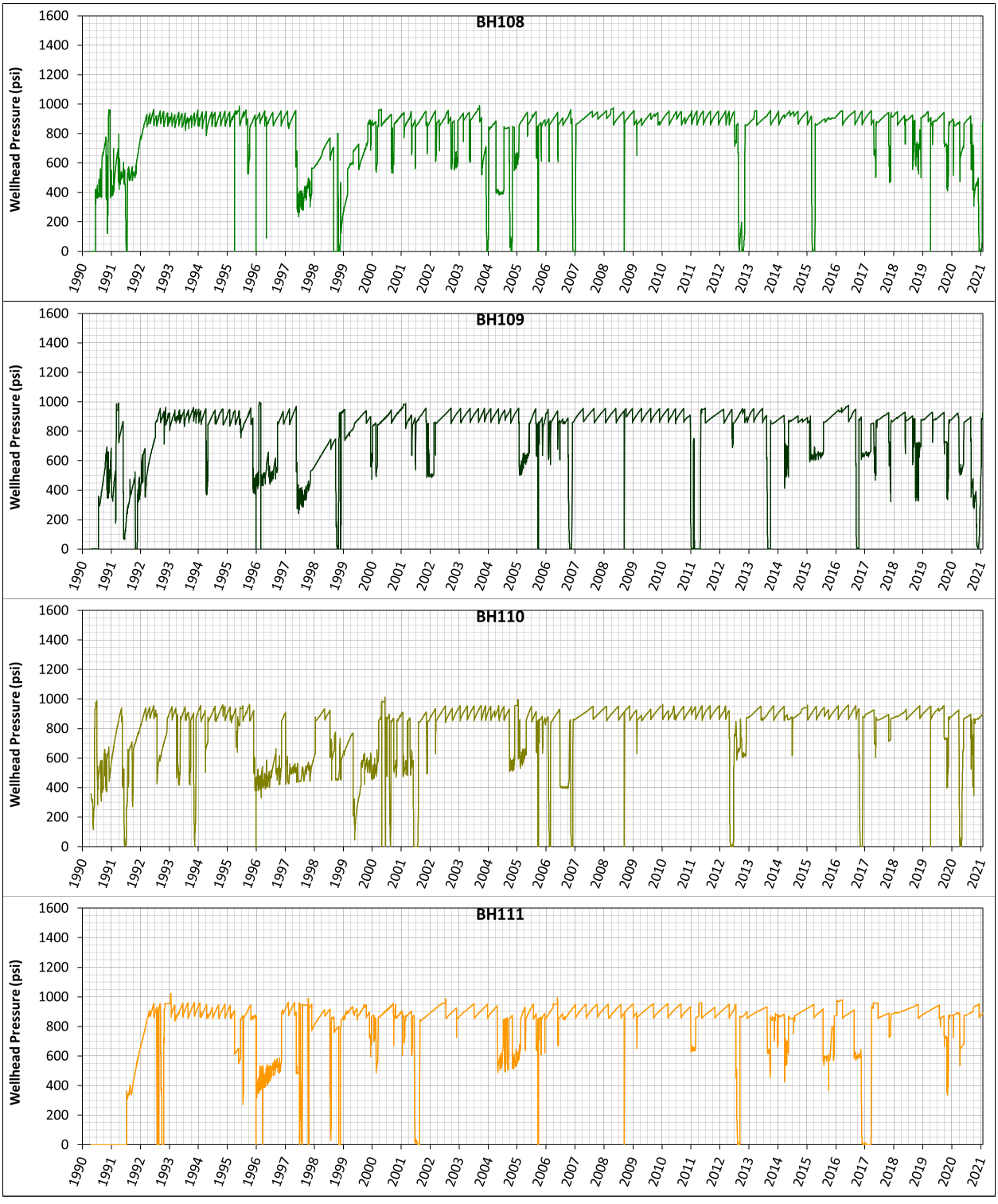
BH108
BH109
BH110
BH111
Wellhead Pressure (psi)
0
200
400
600
800
1000
1200
1400
1600
1990
1991
1992
1993
1994
1995
1996
1997
1998
1999
2000
2001
2002
2003
2004
2005
2006
2007
2008
2009
2010
2011
2012
2013
2014
2015
2016
2017
2018
2019
2020
2021

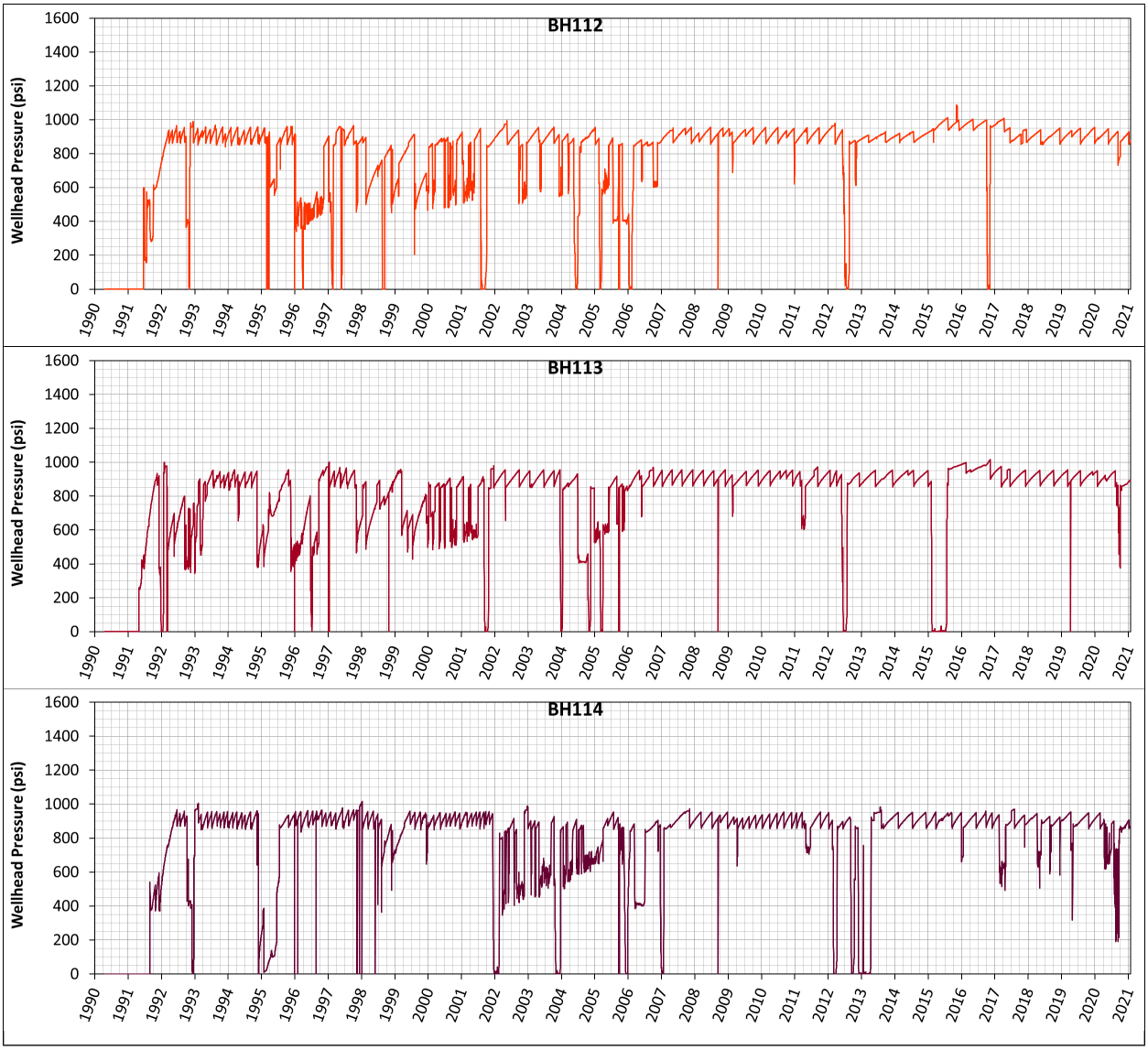

Figure 20. Individual wellhead pressure histories for the 14 SPR caverns used in this analysis.

4.3. Oil-Brine Interface

Previous analyses [Park et al. 2005; Park and Ehgartner, 2012; Park 2014 a and b; Park et al. 2014] assumed that the SPR caverns were filled fully with oil. However, the caverns were not always fully filled with oil. Brine fills the bottom of cavern and the portion changes with time depending on cavern operations. The difference between pressure gradients of oil (0.37 psi/ft of depth) and brine (0.52 psi/ft of depth) cannot be ignored. So, the amounts of oil and brine in a cavern over time needs to be considered. Park [2017] and Park et al. [2018] described the effect of the oil-brine interface (OBI) depth change. Figure 21 shows the OBI depth histories used in this analysis. The history data (4/20/1990 – 2/1/2021) were obtained from the field office.

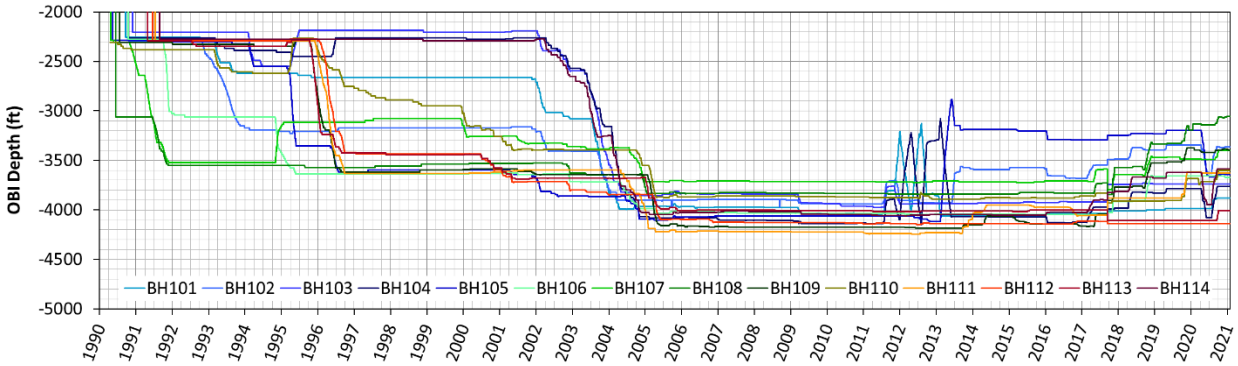

Figure 21. Individual oil-brine Interface depth histories to apply into the simulation for 14 Big Hill SPR caverns.

4.4. Temperature

The finite element model includes a depth-dependent temperature gradient which starts at 76.7°F (24.8°C) at the surface and increases at the rate of 1.41°F/100 ft (2.57°C/100 m). The temperature profile is based on the average temperature data recorded in well logs from BH prior to leaching [Ballard and Ehgartner, 2000]. The temperature distribution is important because the creep response of salt is temperature dependent. Radial temperature gradients due to cavern cooling effects from the cavern contents are not considered in these calculations. Previous 2D cavern studies have shown the predicted cavern deformation to be insensitive to the developed radial thermal gradients [Hoffman, 1992].

4.5. Boundary Condition

Figure 22 shows the assembled mesh and the boundary conditions. The lengths of the confining boundaries are 14,600 ft in the N-S direction and 12,400 ft in the E-W direction. The boundary dimensions are determined by more than two times of the dome's range in each direction. The salt dome is modeled as being subject to a regional far-field stresses acting from an infinite distance away. The sizes of the caverns are horizontally much smaller than the dome. Therefore, the North and South sides of far-field boundary are fixed in Y-direction, and the East and West sides are fixed in X-direction. The bottom is fixed vertically. The top surface and four sides are vertically free. The acceleration of gravity used in the model is 9.81 m/s^2 (32.174 ft/s^2).

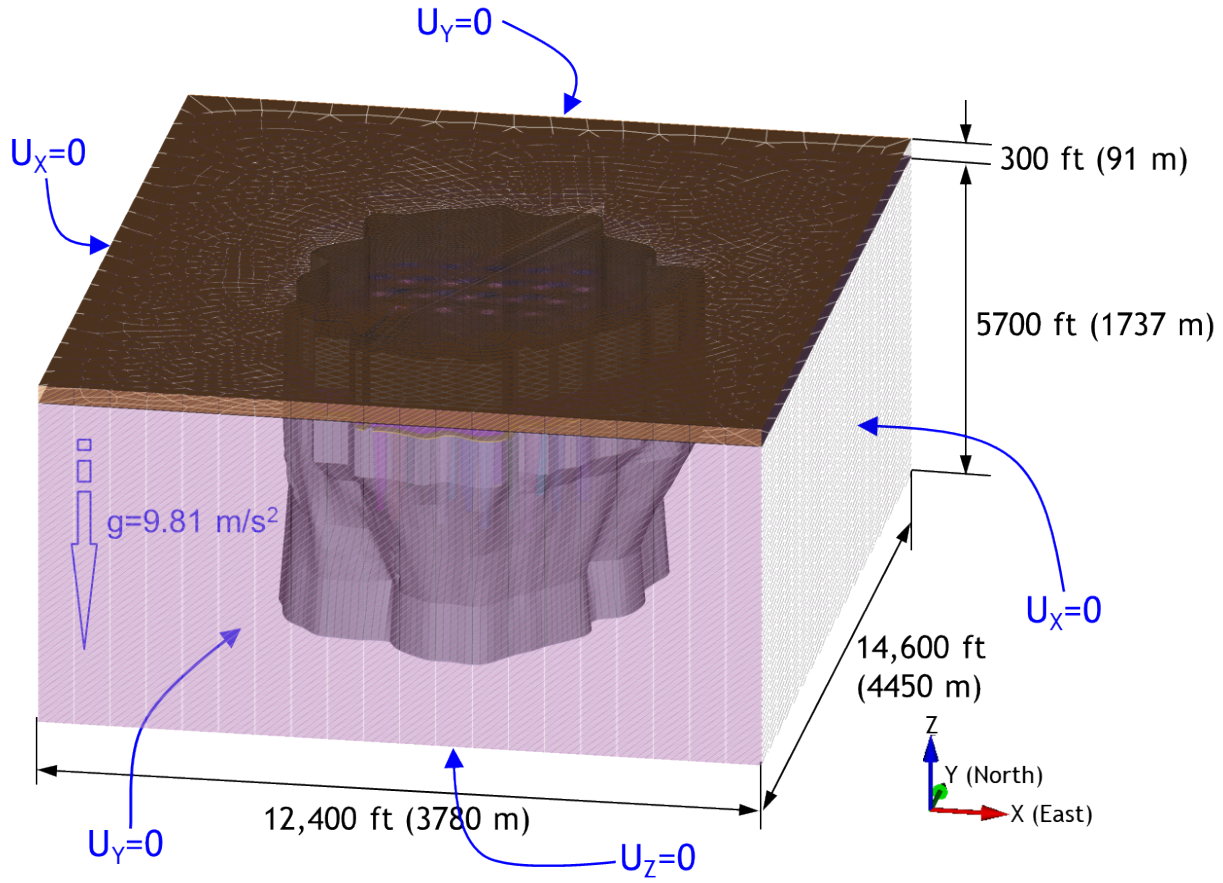

Figure 22. Boundary conditions of Big Hill Model.

5. MATERIAL PROPERTIES

5.1. Salt

5.1.1. M-D Viscoplastic Model

Plastic deformation of intact salt is isochoric and only occurs in the presence of shear stress. The original M-D model [Munson et al. 1989] considers three separate steady-state creep mechanisms and an overlying transient creep mechanism. Recent efforts by Reedlunn [2016, 2018] and others have resulted in some new understandings of steady-state creep, particularly at low stress states. This work has resulted in an upgrade to the M-D model in Adagio that is called the M-D Viscoplastic model. The following changes were made to the legacy M-D creep model formulation, and will be described in detail:

1. The equivalent stress (and flow potential) was generalized from Tresca to Hosford.
2. Steady-state mechanism 0 was added.
3. Transient strain limit mechanism 0 was added.

Originally, the M-D creep model utilized the von Mises stress as its equivalent shear stress measure (also known as deviatoric stress) $\bar{\sigma}$, but Munson et al. [1989] switched $\bar{\sigma}$ to the Tresca stress. Here, it is changed again to an equivalent stress measure proposed by Hosford [1972]:

$$\bar{\sigma} = \left\{ \frac{1}{2} \left[|\sigma_1 - \sigma_2|^a + |\sigma_2 - \sigma_3|^a + |\sigma_1 - \sigma_3|^a \right] \right\}^{1/a} \tag{1}$$

where σ_i are the principal stresses and a is a material parameter Eq. (1) encompasses the Tresca stress ($a = 1$), the von Mises stress ($a = 2$), and a range of behaviors in-between ($1 < a < 2$). One can also reproduce the Tresca stress with $a = \infty$, the von Mises stress with $a = 4$, and behaviors in-between with $4 < a < \infty$. This second range avoids a potential singularity in the second derivative of Eq.(1), so the exponent is restricted to $a \geq 4$.

The original M-D creep model decomposed the steady state behavior into three mechanisms. Several investigators (e.g. Bérest et al. [2005], Bérest et al. [2015], Salzer et al. [2015], and Düsterloh et al. [2015]), however, have reported larger steady-state creep rates at than would be expected from extrapolating rates from higher stresses. Thus, a fourth mechanism is added to capture the steady-state creep at low equivalent stresses. The mechanism is described by pressure dissolution, indicating that the porosity and fluid content of the salt are important components in the development of this mechanism. Among salt researchers, there has not yet been agreement on the mathematical form of the equation describing this new mechanism. For the MD viscoplastic model, Reedlunn used the same Norton-Hoff formulation for the low stress creep mechanism that is used in the original M-D model. The new expression for steady state creep is

$$\dot{\bar{\varepsilon}}^{\mathrm{ss}} = \sum_{i=0}^{3} \dot{\bar{\varepsilon}}_i^{\mathrm{ss}} \tag{2}$$

$$\dot{\bar{\varepsilon}}_i^{\mathrm{ss}} = A_i \exp\left(-\frac{Q_i}{RT} \right) \left(\frac{\bar{\sigma}}{\mu} \right)^{n_i} \quad \text{for } i = 0, 1, \text{and } 2 \tag{3}$$

$$\dot{\bar{\varepsilon}}_i^{\mathrm{ss}} = H(\bar{\sigma} - \bar{\sigma}_{\mathrm{g}}) \sum_{i=0}^{2} B_i \exp\left(-\frac{Q_i}{RT}\right) \mathrm{shin}\left(q \frac{(\bar{\sigma} - \bar{\sigma}_{\mathrm{g}})}{\mu}\right) \tag{4}$$

where the variable A_i, B_i, Q_i, n_i, $\bar{\sigma}_{\mathrm{g}}$, and q are all model parameters. All four mechanisms have an Arrhenius temperature dependence, where Q_i is an activation energy and $R = 8.314\ \mathrm{J/(K \cdot mol)}$ is the universal gas constant. An actual micro-mechanical mechanism for the creep behavior at low equivalent stresses has not been identified yet, so the new mechanism, Mechanism 0, is simply given the same mathematical form as Mechanisms 1 and 2. Mechanism 1 is meant to capture dislocation climb, which dominates at high temperatures and low equivalent stresses. Mechanism 2 dominates at low temperatures and medium equivalent stresses. The micro-mechanical cause for mechanism 2 is also unknown, but cross-slip has been recently suggested [Hansen 2014]. Regardless, the macroscopic behavior corresponding to the second mechanism has been well characterized. Mechanism 3 models dislocation glide, which is only activated when $\bar{\sigma}$ exceeds $\bar{\sigma}_{\mathrm{g}}$, as reflected in the Heaviside function $H(\bar{\sigma} - \bar{\sigma}_{\mathrm{g}})$. Typically, the parameters B_i are chosen to produce a smooth transition to mechanism 3 at $\bar{\sigma}_{\mathrm{g}}$.

The simple functional forms of Eqs. (3) and (4) suffice for the steady-state behavior, but the transient behavior is somewhat more complex. During work hardening under constant stress, $\bar{\sigma}^{\mathrm{tr}}$ approaches the transient equivalent strain limit $\bar{\sigma}^{\mathrm{tr}^*}$ from below, and the total viscoplastic strain rate slows down over time. During recovery under constant stress, $\bar{\sigma}^{\mathrm{tr}}$ approaches $\bar{\sigma}^{\mathrm{tr}^*}$ from above, and the total viscoplastic strain rate speeds up over time.

The rate that $\bar{\sigma}^{\mathrm{tr}}$ approaches $\bar{\sigma}^{\mathrm{tr}^*}$ is governed by

$$\dot{\bar{\varepsilon}}^{\mathrm{tr}} = (F - 1)\dot{\bar{\varepsilon}}_i^{\mathrm{ss}} \tag{5}$$

where

$$F = \exp\left[\mathrm{sign}(\bar{\varepsilon}^{\mathrm{tr}^*} - \bar{\varepsilon}^{\mathrm{tr}})\kappa\left(1 - \frac{\bar{\varepsilon}^{\mathrm{tr}}}{\bar{\varepsilon}^{\mathrm{tr}^*}}\right)^2\right] \tag{6}$$

The quantity κ depends on whether the material is work hardening or recovering:

$$\kappa = \begin{cases} \alpha_{\mathrm{h}} + \beta_{\mathrm{h}} \log_{10}\left(\dfrac{\bar{\sigma}}{\mu}\right) & \text{for } \bar{\varepsilon}^{\mathrm{tr}} \le \bar{\varepsilon}^{\mathrm{tr}^*} \\ \alpha_{\mathrm{r}} + \beta_{\mathrm{r}} \log_{10}\left(\dfrac{\bar{\sigma}}{\mu}\right) & \text{for } \bar{\varepsilon}^{\mathrm{tr}} < \bar{\varepsilon}^{\mathrm{tr}^*} \end{cases} \tag{7}$$

where α_j and β_j are model parameters. Note that the parameter κ must be non-negative, otherwise Eq. (5) produces a negative/positive $\dot{\bar{\varepsilon}}^{\mathrm{tr}}$ when $\bar{\varepsilon}^{\mathrm{tr}}$ is below/above $\bar{\varepsilon}^{\mathrm{tr}^*}$. Such behavior occurs during reverse creep, but the M-D creep model is only designed to model forward creep [Munson and Dawson 1982]. To enforce this, Eq. (7) is calculated first, and then

$$\kappa \leftarrow \max(\kappa, 0) \tag{8}$$

is applied.

The legacy M-D creep model used a single mechanism to endow $\bar{\varepsilon}^{\mathrm{tr}^*}$ with stress and temperature dependence. Reedlunn [2016], however, analyzed the data from Salzer et al. [2015] and Düsterloh et al. [2015] and discovered larger $\bar{\varepsilon}^{\mathrm{tr}^*}$ values for $\sigma < 8\ \mathrm{MPa}$ than would be expected from extrapolating

$\bar{\varepsilon}^{tr^*}$ values from higher stresses. Consequently, a second mechanism is added to capture the transient creep at low equivalent stress

$$\bar{\varepsilon}^{tr^*} = \sum_{i=0}^{1} \bar{\varepsilon}_i^{tr^*} \tag{9}$$

$$\bar{\varepsilon}^{tr^*} = K_i \exp(c_i T)\left(\frac{\bar{\sigma}}{\mu}\right)^{m_i} \tag{10}$$

where K_i, c_i, and m_i are parameters to be calibrated against experimental results. As before, the new transient strain limit mechanism, Mechanism 0, is given the same mathematical form as the original mechanism. This may be revisited if new information comes to light. Note that the notation of K_0 in the original M-D model is changed to K_1 because K_0 is used for Mechanism 0.

To summarize, the changes to the legacy M-D creep model formulation are:

1. The equivalent stress (and flow potential) was generalized from Tresca to Hosford in Eq. (1)
2. Steady-state mechanism 0 was added in Eq. (2)
3. Transient strain limit mechanism 0 was added in Eq. (9).

5.1.2. Parameter values of M-D viscoplastic for Calibration 3B, Big Hill and M-D creep

Fundamentally, salt creep behavior has common micromechanical constitutive features regardless of the origin of the salt, all that differs is the exact value of the parameters. In particular, those critical parameters that primarily distinguish one salt material from another salt material are the steady-state responses as represented by the structure factors (*A*'s and *B*'s) and the transient strain rate limits $\bar{\varepsilon}^{tr^*}$ as represented by K_i. By using the analysis criteria given above and the known behavior from the well-documented tests of clean WIPP salt as a baseline response, it may be possible on the one hand to construct reasonable steady-state responses for the domal salts. On the other hand, determination of the transient strain limit depends critically upon having the complete transient strain curves, i.e., complete conventional raw creep curves. In the absence of these curves, only uncertain estimates can be made for values for this parameter. Often, the only recourse in this case is to estimate the transient strain limit values based on the particle impurity level and the measured values from the clean and argillaceous WIPP salts. Remaining parameters are either unaffected by or insensitive to the specific salt material [Munson, 1998].

The database for Big Hill salt is developed using stress and temperature change tests from three specimens [Wawersik, 1985]. The specimens were prepared from recovered core from two deep boreholes at the site. These boreholes were to become solutioning wells, specifically Well 106B and Well 108B. Grain sizes were from medium to quite large, ranging from 3.7 mm (0.12 inch) to 51 mm (2.0 inch) with some cores having grains in excess of 100 mm (4.0 inch) in diameter. Although the salt purity was probably high, visual examination suggested finely distributed anhydrite crystals in the specimens from Well 106B. Magorian and Neal [1988] described the geology of the site in detail and reported insoluble contents based on density logs and x-ray analysis. The calculated median of insoluble from all logged holes is 1.7%, probably anhydrite. Anhydrite content was greatest in Wells 110A and 110B. Core samples indicated the occurrence of anhydrite bands parallel to the dome edges. It was believed that insoluble quantities decrease toward the edges of the dome [Munson, 1998]. Figure 23 shows the steady state creep rates for Big Hill domal salt.

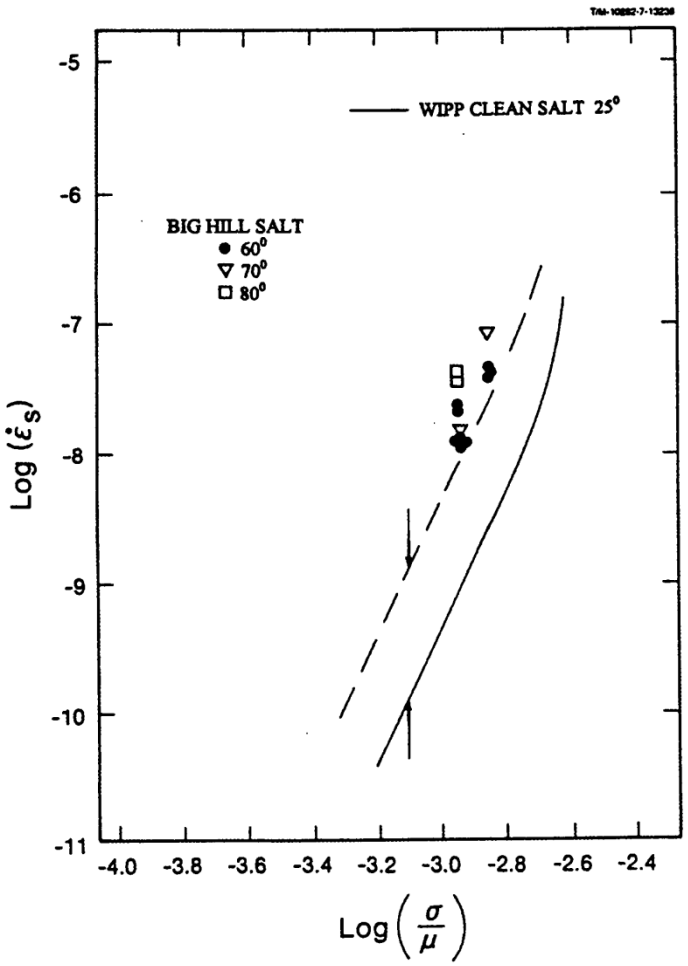

Figure 23. Steady state creep rates for Big Hill domal salt [Data from Wawersik, 1985]

Indirect substantiation of the effect of differences in the creep response of domal salt is found in the work of Ehgartner et al. [1995] on loss of volume of petroleum storage caverns of the SPR. These results are produced from a Caveman simulation methodology based on the M-D creep equations. The methodology generates a set of "effective" fitting parameters for material, geometry, pressurization, and stress in the cavern setting as determined from cavern fluid loss histories and can be used to predict "effective" SPR cavern creep rates. These rates have been reported [Linn, 1997] from an ullage study. The effective creep rates in volume loss percentage per year (the same as a linear rate) are shown in Figure 24. Of the four facilities studied, Big Hill and West Hackberry show the highest creep volume loss rates; whereas, Bryan Mound and Bayou Choctaw show the lowest [Munson, 1998].

Because all of the creep tests were conducted at relatively low stress and low temperature, we can characterize the creep in terms of the structure factor of just one of the three mechanisms involved in salt creep. This is the undefined or empirical mechanism with the structure factor A_2. Values of the structure factor can be used to evaluate the relative creep "resistance" of the various domal salts compared to the WIPP clean salt creep baseline. Structure factor multiplication factor (*SMF*) from WIPP 25°C pure salt baseline is defined as $SMF = A_{2\ \text{Domal Salt}} / A_{2\ \text{WIPP Salt}}$. A_1, B_1, and B_2 of domal salt are multiplied those of WIPP salt by *SMF*. By applying ratios determined from the creep results, we can establish some suggested M-D creep parameters. However, the limited database permits only

structure factors to be determined; all other parameters are established on the basis of the clean WIPP salt database and the logical extension of the WIPP parameters, considering how material variation can affect the parameter. These results are given in Table 3 for clean WIPP salt and the Big Hill salt [Munson, 1998].

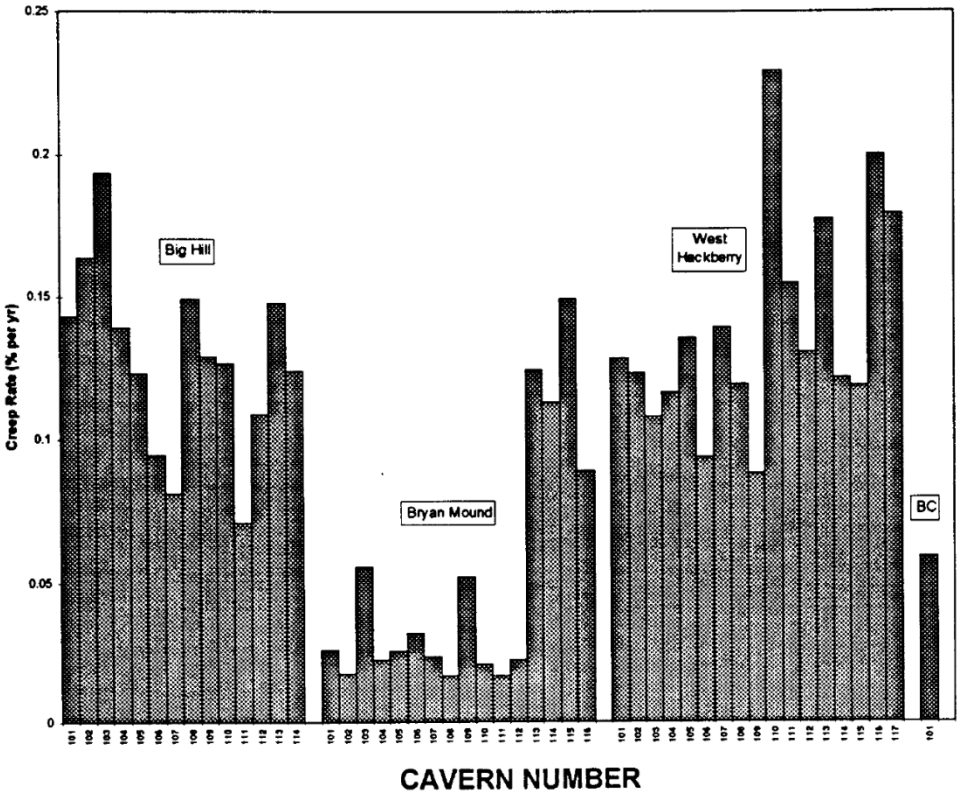

Figure 24. Caveman calculated volume creep rates for SPR caverns [Linn, 1997]

The input parameter values in the Adagio input deck are listed in Table 3. The parameter values for Mechanism 0 in Eq. (3) have been estimated by Reedlunn [2018] for modeling the closure of WIPP rooms. His values for the Mechanism 0 parameters are A_0=56.17 sec^{-1}, Q_0=10000 cal/mol, n_0=1.595. Figure 25 shows how the implementation of the low deviatoric stress mechanism would change the steady-state strain rate as a function of stress, while using both original Munson properties for Big Hill salt and the properties listed in Table 3 for the other mechanisms. The M-D viscoplastic model in this study uses the same parameter values for the Mechanism 0 as those of Reedlunn [2018]. This allows a direct comparison of the simulation of the same creep properties using both models. The parameter values for Mechanism 3 in M-D viscoplastic are zero i.e., Mechanism 3 is ignored. Mechanism 3 is only activated when $\overline{\sigma}$ exceeds $\overline{\sigma}_{\mathrm{g}}$. Therefore, the results from both models are expected to be close each other.

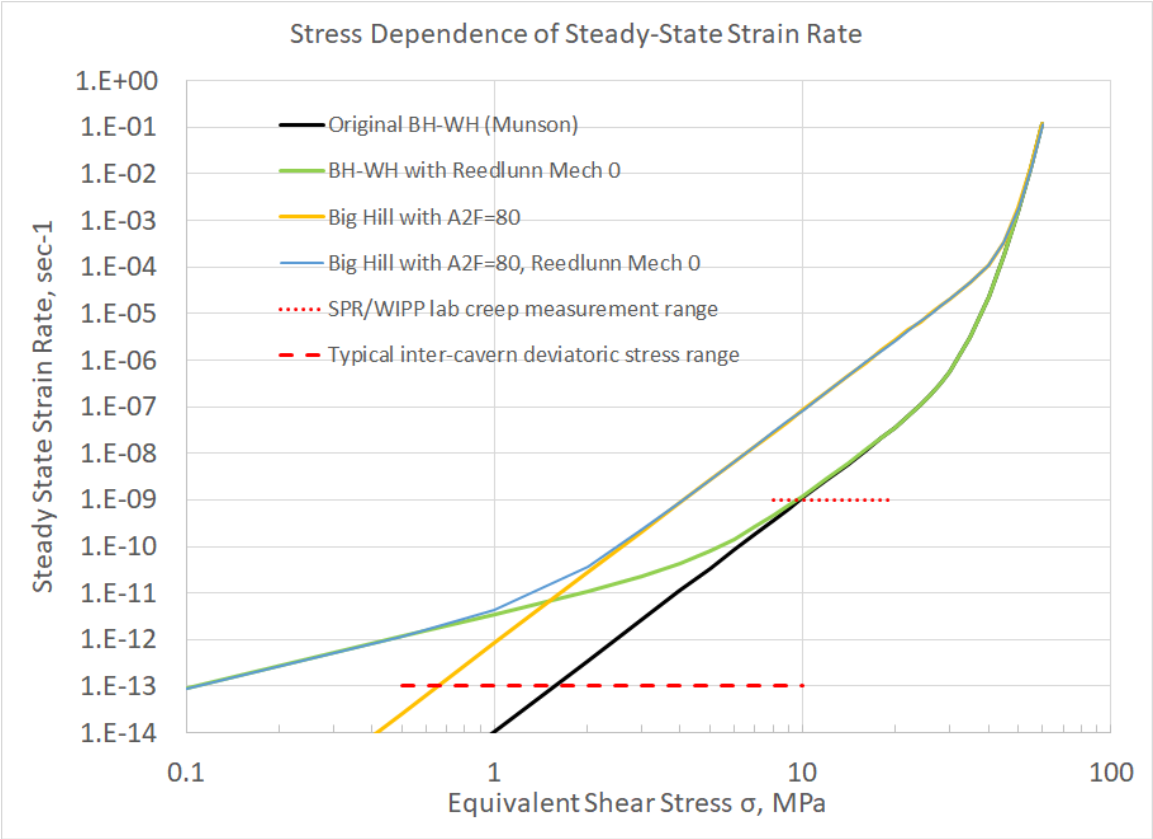

Figure 25. Effect of additional low deviatoric stress component in M-D viscoplastic model [Park, 2020].

Table 3. Comparison of parameter values for Big Hill salt dome using Munson-Dawson (M-D) Calibration 3B [Reedlunn, 2018], M-D Viscoplastic models, and M-D creep [Park, 2021].

Mechanism	Parameter	Symbol	Unit	M-D Cal 3B (1)	BH M-D Viscoplastic (2)	BH M-D (3)
Conventional	Gravity	gr	ft/s^2	32.174 (9.81 m/s^2)	Same as left	Same as left
	Universal gas cnst.	R	cal/(mol·R)	1.103	Same as left	Same as left
	Temperature	T	R	Varies with depth*	Same as left	Same as left
	Thermal expansion	α	1/R	$45x10^{-6}$	0.0	N/A
	Density	ρ	lb/ft^3	143.58** (2300 kg/m^3)	Same as left	Same as left
Elasticity	Young's modulus	E	psf	647,447,400 (31.0 GPa)	Same as left	Same as left
	Poisson's ratio	v	-	0.25	Same as left	Same as left
	Shear modulus	μ	psf	258,978,960 (12.4 GPa)	Same as left	Same as left
	Bulk modulus	B	psf	431,632,307 (20.7 GPa)	Same as left	Same as left
	Hosford stress exp.	a	-	16.0	100	N/A
Mechanism 0, Steady-state creep at low equivalent stresses (< 8 MPa) (Eq. 3)	Structure factor	$\boldsymbol{A_0}$	1/s	$5.617x10^1$	**$5.617x10^1$**	N/A
	Activation energy	Q_0	cal/mol	10,174‡	10,174‡	N/A
	Stress exponent	n_0	-	1.595	1.595	N/A
Mechanism 1, Dislocation climb, it dominates at high temp. and low stress (Eq. 3)	Structure factor	A_1	1/s	8.386×10^{22}	9.812×10^{22}++	Same as left
	Activation energy	Q_1	cal/mol	25,000‡	Same as left	Same as left
	Stress exponent	n_1	-	5.5	Same as left	Same as left
Mechanism 2, It dominates at low temperature and medium stresses (Eq. 3)	Structure factor	$\boldsymbol{A_2}$	1/s	4.415×10^{16}	**1.132×10^{13}**++	Same as left
	Activation energy	Q_2	cal/mol	10,174‡	10,000++	Same as left
	Stress exponent	n_2	-	6.279	5++	Same as left
Mechanism 3, Dislocation glide, which only activated when $\bar{\sigma} > \bar{\sigma}_g$ (Eq. 4)	Stress limit	$\bar{\sigma}_g$	psf	429,613 (20.57 MPa)	Same as left	Same as left
	Structure factor	B_0	1/s	0	0	N/A
	Structure factor	B_1	1/s	$6.086x10^6$	0	$7.123x10^6$
	Structure factor	B_2	1/s	$3.034x10^{-2}$	0	$3.551x10^{-2}$
	Stress constant	q	-	5335	0	5335
Transient strain (Eq. 5, 6, 9, 10)	Material constant	K_0	-	$5.277x10^{-2}$	0	N/A
	Material constant	c_0	1/R	$8.882x10^{-3}$	0	N/A
	Material constant	m_0	-	0.9201	0	N/A
	Material constant	$\boldsymbol{K_1}$	-	$3.052x10^{12}$	**$6.275x10^5$**++	Same as left
	Material constant	c_1	1/R	$8.882x10^{-3}$	0.00511++	Same as left
	Material constant	m_1	-	5.282	3++	Same as left
Work-hardening and recovery (Eq. 7)	Model parameter	α_h	-	3.367	-17.37++	Same as left
	Model parameter	β_h	-	-0.6838	-7.738++	Same as left
	Model parameter	α_r	-	0.58	0.58++	Same as left
	Model parameter	β_r	-	0.0	0.0++	Same as left
Structure factor multi factor from WIPP 25°C salt		*SMF*	-	N/A	1.17++	Same as left

Note:
* – Temperature value is assigned on every node in the mesh
** -The value (lb/ft^3/gr) will be divided by gravity (32.174 ft/s^2) in the system
‡ – Adagio requests the value be divided by universal gas constant
++ – The values in Table V [Munson, 1998]
The bold parameters indicate the base values used for the calibration

5.2. Lithologies Encompassing Salt

The surface overburden layer, which is mostly comprised of sandy soil, is modeled as exhibiting linear elastic material behavior. The layer is considered isotropic and homogeneous and has no assumed failure criteria. The upper caprock layer, consisting of gypsum and limestone, is also assumed to be linear elastic, homogeneous, and isotropic. The rock surrounding the salt dome is assumed to be isotropic, homogeneous, linear elastic sandstone as well.

The anhydrite in the lower caprock layer is expected to experience inelastic material behavior. The anhydrite layer is considered isotropic and elastic until yield occurs [Butcher, 1997]. Once the yield stress is reached, plastic strain begins to accumulate. Yield is assumed to be governed by the Drucker-Prager (D-P) criterion:

$$\sqrt{J_2} = C - aI_1 \tag{11}$$

where $I_1 = \sigma_1 + \sigma_2 + \sigma_3 = 3\sigma_m$ is the first invariant of the stress tensor and

$\sqrt{J_2} = \sqrt{\frac{(\sigma_1 - \sigma_2)^2 + (\sigma_2 - \sigma_3)^2 + (\sigma_3 - \sigma_1)^2}{6}}$ is the square root of the second invariant of the deviatoric stress tensor; σ_1, σ_2, and σ_3 are the maximum, intermediate, and minimum principal stresses, respectively; σ_m is the mean stress; and C and a are D-P constants.

The material properties of the BH anhydrite are not known. Therefore, the behavior of the BH anhydrite is assumed to be the same as the WIPP anhydrite. A non-associative flow rule is used to determine the plastic strain components. "soil_foam" model in Adagio is used for the lower caprock. The input parameters, A_0 and A_1, are derived from the elastic properties and the D-P constants, C and a [Park et al., 2005].

The material properties for the lithologies overlying and surrounding the BH salt dome used as input data for the SNL-developed 3D solid mechanics codes used in the present analyses, Adagio, are listed in Table 4.

Table 4. Material properties of lithologies around salt dome used in the analyses.

		Unit	Overburden (Sandy soil)	Caprock 1 (Limestone and gypsum)	Caprock 2 (Anhydrite)	Surrounding Rock (Sandstone)
Young's modulus (E)		psf	2,088,543 (0.1 GPa)	438,594,119 (21 GPa)	1,568,496,111 (75.1 GPa)	1,461,980,396 (70 GPa)
Density (ρ)		lb/ft^3	116.99 (1874 kg/m^3)	156.07 (2500 kg/m^3)	143.58 (2300 kg/m^3)	156.07 (2500 kg/m^3)
Poisson's ratio (v)		-	0.33	0.29	0.35	0.33
Drucker-Prager constants	C	psf	N/A	N/A	28,195 (1.35 MPa)	N/A
	a	-	N/A	N/A	0.45	N/A
Bulk modulus (K)		psf	N/A	N/A	1,742,773,456 (83.44 GPa)	N/A
Shear modulus (μ)		psf	N/A	N/A	580,924,485 (27.82 GPa)	N/A
Soil and forms model constants	A_0	psf	N/A	N/A	48,836 (2.338 MPa)	N/A
	A_1	-	N/A	N/A	2.338	N/A
	A_2	-	N/A	N/A	0	N/A
References		-	[Hoffman and Ehgartner, 1992]	[Hoffman and Ehgartner, 1992]	[Butcher, 1997]	[Lama and Vutukuri, 1978]

5.3. Interbed and Interface

Adagio has a contact surface algorithm for modeling contact and sliding behavior between two solid surfaces as described in Sections 3.4.3 through 3.4.5. The overburden material properties (Table 5) are used for the interbed block.

The interface between the dome and surrounding rock is a vertical layer, while the interbed is a horizontal layer. In this analysis, it is assumed that the interface behaves like a thin, soft element layer in a manner like the interbed, but the horizontal pressure applied on the dome surface must be the same as it arises from the surrounding rock. Therefore, the density and Poisson's ratio of the surrounding rock are used for the pseudo material of the interface. To implement a soft element, 1% of the surrounding rock's elastic modulus is used for the interface. The mechanical properties used in the analysis are listed in Table 5.

Table 5. Material properties of the interbed and interface used in the analysis.

	Unit	Interbed	Interface
Young's modulus	psf	2,088,543 (0.1 GPa)	14,619,804 (0.7 GPa)
Density	lb/ft^3	116.99 (1874 kg/m^3)	156.07 (2500 kg/m^3)
Poisson's ratio	-	0.33	0.33

This page left blank

6. PARAMETER EFFECT

The structure factor A_0, A_2, in Eq. (3) and transient strain limit factor, K_1 in Eq. (10) in the M-D viscoplastic constitutive model are used for the calibration. The parameter values for Mechanism 0 in Eq. (3) have been estimated by Reedlunn [2018] for modeling the closure of WIPP rooms. The value for the Mechanism 0 parameter is A_0=56.17 sec^{-1} as mentioned in Section 5.1.2. The A_2 value obtained experimentally from the BH salt as shown Figure 23. The value for the Mechanism 2 parameter is A_2=1.132×10^{13} s^{-1}. K_1 value for the transient strain limit is K_1=6.275×10^5, which was obtained from WIPP salt, as the baseline values listed in Table 3.

The volumetric closure normalized to initial cavern volumes calculated using the original M-D constitute model, which did not consider Mechanism 0, are shown in Figure 26 [Park, 2018]. The values listed in column (3) of Table 3 were used. The solid and dotted lines indicate the results from the M-D model and Caveman (CM) calculations, respectively. For all simulations, the calculated volumetric closures are much smaller than the CM results. The magnitude of the sudden increases (called "jumps" hereafter) in cavern volumetric closure during workovers is a function of both A_1 and A_2, but also of the transient creep phenomenon which is governed by the factor K_1 in Eq. (10) [Sobolik, 2015].

The M-D viscoplastic contact surface (VCS) model, which uses the M-D viscoplastic constitute model for the salt and the mesh containing the interbed layer with contact surfaces between the salt and caprock layers, is used in this study. The VCS model used the values originally suggested by Munson [1998] and Reedlunn [2018] for the BH salt as listed in column (2) of Table 3. Figure 27 shows the volumetric closure normalized to initial cavern volumes calculated from the VCS model and the CM. The colorful solid and dotted curves indicate the predictions from the VCS model and CM calculations, respectively. In all caverns, the volumetric closures calculated from the VCS model match the CM's better than the original M-D model's in Figure 26. This might be because the VCS model considers the steady-state creep at low stress states (Mechanism 0), and the sliding mechanism between the caprock and salt, and fault blocks through contact surfaces.

Park [2021] compared the volumetric closures calculated from the VCS model and the viscoplastic soft element (VSE) model which has the interbed between the caprock and salt layers, but no contact surfaces. The results showed that the volumetric closures from the VCS were closer to that of the CM than those calculated from VSE for the most caverns. This implies that the VCS model is closer to reality than the VSE model in implementing the cavern volume calculation. One possible explanation for this is that the additional of contact surface slip may increase the equivalent stresses in the salt surrounding the caverns, which would enhance the low stress creep mechanism and cause larger predicted volume closures.

Anyhow, the results for BH106, BH107, BH108, BH111, and BH114 do not agree well. Therefore, the calibration of the parameter values is needed to match the simulation model to the field environment. To adjust the magnitude of A_0, A_2, and K_1, multiplication factors *A0F*, *A2F* and *K1F* are defined as listed in Table 6, respectively. The values for BH salt in Table 3 are converted into the Adagio input format. The values of the multiplication factors of the salt dome and each SPR cavern cylinder column as shown in Figure 17 have been determined through several back fitting analyses.

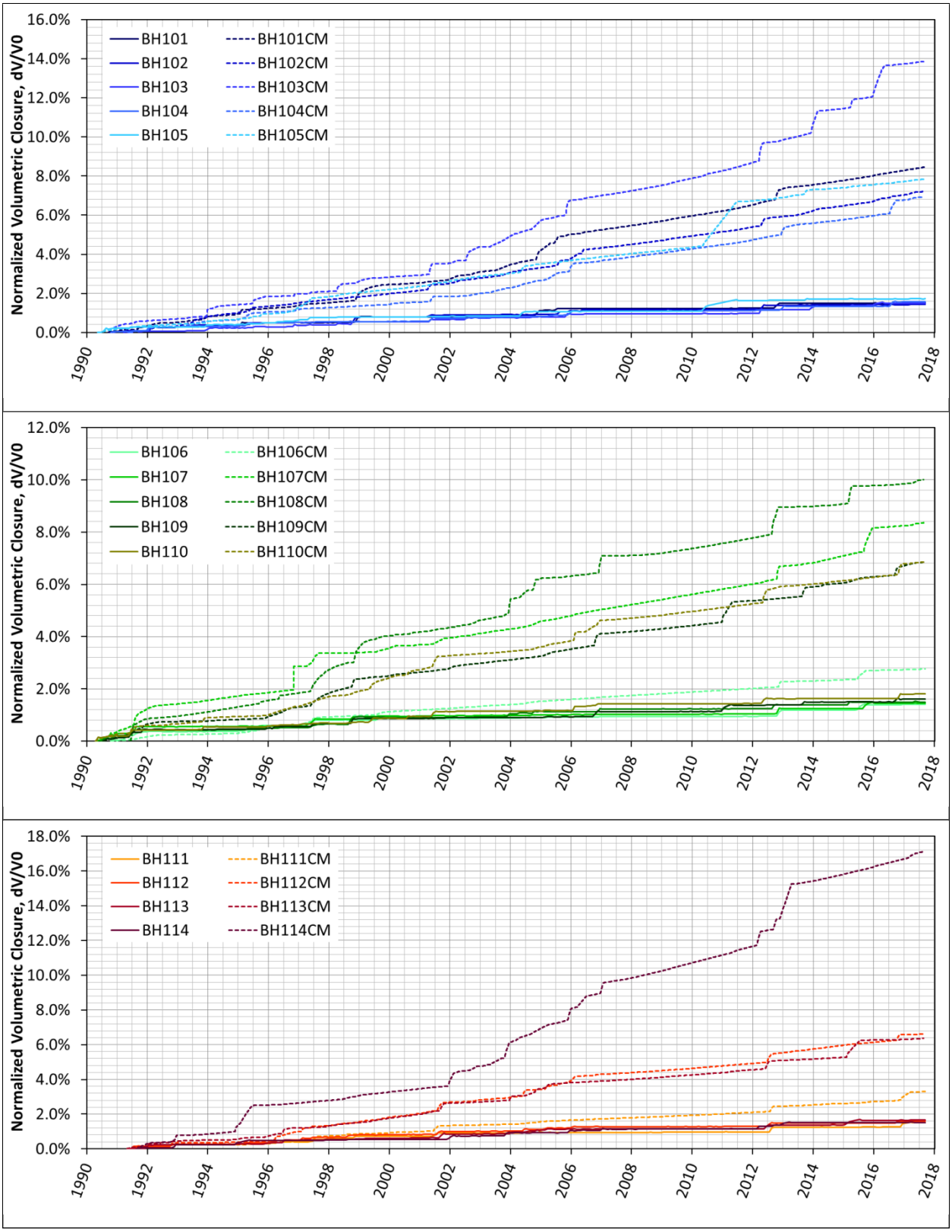

Figure 26. Volumetric closure normalized to initial volume calculated using the baseline parameter values and Caveman predictions for BH101 through BH114 [Park, 2018]

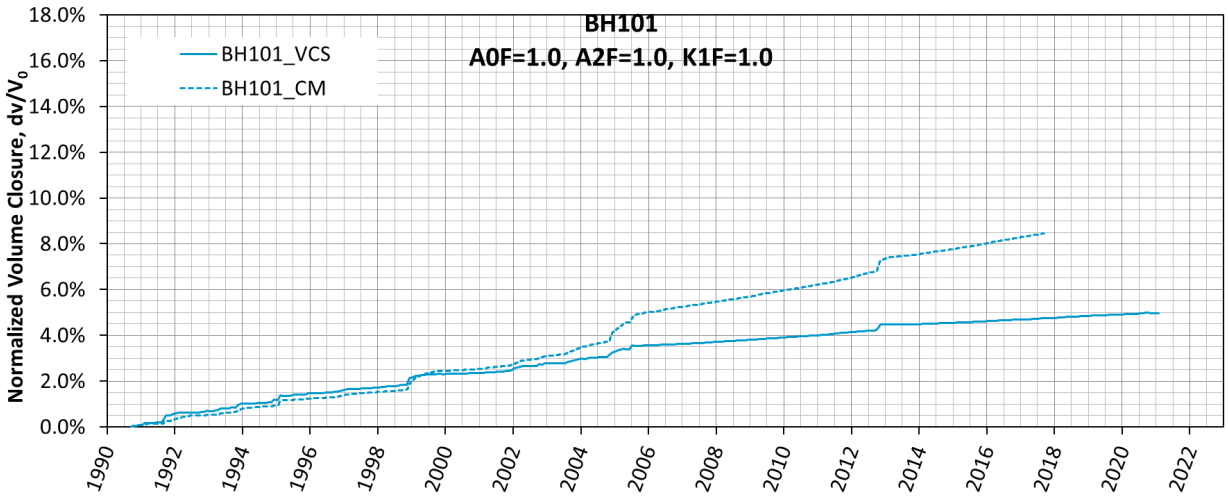
BH101
A0F=1.0, A2F=1.0, K1F=1.0
BH101_VCS
BH101_CM
Normalized Volume Closure, dv/V0
18.0%
16.0%
14.0%
12.0%
10.0%
8.0%
6.0%
4.0%
2.0%
0.0%
1990
1992
1994
1996
1998
2000
2002
2004
2006
2008
2010
2012
2014
2016
2018
2020
2022

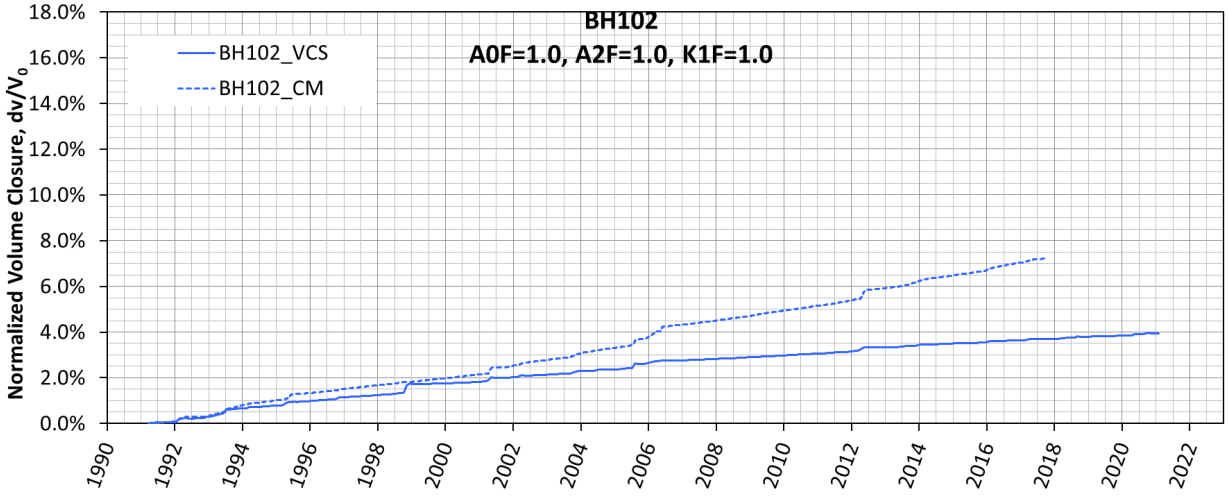
BH102
A0F=1.0, A2F=1.0, K1F=1.0
BH102_VCS
BH102_CM
Normalized Volume Closure, dv/V0
18.0%
16.0%
14.0%
12.0%
10.0%
8.0%
6.0%
4.0%
2.0%
0.0%
1990
1992
1994
1996
1998
2000
2002
2004
2006
2008
2010
2012
2014
2016
2018
2020
2022

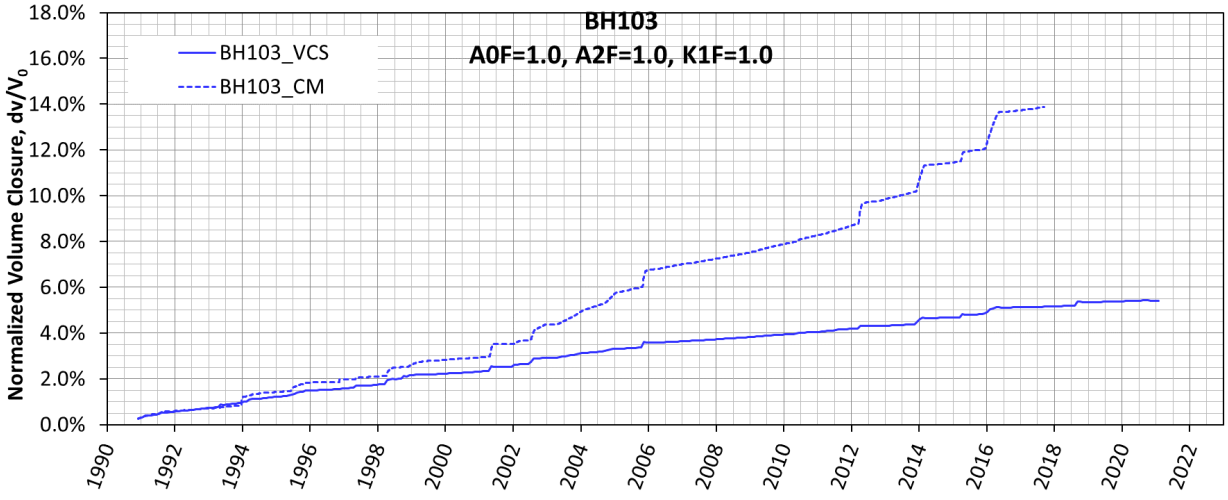
BH103
A0F=1.0, A2F=1.0, K1F=1.0
BH103_VCS
BH103_CM
Normalized Volume Closure, dv/V0
18.0%
16.0%
14.0%
12.0%
10.0%
8.0%
6.0%
4.0%
2.0%
0.0%
1990
1992
1994
1996
1998
2000
2002
2004
2006
2008
2010
2012
2014
2016
2018
2020
2022

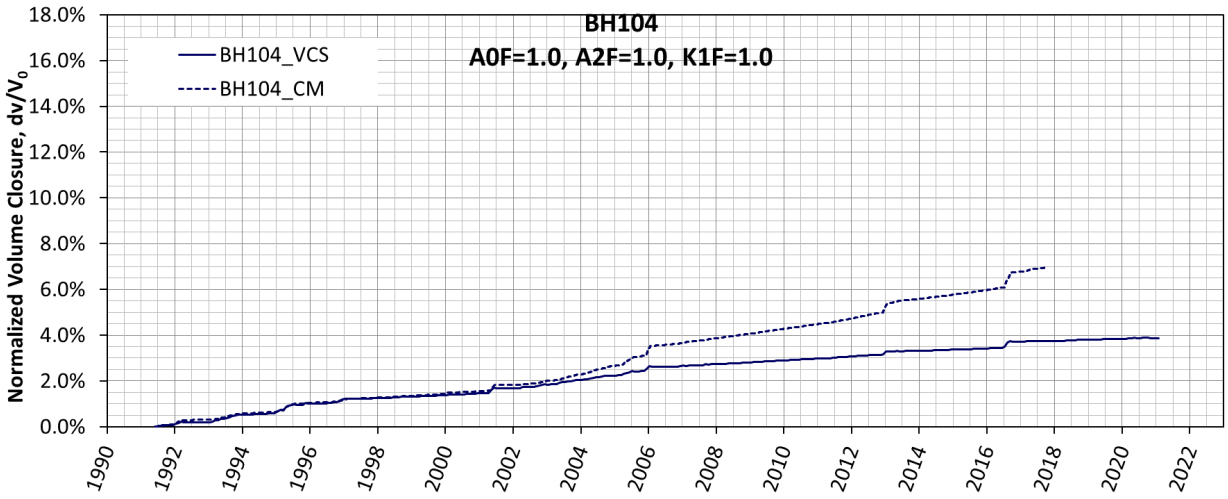
BH104
A0F=1.0, A2F=1.0, K1F=1.0
BH104_VCS
BH104_CM
Normalized Volume Closure, dv/V0
18.0%
16.0%
14.0%
12.0%
10.0%
8.0%
6.0%
4.0%
2.0%
0.0%
1990
1992
1994
1996
1998
2000
2002
2004
2006
2008
2010
2012
2014
2016
2018
2020
2022

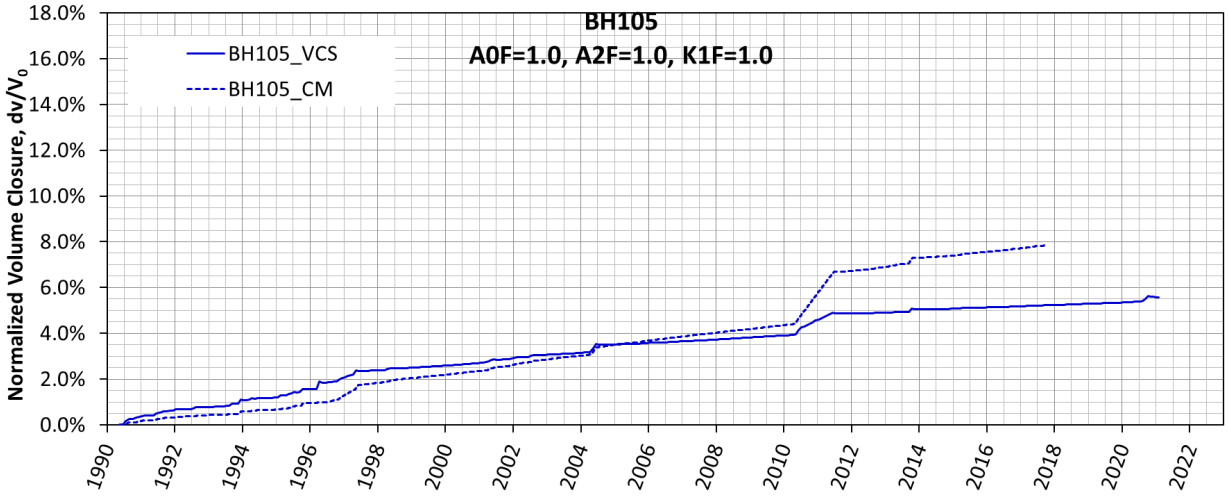
BH105
A0F=1.0, A2F=1.0, K1F=1.0
BH105_VCS
BH105_CM
Normalized Volume Closure, dv/V0
18.0%
16.0%
14.0%
12.0%
10.0%
8.0%
6.0%
4.0%
2.0%
0.0%
1990
1992
1994
1996
1998
2000
2002
2004
2006
2008
2010
2012
2014
2016
2018
2020
2022

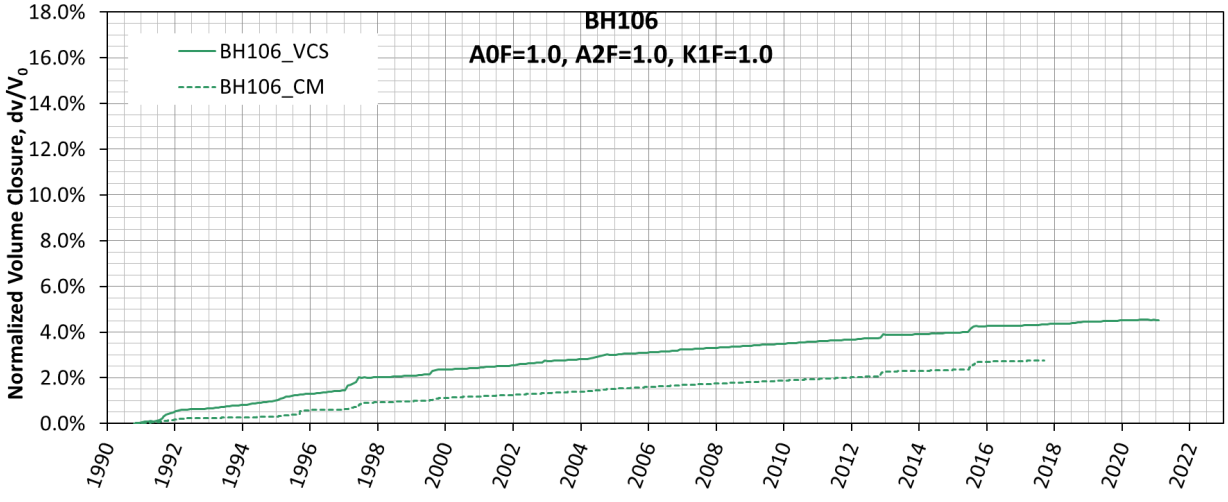
BH106
A0F=1.0, A2F=1.0, K1F=1.0
BH106_VCS
BH106_CM
Normalized Volume Closure, dv/V0
18.0%
16.0%
14.0%
12.0%
10.0%
8.0%
6.0%
4.0%
2.0%
0.0%
1990
1992
1994
1996
1998
2000
2002
2004
2006
2008
2010
2012
2014
2016
2018
2020
2022

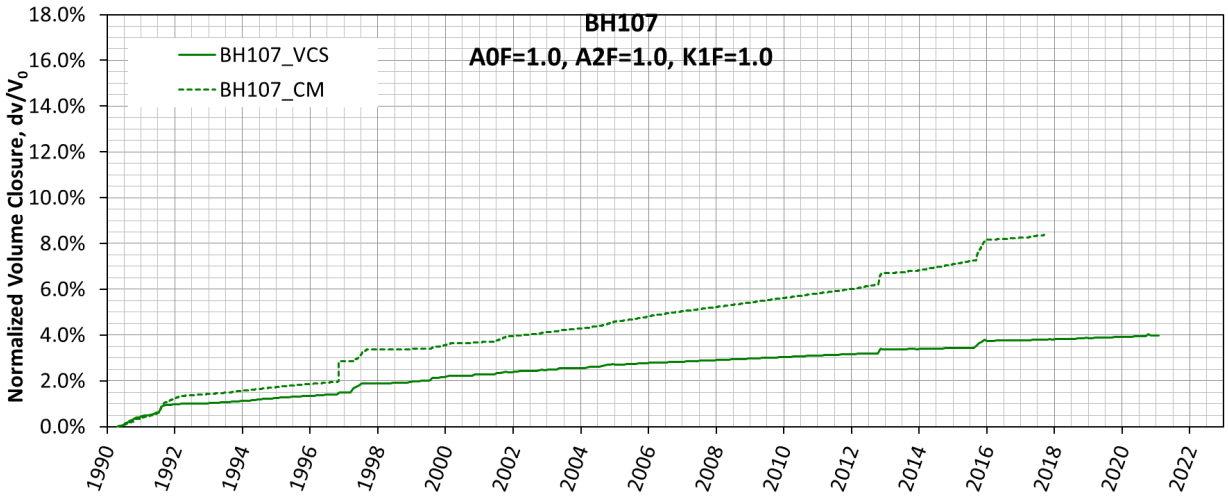
BH107
A0F=1.0, A2F=1.0, K1F=1.0
BH107_VCS
BH107_CM
Normalized Volume Closure, dv/V0
18.0%
16.0%
14.0%
12.0%
10.0%
8.0%
6.0%
4.0%
2.0%
0.0%
1990
1992
1994
1996
1998
2000
2002
2004
2006
2008
2010
2012
2014
2016
2018
2020
2022

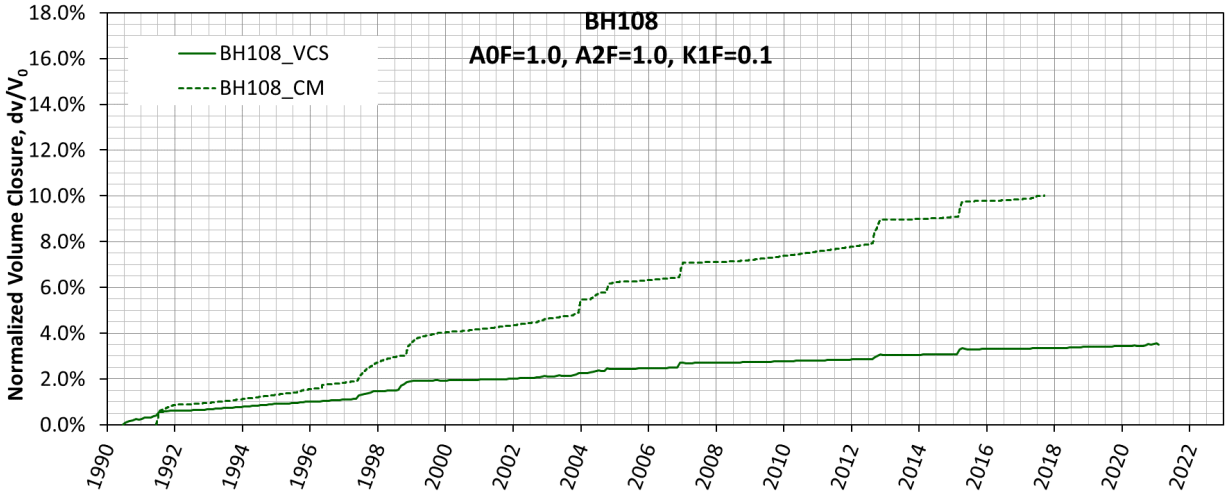
BH108
A0F=1.0, A2F=1.0, K1F=0.1
BH108_VCS
BH108_CM
Normalized Volume Closure, dv/V0
18.0%
16.0%
14.0%
12.0%
10.0%
8.0%
6.0%
4.0%
2.0%
0.0%
1990
1992
1994
1996
1998
2000
2002
2004
2006
2008
2010
2012
2014
2016
2018
2020
2022

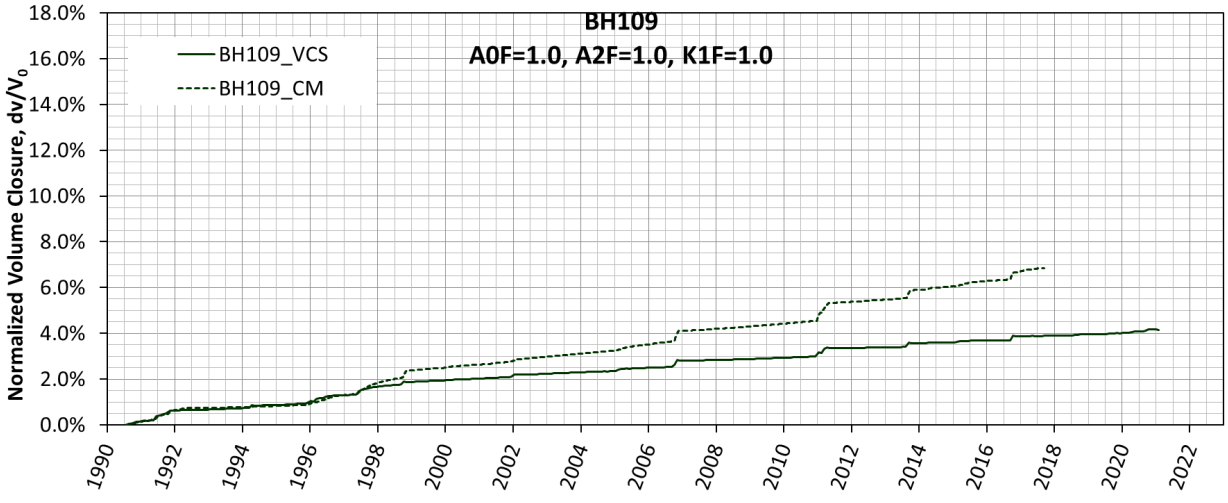
BH109
A0F=1.0, A2F=1.0, K1F=1.0
BH109_VCS
BH109_CM
Normalized Volume Closure, dv/V0
18.0%
16.0%
14.0%
12.0%
10.0%
8.0%
6.0%
4.0%
2.0%
0.0%
1990
1992
1994
1996
1998
2000
2002
2004
2006
2008
2010
2012
2014
2016
2018
2020
2022

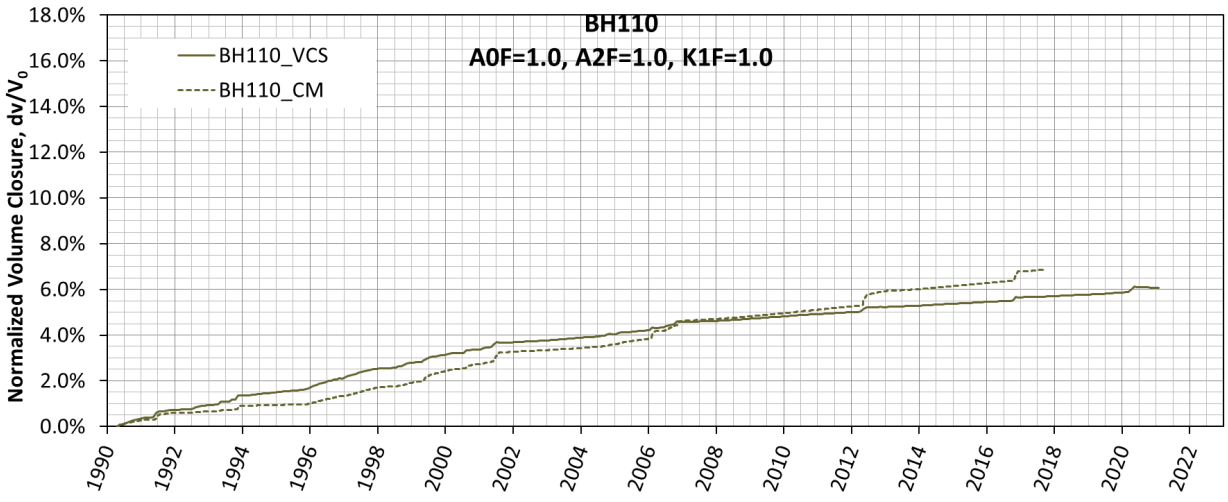
BH110
A0F=1.0, A2F=1.0, K1F=1.0
BH110_VCS
BH110_CM
Normalized Volume Closure, dv/V0
18.0%
16.0%
14.0%
12.0%
10.0%
8.0%
6.0%
4.0%
2.0%
0.0%
1990
1992
1994
1996
1998
2000
2002
2004
2006
2008
2010
2012
2014
2016
2018
2020
2022

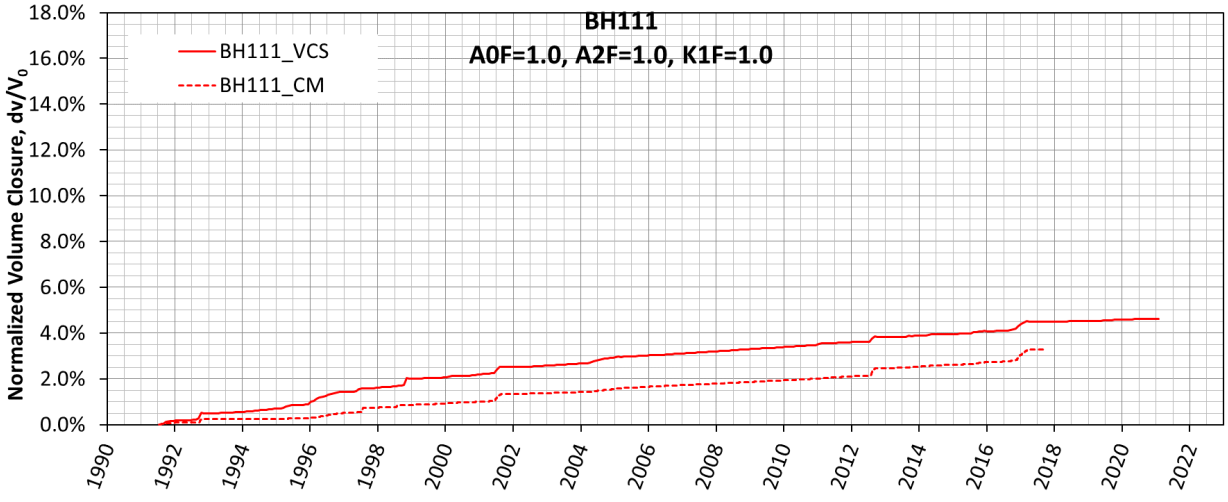
BH111
A0F=1.0, A2F=1.0, K1F=1.0
BH111_VCS
BH111_CM
Normalized Volume Closure, dv/V0
18.0%
16.0%
14.0%
12.0%
10.0%
8.0%
6.0%
4.0%
2.0%
0.0%
1990
1992
1994
1996
1998
2000
2002
2004
2006
2008
2010
2012
2014
2016
2018
2020
2022

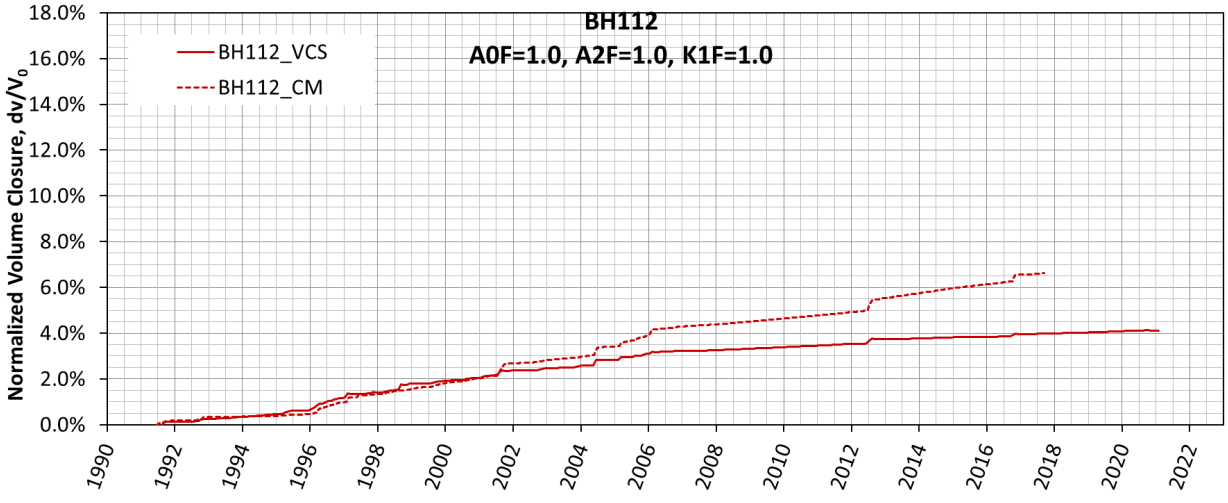
BH112
A0F=1.0, A2F=1.0, K1F=1.0
BH112_VCS
BH112_CM
Normalized Volume Closure, dv/V0
18.0%
16.0%
14.0%
12.0%
10.0%
8.0%
6.0%
4.0%
2.0%
0.0%
1990
1992
1994
1996
1998
2000
2002
2004
2006
2008
2010
2012
2014
2016
2018
2020
2022

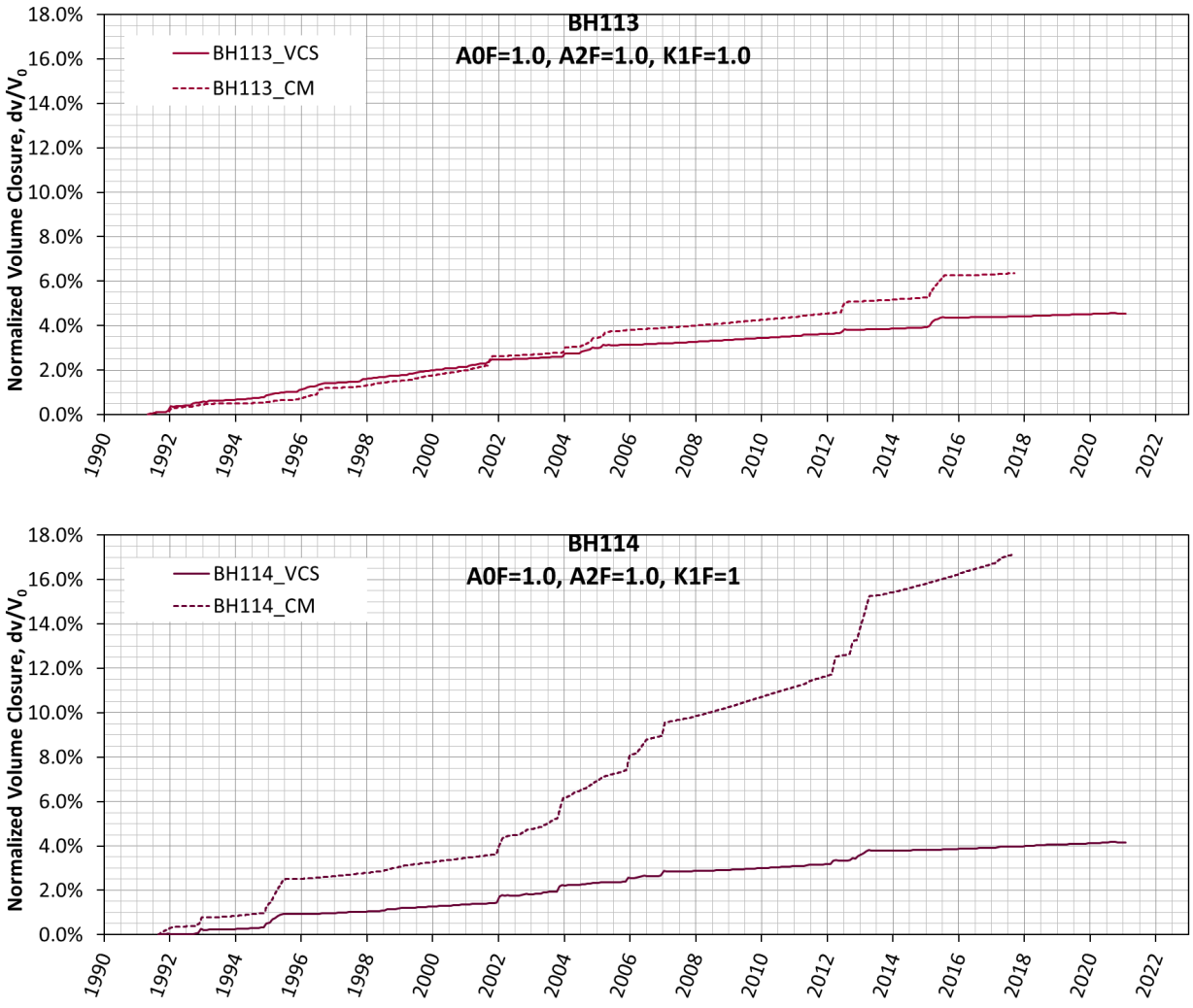

Figure 27. Volumetric closure normalized to initial cavern volumes calculated from the viscoplastic contact surface model (VCS) with no calibrated parameter values, and Caveman (CM) for 14 SPR caverns. The colorful solid curves and colorful dot curves indicate the predictions from the VCS and Caveman calculations, respectively.

Table 6. Parameter values used in Adagio input deck for M-D Viscoplastic and M-D creep for Big Hill salt.

Mechanism	Parameter	Symbol	Unit	BH M-D Viscoplastic	BH M-D
Conventional	Gravity	gr	ft/s^2	32.174 (9.81 m/s^2)	Same as left
	Universal gas cnst.	R	cal/(mol·R)	1.103	Same as left
	Temperature	T	R	Varies with depth*	Same as left
	Thermal expansion	α	1/R	0.0	N/A
	Density	ρ/gr	$lb{\cdot}s^2/ft^4$	4.4626** (2300 kg/m^3)	Same as left
Elasticity	Young's modulus	E	psf	647,447,400 (31.0 GPa)	Same as left
	Poisson's ratio	v	-	0.25	Same as left
	Shear modulus	μ	psf	258,978,960 (12.4 GPa)	Same as left
	Bulk modulus	B	psf	431,632,307 (20.7 GPa)	Same as left
	Hosford stress exp.	a	-	100	N/A
Mechanism 0, Steady-state creep at low equivalent stresses (< 8 MPa) (Eq. 3)	Structure factor	$\boldsymbol{A_0}$	1/s	***A0F***†**×56.17**	N/A
	Activation energy	Q_0/R	R	9226.6‡	N/A
	Stress exponent	n_0	-	1.595	N/A
Mechanism 1, Dislocation climb, it dominates at high temp. and low stress (Eq. 3)	Structure factor	A_1	1/s	9.812×10^{22}††	Same as left
	Activation energy	Q_1/R	R	22660‡	Same as left
	Stress exponent	n_1	-	5.5	Same as left
Mechanism 2, It dominates at low temperature and medium stresses (Eq. 3)	Structure factor	$\boldsymbol{A_2}$	1/s	***A2F***††**×1.132×10^{13}**	Same as left
	Activation energy	Q_2/R	R	9064.0‡	Same as left
	Stress exponent	n_2	-	5	Same as left
Mechanism 3, Dislocation glide, which only activated when $\bar{\sigma} > \bar{\sigma}_g$ (Eq. 4)	Stress limit	$\bar{\sigma}_g$	psf	429,613 (20.57 MPa)	Same as left
	Structure factor	B_0	1/s	0	N/A
	Structure factor	B_1	1/s	0	$7.123\text{x}10^{6}$
	Structure factor	B_2	1/s	0	$3.551\text{x}10^{-2}$
	Stress constant	q	-	0	5335
Transient strain (Eq. 5, 6, 9, 10)	Material constant	K_0	-	0	N/A
	Material constant	c_0	1/R	0	N/A
	Material constant	m_0	-	0	N/A
	Material constant	$\boldsymbol{K_1}$	-	***K0F***†††**×6.275x10^{5}**	Same as left
	Material constant	c_1	1/R	0.00511	Same as left
	Material constant	m_1	-	3	Same as left
Work-hardening and recovery (Eq. 7)	Model parameter	α_h	-	-17.37	Same as left
	Model parameter	β_h	-	-7.738	Same as left
	Model parameter	α_r	-	0.58	Same as left
	Model parameter	β_r	-	0.0	Same as left
Structure factor multi factor from WIPP 25°C salt		*SMF*‡‡	-	1.17	Same as left

Note:
* – Temperature value is assigned on every node in the mesh
** -The value (lb/ft^3/gr) will be multiplied by gravity (32.174 ft/s^2) in the system
‡ – Adagio requests the value be divided by universal gas constant
† – A_0 multiplication factor to examine the A_0 factor effect
†† – A_2 multiplication factor to examine the A_2 factor effect
††† - K_0 multiplication factor to examine the K_0 factor effect
‡‡*SMF* = $A_{2\ \text{BH Salt}}$ / $A_{2\ \text{WIPP Salt}}$, A_1, B_1, and B_2 of BH salt are multiplied those of WIPP salt by *SMF* [Munson, 1998]
The bold parameters indicate the values used for the calibration

To examine the effect of changing A_0 on cavern volumetric closure, the cavern volume decrease rates are calculated with several A_0 values while the other parameter values are not changed. The multiplier *A0Fs* with *A2F*=1 and *K1F*=1 is applied to all the salt blocks such as the salt dome and cavern column. Figure 28 shows the relationship between the slope and various *A0F* values when *A2F*=1 and *K1F=1*. The cavern volumetric closure rates are calculated for *A0F*= 0.1, 0.2, 1, 2, 10, 20, and 40. The rates increase as the *A0F*s increase until approximately *A0F*=10, and then continue to increase for some caverns or decrease for other caverns.

Figure 29 shows the relationship between the slope and *A2F* when *K1F*=1.0 in the M-D model which does not consider Mechanism 0 (viscoplastic) [Park, 2018]. Note that the notation of K_0 in the original M-D model is changed to K_1 because K_0 is used for Mechanism 0 as mentioned in Section 5.1.1. Thus, the related multiplication factor *K0F* also changed to *K1F*. The cavern volumetric closure rates were calculated for *A2F*=1, 10, 20, 40, 60, 80, 100, 200, 500, and 1000. The rates increase as the *A2F*s increase until approximately *A2F*=80, and then continue to increase for BH103 and BH114 or decrease for the other 12 caverns.

In similar manner, the cavern volumetric closure rates are calculated with several *K1F* values while other parameter values are not changed to examine the effect of K_1. Figure 30 show the relationship between the cavern volumetric closure rates and *K1F* when *A2F*=100 in the M-D model. The rates are calculated for *K1F* = 1, 2, 4, 8, and 16. The cavern volumetric closure rate slightly increases/decreases when *K1F* increases. Changing the K_1 value does not affect the cavern volumetric closure rate much [Park, 2018].

This relationships between the cavern volumetric closure rates and *A0F*, *A2F*, and *K1F* are used for the model calibration.

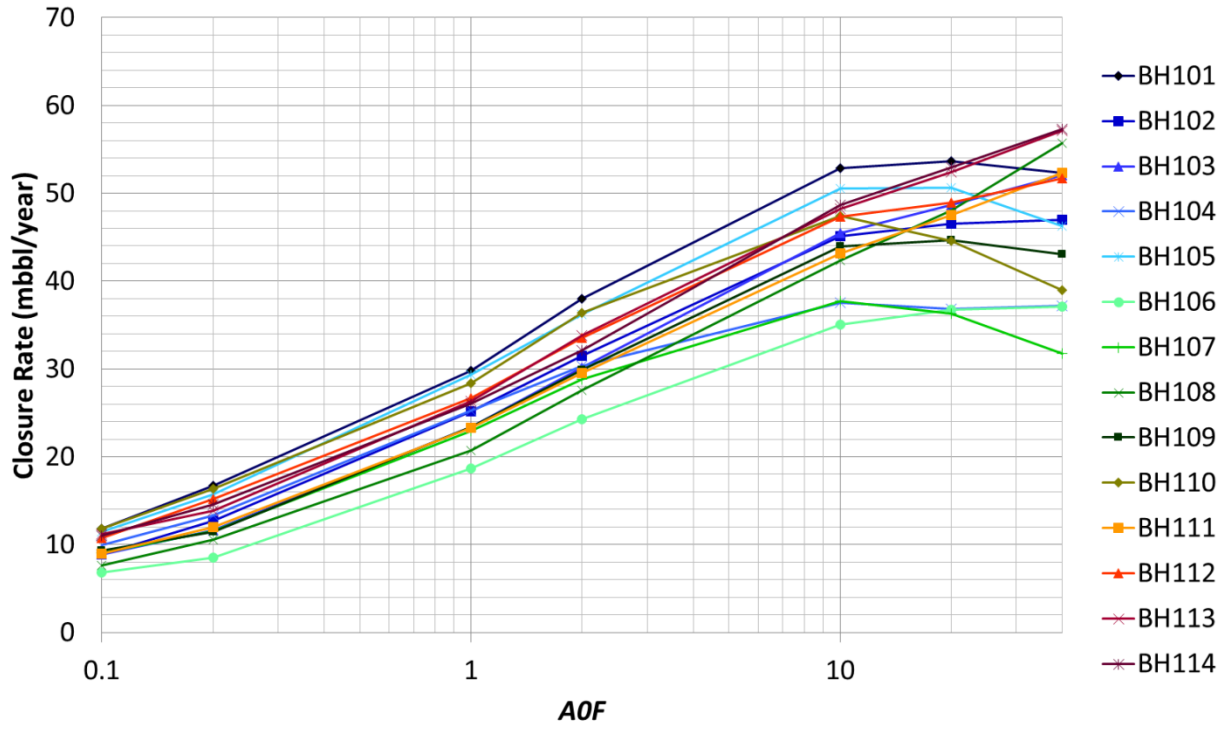

Figure 28. Relationship between *A0F* and cavern volume closure rate when *A2F*=1 and *K0F*=1 for 14 caverns for M-D viscoplastic slat model.

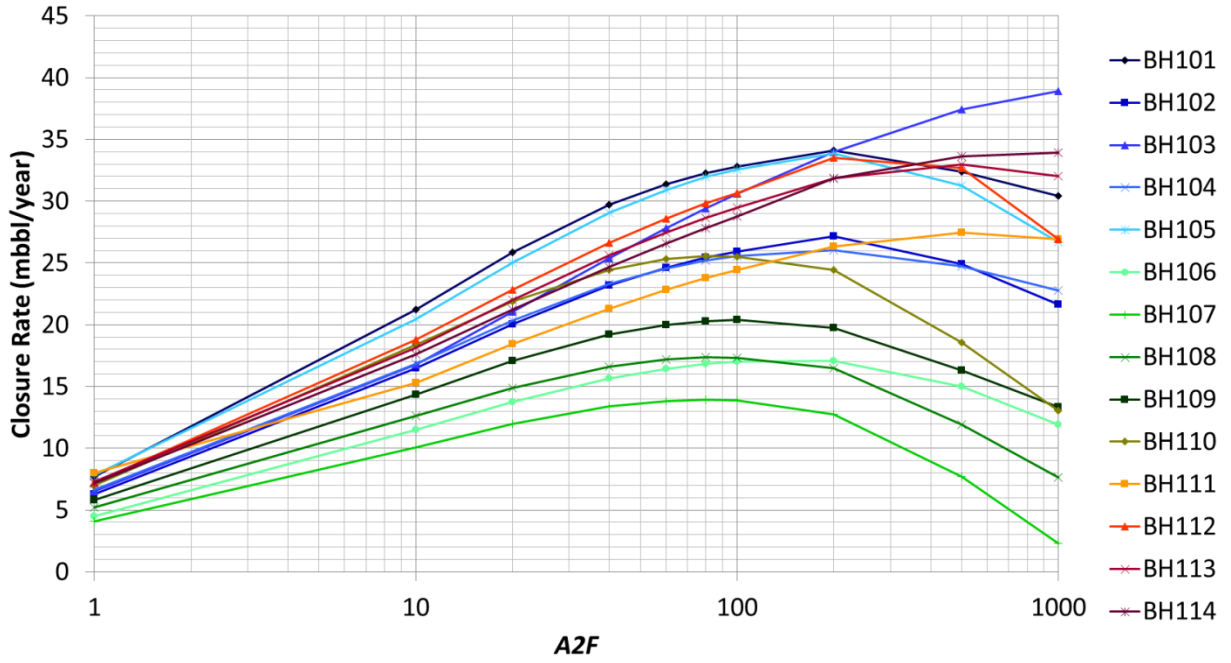

Figure 29. Relationship between *A2F* and cavern volume closure rate when *K0F*=1 for 14 caverns for M-D salt model [Park, 2018].

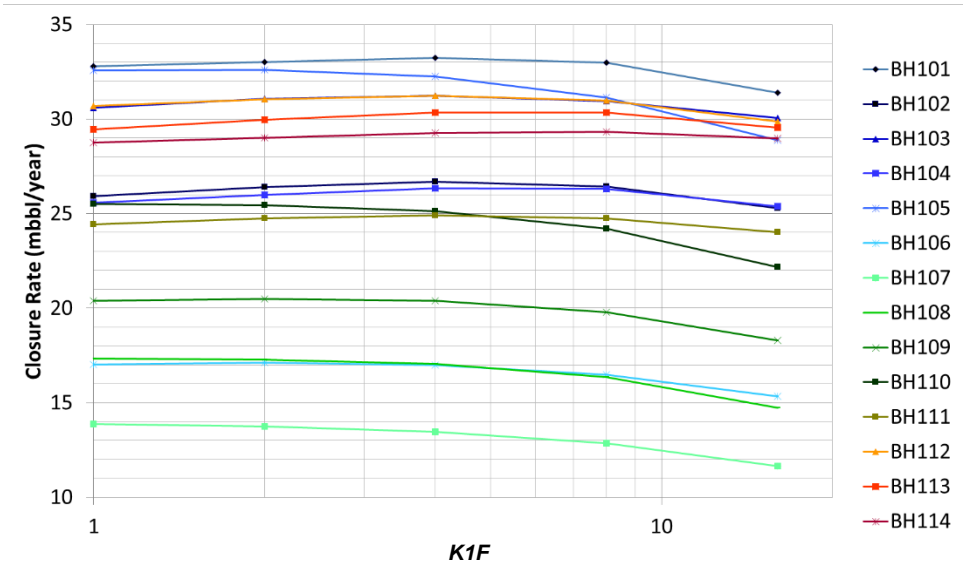

Figure 30. Relationship between *K1F* and cavern volume closure rate when *A2F*=100 for 14 caverns in M-D salt model [Park, 2018].

This page left blank

7. MODEL CALIBRATION

Based on the relationships between the cavern volumetric closure rates and *A0F*, *A2F*, and *K1F* in Figure 28 through Figure 30, the values of *A0F*, *A2F* and *K0F* have been calibrated through a number of back-fitting analyses and determined as listed Table 7. *A0F*=1, *A2F*=1, and *K0F*=1 i.e., the base line values in column (2) of Table 3 are applied to the entire salt dome except the cavern columns in Figure 17. The values of *A0F, A2F,* and *K0F* as listed in Table 7 are applied into the cavern cylinder columns encompassing the cavern cavities. The volumetric closure curves normalized to the initial volumes of SPR caverns calculated from CM as shown Figure 26 are used as a back-fitting standard.

Figure 31 shows the volumetric closure normalized to initial cavern volumes calculated from the VCS model using calibrated *A0F, A2F,* and *K0F* values listed in Table 7, and CM predictions for 14 SPR caverns. In all caverns except BH114, the volumetric closures calculated from the VCS model and CM agree well from 1991, when the caverns began operating, to the early 2000s. But after that, the difference starts to widen. CM's results show that the slope of volumetric closure tends to increase during 2000's compared to them during 1990's.

Figure 32 shows the amount of raw water injected into each cavern with time. The circles in blue and orange indicate the injected raw water and leached salt volumes, respectively. Before 2005, the injected amount was not very large, so there is little change in the volume of the caverns that were leached by the injected raw water. Therefore, it seems to the volumetric closure results up to the early 2000s in most caverns are in good match to CM's results. It may have contributed to the increase in the slope of the CM curve due to the volume of the caverns increased as the raw water injection amount was increased afterwards. However, the amount of injected water does not match the slope increase in normalized cavern closure in the same proportion. In the case of BH114, which did not have much raw water injection, there is a serious difference between them.

One of the issues we are going to have that will make it difficult to compare Caveman and Adagio is that they do different things. Adagio uses either historic or user-specified pressures on the interior surface of the cavern and tests the salt reaction to that. Caveman tries to calculate the increased pressure on the fluid due to salt creep and fluid compressibility to calculate the change in volume in daily increments. Furthermore, whenever a fluid exchange is entered into Caveman, the overall volume of the cavern is changed by that amount; in the case of raw water, an additional 15% of the water volume is added to the cavern. This happens on a "daily" basis in the program. In Adagio, the cavern volume is increased only when a predesigned, meshed block of salt is removed from the calculation. It is not surprising that there is going to be greater discrepancy between Caveman and Adagio during times of frequent fluid movement and raw water injection, although the manner in which they are different in Figure 31 is somewhat perplexing.

In conclusion, Caveman's calculation results could not be consistent with those from the BH geomechanical model. However, it could be used as a reference for examining the calculation results of the model. Since the simulation results up to the early 2000s agree well with Cavemen's results, the results calculated from this model could be used to examine the structural integrity of caverns in BH dome. Another consideration is that Caveman's consistent prediction of significant increases in volume closure rates for most of the caverns, based on recorded wellhead pressure data, may indicate an increase in equivalent stresses in regions around each cavern due to an external cause not yet identified.

Table 7. Calibrated values of multiplication factors applied to the A_0, A_2 and K_1 in Table 6.

Cavern ID	*A0F*	*A2F*	*K1F*
Salt dome except SPR cavern columns	1.0	1.0	1.0
BH101 salt cylinder column	1.0	1.0	1.0
BH102 salt cylinder column	1.0	1.0	1.0
BH103 salt cylinder column	1.0	1.0	1.0
BH104 salt cylinder column	1.0	1.0	1.0
BH105 salt cylinder column	1.0	1.0	1.0
BH106 salt cylinder column	0.3	0.1	1.0
BH107 salt cylinder column	2.0	2.0	1.0
BH108 salt cylinder column	2.0	1.0	1.0
BH109 salt cylinder column	1.5	1.0	1.0
BH110 salt cylinder column	0.75	1.0	1.0
BH111 salt cylinder column	0.75	0.1	1.0
BH112 salt cylinder column	1.0	1.0	1.0
BH113 salt cylinder column	1.0	1.0	1.0
BH114 salt cylinder column	1.0	10.	20.

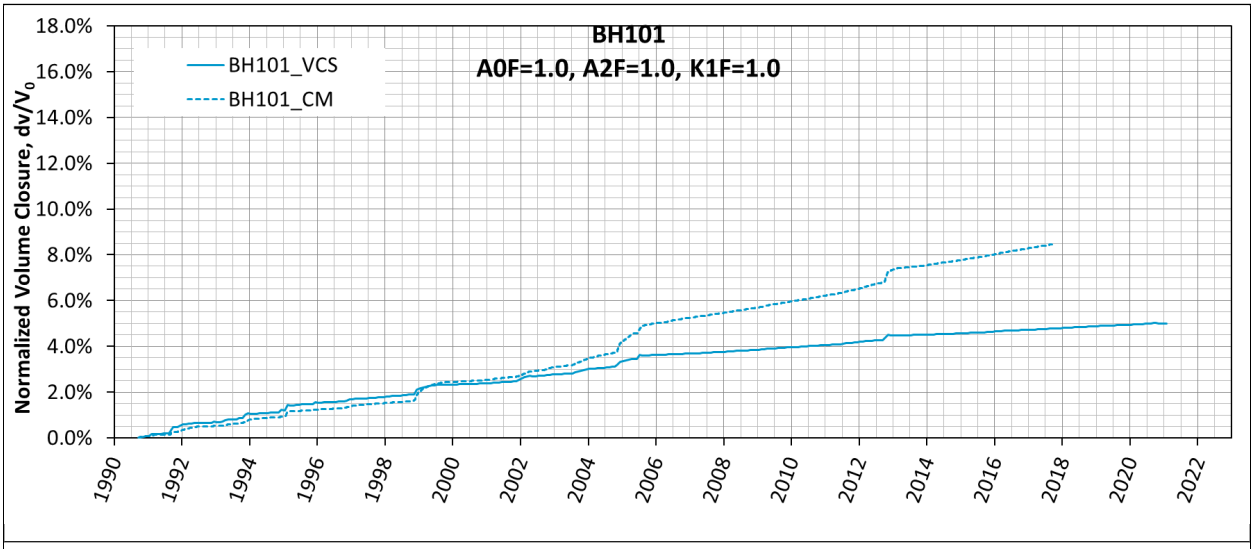

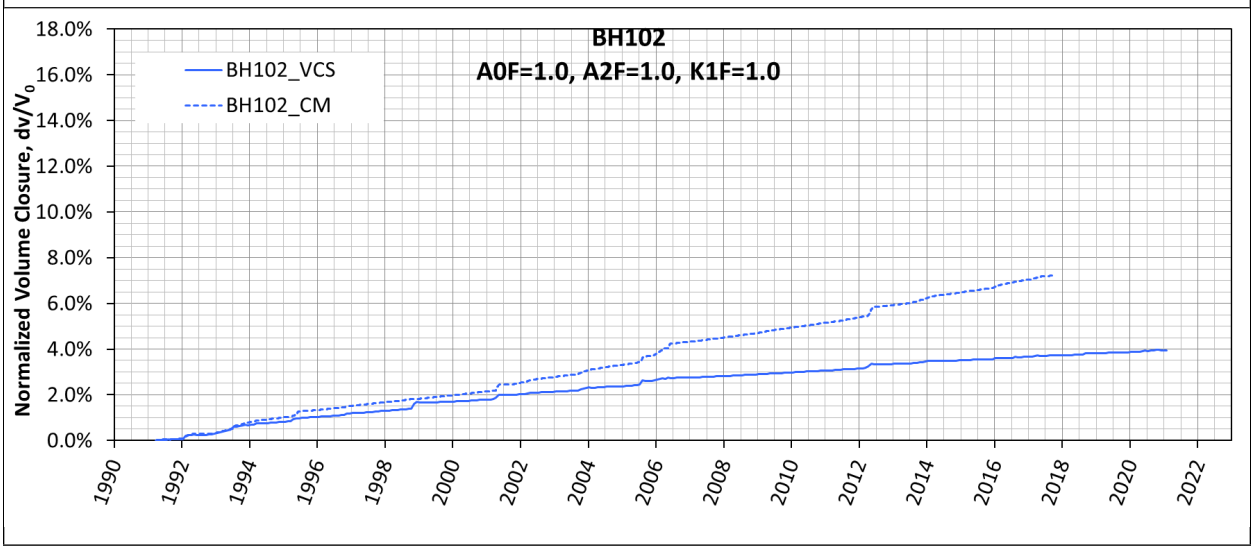

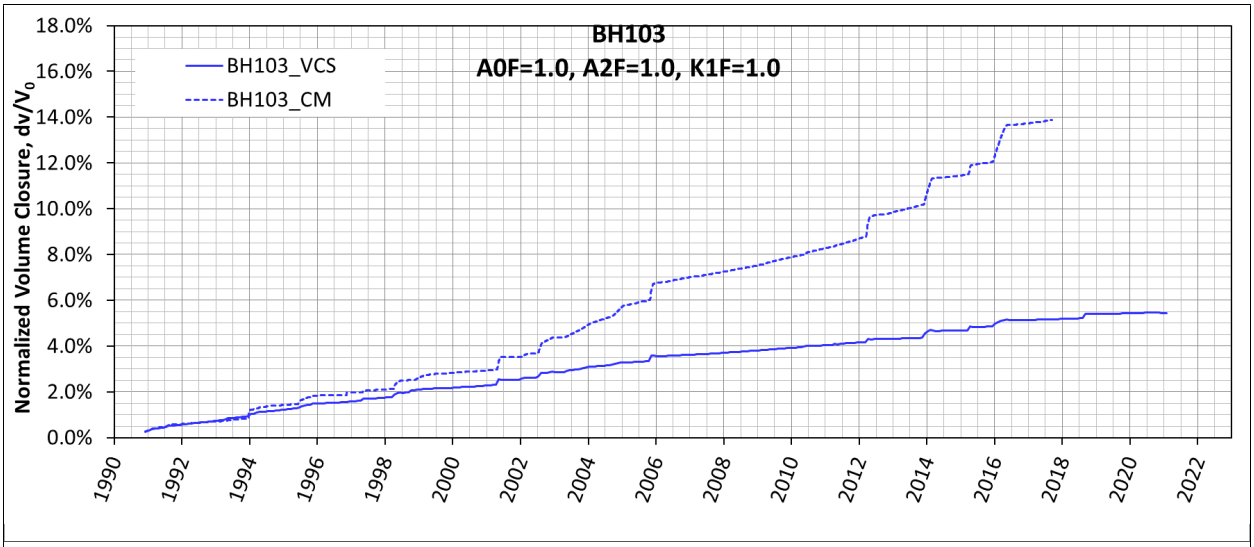
BH103
A0F=1.0, A2F=1.0, K1F=1.0
BH103_VCS
BH103_CM
Normalized Volume Closure, dv/V0
18.0%
16.0%
14.0%
12.0%
10.0%
8.0%
6.0%
4.0%
2.0%
0.0%
1990
1992
1994
1996
1998
2000
2002
2004
2006
2008
2010
2012
2014
2016
2018
2020
2022

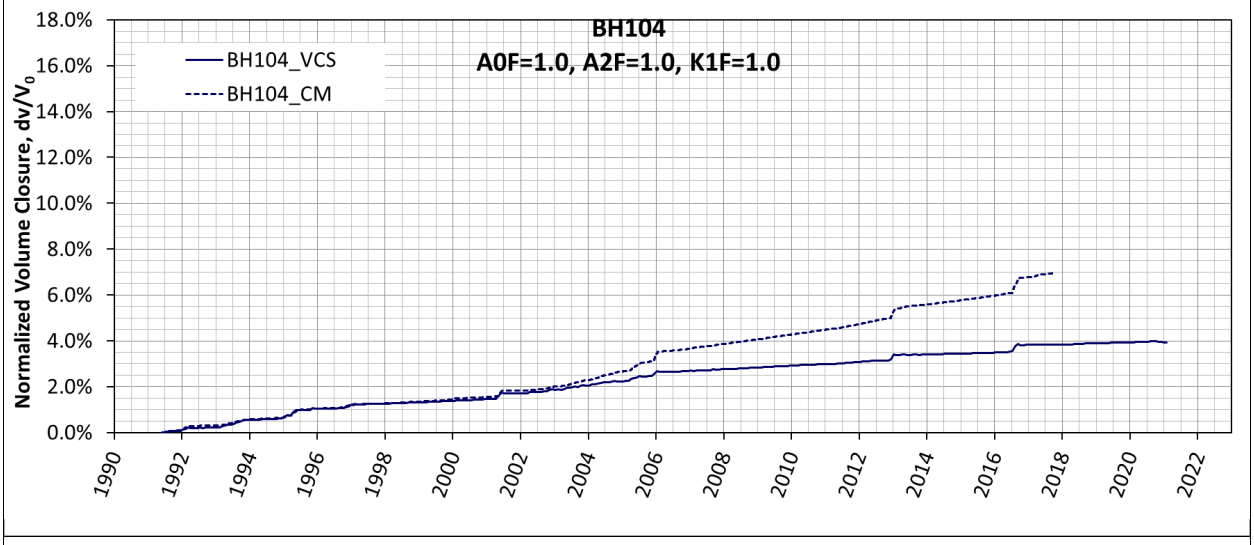
BH104
A0F=1.0, A2F=1.0, K1F=1.0
BH104_VCS
BH104_CM
Normalized Volume Closure, dv/V0
18.0%
16.0%
14.0%
12.0%
10.0%
8.0%
6.0%
4.0%
2.0%
0.0%
1990
1992
1994
1996
1998
2000
2002
2004
2006
2008
2010
2012
2014
2016
2018
2020
2022

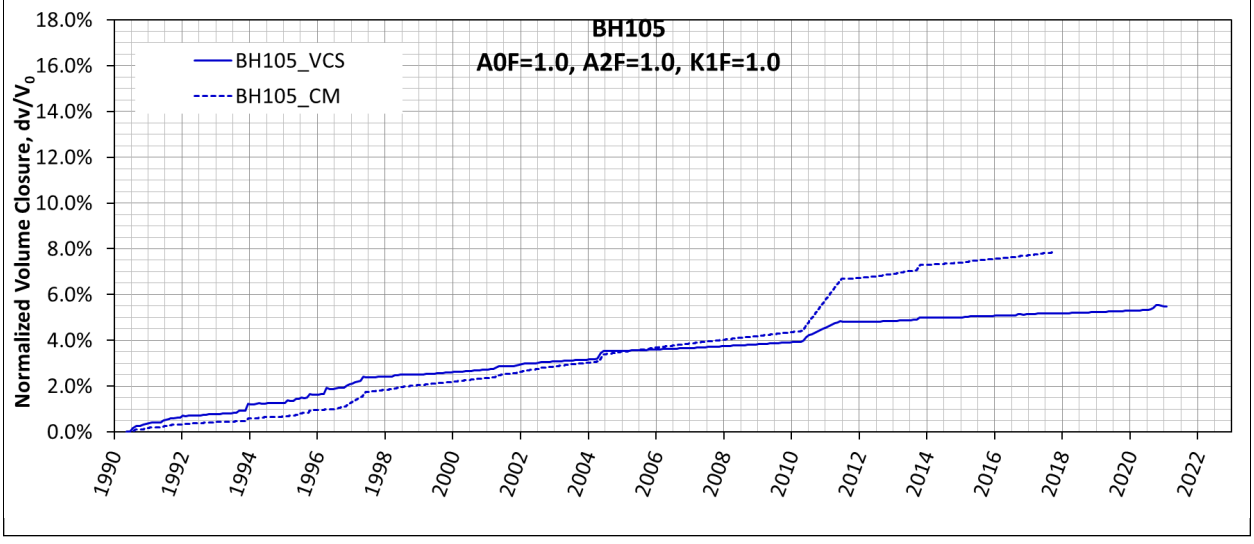
BH105
A0F=1.0, A2F=1.0, K1F=1.0
BH105_VCS
BH105_CM
Normalized Volume Closure, dv/V0
18.0%
16.0%
14.0%
12.0%
10.0%
8.0%
6.0%
4.0%
2.0%
0.0%
1990
1992
1994
1996
1998
2000
2002
2004
2006
2008
2010
2012
2014
2016
2018
2020
2022

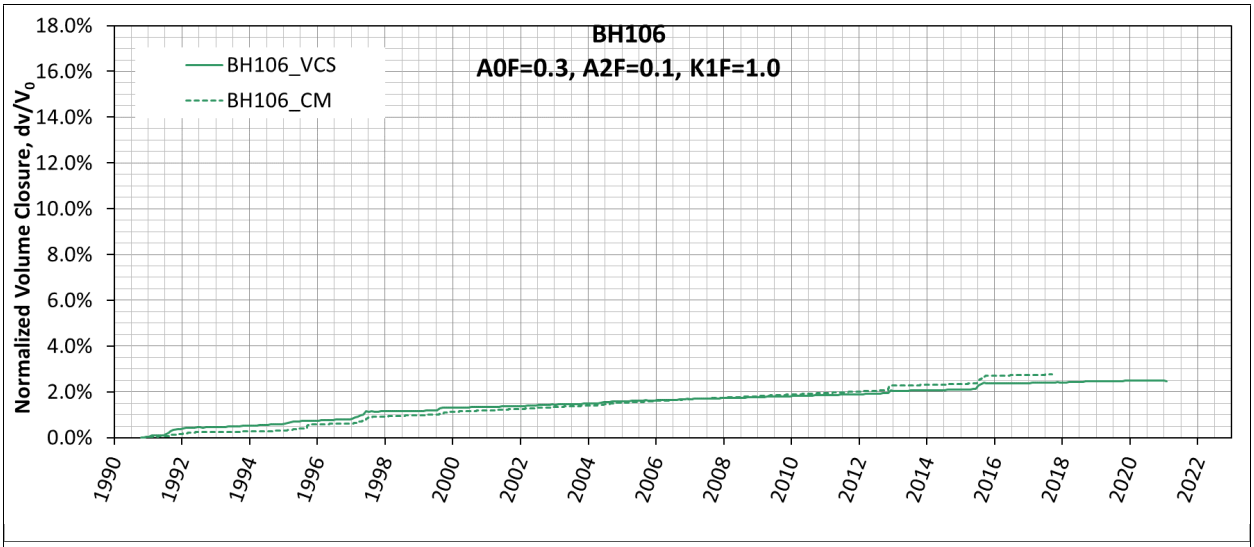
BH106
A0F=0.3, A2F=0.1, K1F=1.0
BH106_VCS
BH106_CM
Normalized Volume Closure, dv/V0
18.0%
16.0%
14.0%
12.0%
10.0%
8.0%
6.0%
4.0%
2.0%
0.0%
1990
1992
1994
1996
1998
2000
2002
2004
2006
2008
2010
2012
2014
2016
2018
2020
2022

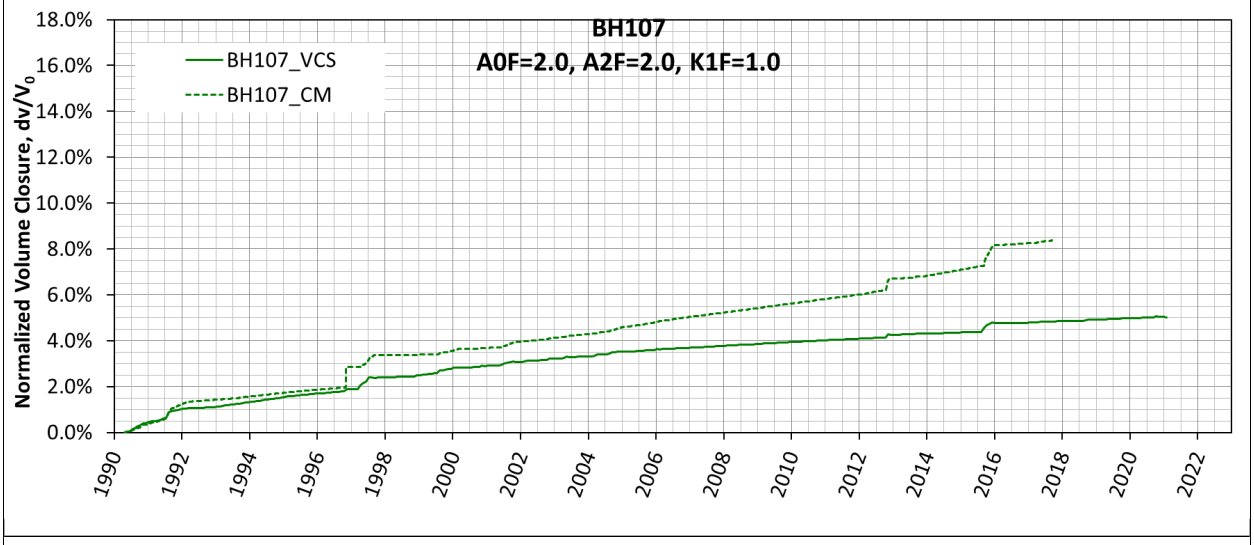
BH107
A0F=2.0, A2F=2.0, K1F=1.0
BH107_VCS
BH107_CM
Normalized Volume Closure, dv/V0
18.0%
16.0%
14.0%
12.0%
10.0%
8.0%
6.0%
4.0%
2.0%
0.0%
1990
1992
1994
1996
1998
2000
2002
2004
2006
2008
2010
2012
2014
2016
2018
2020
2022

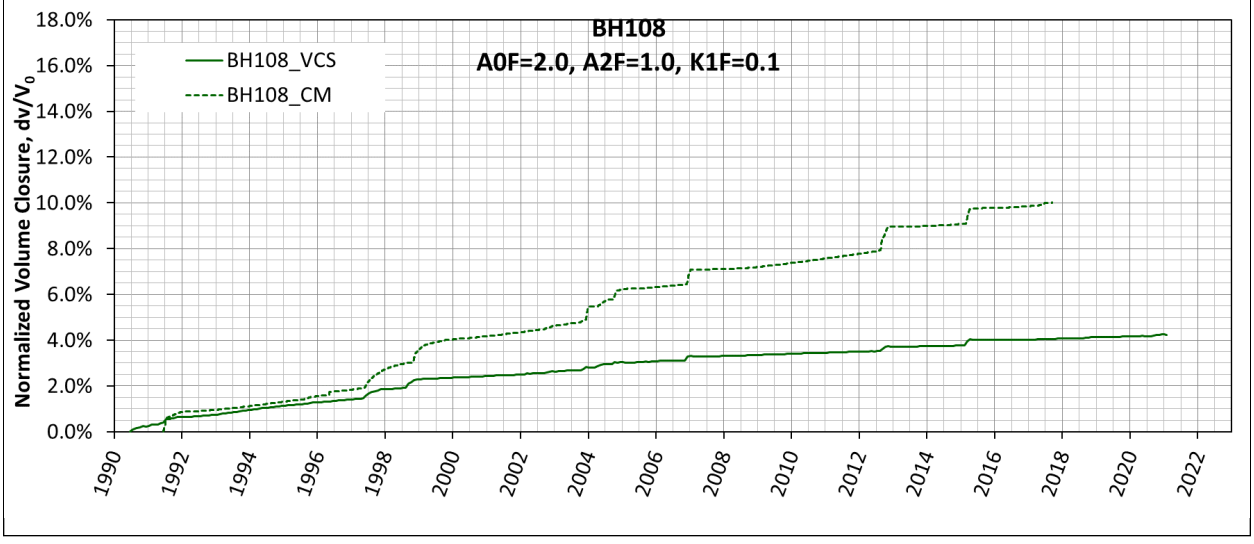
BH108
A0F=2.0, A2F=1.0, K1F=0.1
BH108_VCS
BH108_CM
Normalized Volume Closure, dv/V0
18.0%
16.0%
14.0%
12.0%
10.0%
8.0%
6.0%
4.0%
2.0%
0.0%
1990
1992
1994
1996
1998
2000
2002
2004
2006
2008
2010
2012
2014
2016
2018
2020
2022

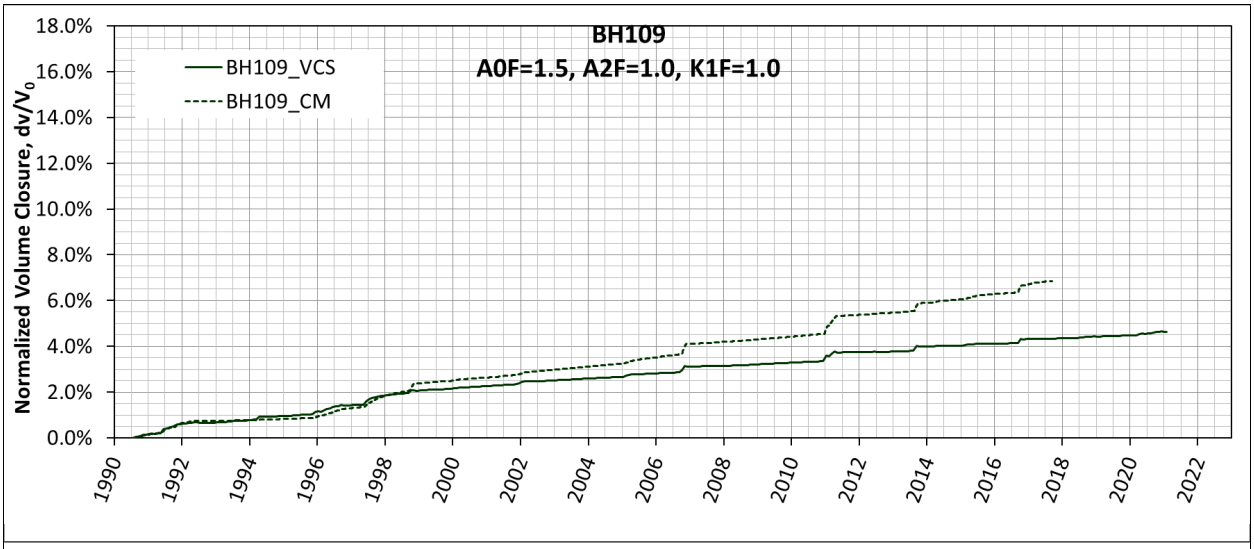
BH109
A0F=1.5, A2F=1.0, K1F=1.0
BH109_VCS
BH109_CM
Normalized Volume Closure, dv/V0
18.0%
16.0%
14.0%
12.0%
10.0%
8.0%
6.0%
4.0%
2.0%
0.0%
1990
1992
1994
1996
1998
2000
2002
2004
2006
2008
2010
2012
2014
2016
2018
2020
2022

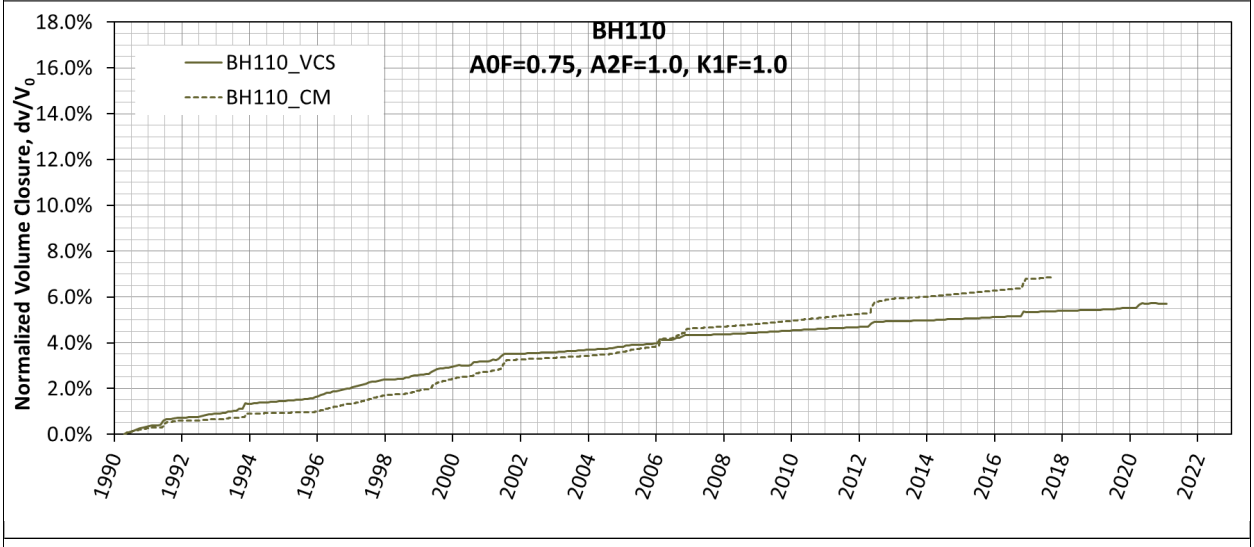
BH110
A0F=0.75, A2F=1.0, K1F=1.0
BH110_VCS
BH110_CM
Normalized Volume Closure, dv/V0
18.0%
16.0%
14.0%
12.0%
10.0%
8.0%
6.0%
4.0%
2.0%
0.0%
1990
1992
1994
1996
1998
2000
2002
2004
2006
2008
2010
2012
2014
2016
2018
2020
2022

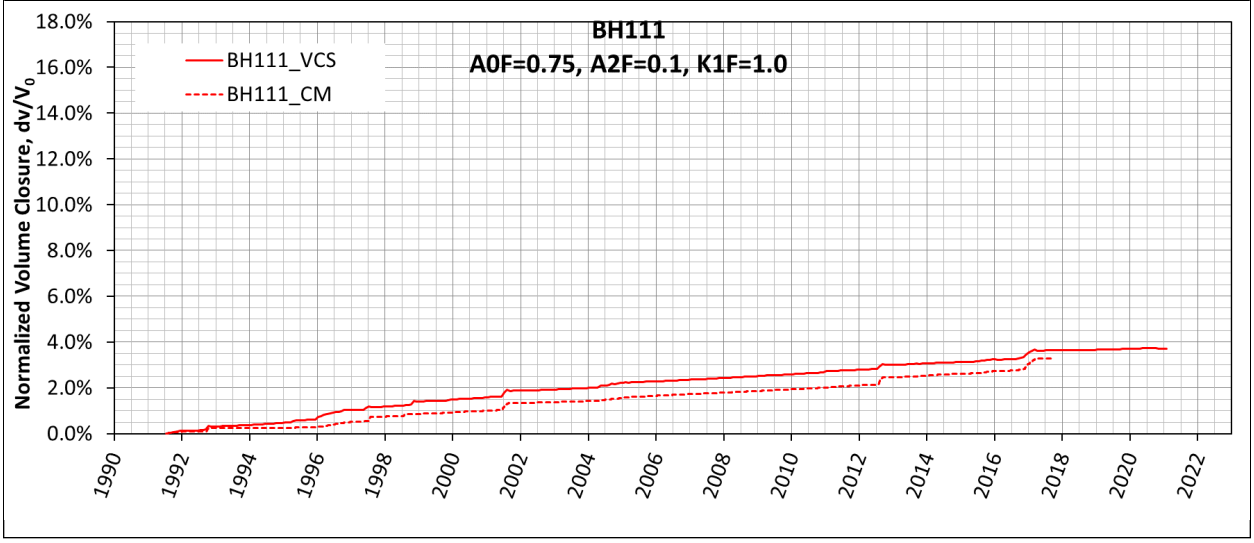
BH111
A0F=0.75, A2F=0.1, K1F=1.0
BH111_VCS
BH111_CM
Normalized Volume Closure, dv/V0
18.0%
16.0%
14.0%
12.0%
10.0%
8.0%
6.0%
4.0%
2.0%
0.0%
1990
1992
1994
1996
1998
2000
2002
2004
2006
2008
2010
2012
2014
2016
2018
2020
2022

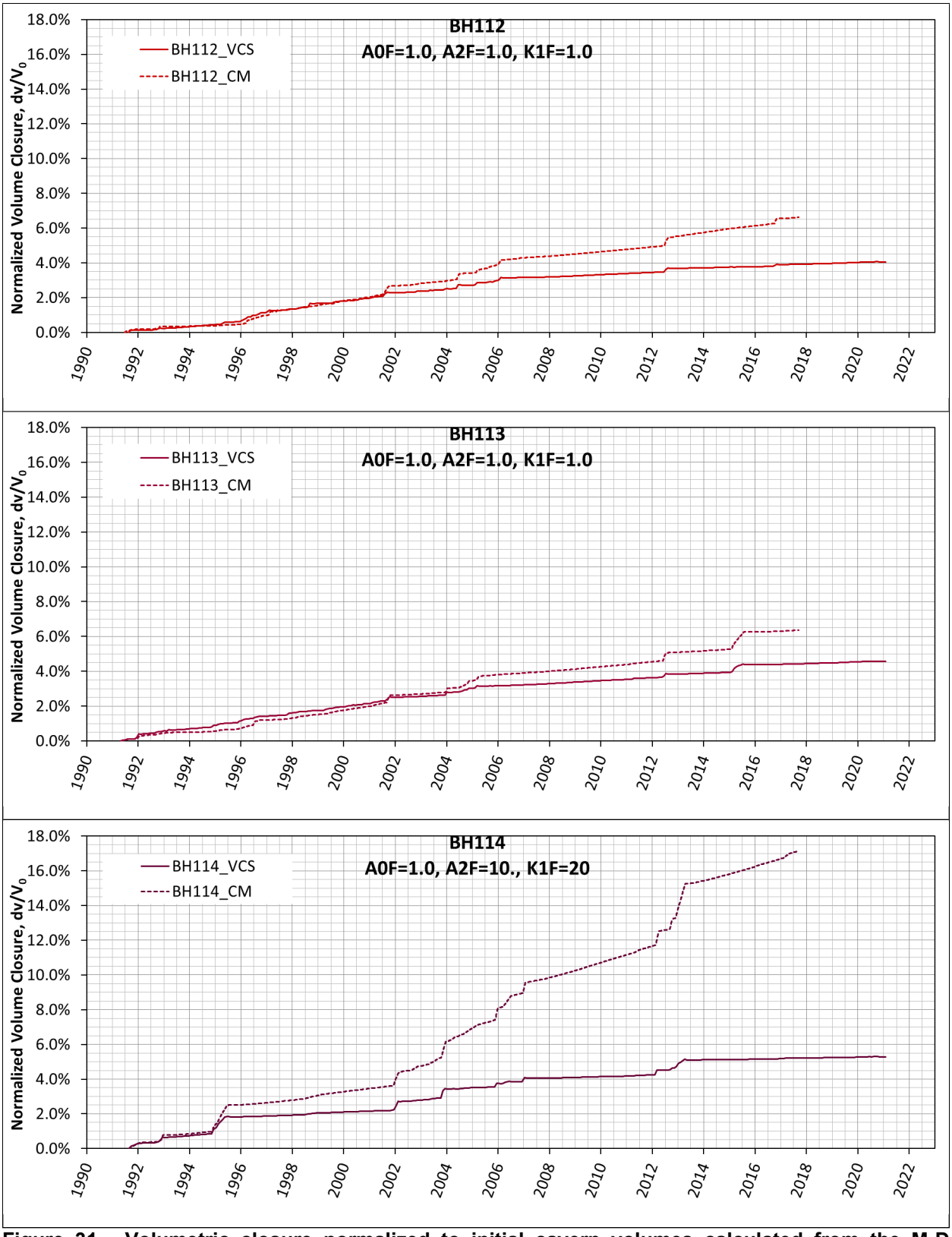

Figure 31. Volumetric closure normalized to initial cavern volumes calculated from the M-D viscoplastic contact surface model (VCS) using calibrated *A0F*, *A2F* and *K1F* in Table 7, and Caveman (CM) predictions for 14 SPR caverns

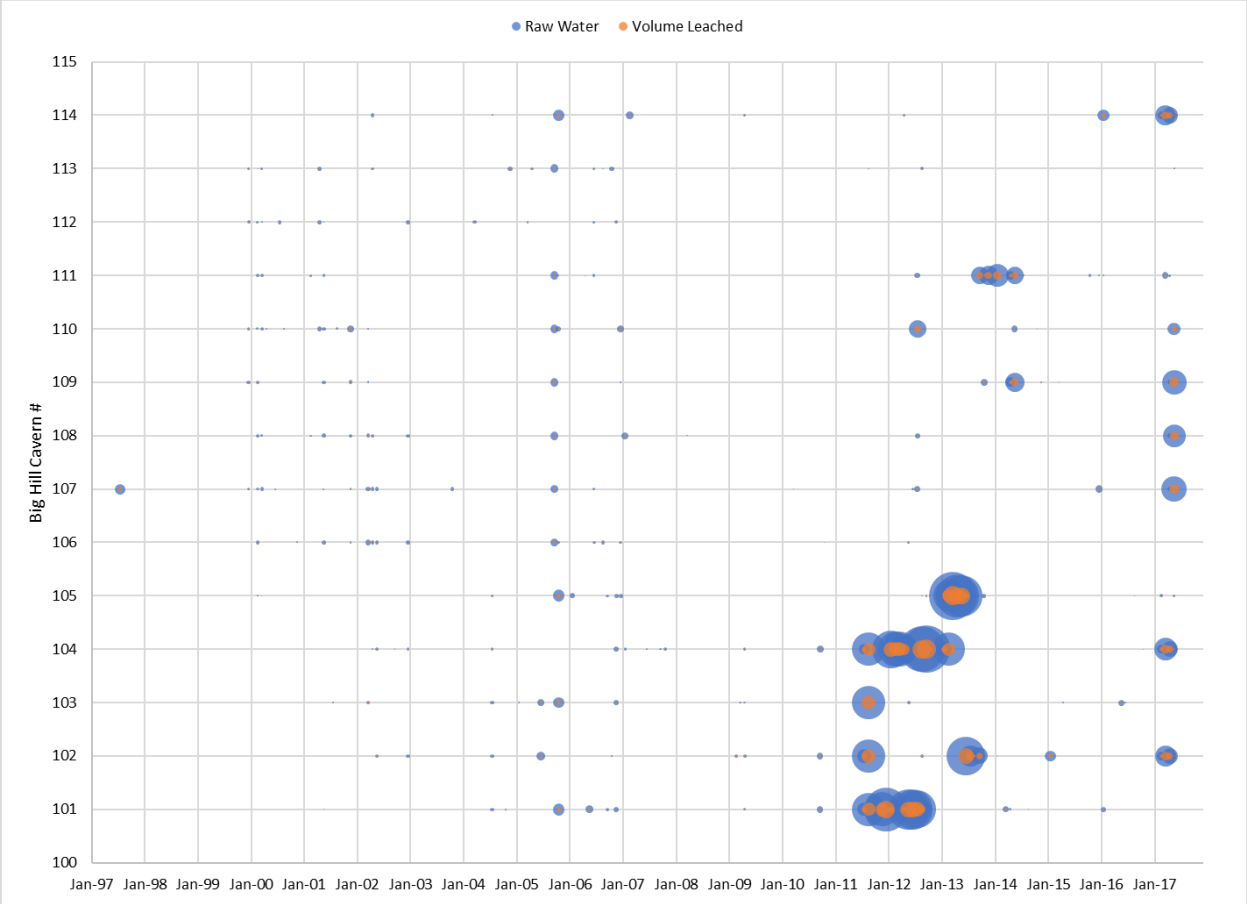

Figure 32. Month-by-month raw water movements in the Big Hill SPR caverns from 1997 to 9/29/2017 [Hart, 2018].

This page left blank

8. SUMMARY AND DISCUSSIONS

This simulation uses the multi-mechanism deformation viscoplastic model as a salt constitutive model. The original M-D model considers three separate steady-state creep mechanisms and an overlying transient creep mechanism. Recent efforts by Reedlunn and others have resulted in some new understandings of steady-state creep, particularly at low stress states. This work has resulted in an upgrade to the M-D model in Adagio that is called the M-D viscoplastic model.

The BH site has a shear zone that is important to the geomechanical behavior of the system. Modeling approaches to simulate the behavior of this shear zone, as well as the behavior of the horizontally oriented plane between caprock and salt dome, have evolved through several approaches. This study describes how the new contact surface model was applied to the BH slippage planes.

The M-D viscoplastic contact surface (VCS) model, which uses the M-D viscoplastic constitute model for the salt and the mesh containing the interbed layer with contact surfaces between the salt and caprock layers, and fault blocks in overburden and caprock layers, is used in this study. In most caverns, the volumetric closures calculated from the VCS model match the Caveman (CM)'s better than the original M-D model's. This might be because the VCS model uses the steady-state creep at low stress states, and the sliding mechanism between the caprock and salt, and fault blocks.

However, the results for BH106, BH107, BH108, BH111, and BH114 do not agree well. Therefore, the calibration of the parameter values is needed to match the simulation model to the field environment. The structure factor A_0, A_2, and transient strain limit factor, K_1 in the M-D viscoplastic constitutive model are used for the calibration. To adjust the magnitude of A_0, A_2, and K_1, multiplication factors *A0F*, *A2F* and *K1F* are defined. The relationships between each cavern volumetric closure rates and *A0F*, *A2F*, and *K1F* are determined.

The values of *A0F*, *A2F* and *K0F* have been calibrated through several back-fitting analyses and determined. In all caverns except BH114, the volumetric closures calculated from the VCS model and CM agree well from 1991, when the caverns began operating, to the early 2000s. But after that, the difference starts to widen. CM's results show that the slope of volumetric closure tends to increase during 2000's compared to them during 1990's.

According to the record of raw water injection into each cavern, the injected amount was not very large by 2005, so there is little change in the volume of the caverns that were leached by the injected raw water. Therefore, it seems to the volumetric closure results up to the early 2000s in most caverns are in good match to CM's results. It may have contributed to the increase in the slope of the CM curve due to the volume of the caverns increased as the raw water injection amount was increased afterwards. However, the amount of injected water does not match the slope increase in normalized cavern closure in the same proportion.

One of the issues we are going to have that will make it difficult to compare Caveman and Adagio is that they do different things. Adagio uses either historic or user-specified pressures on the interior surface of the cavern and tests the salt reaction to that. Caveman tries to calculate the increased pressure on the fluid due to salt creep and fluid compressibility to calculate the change in volume in daily increments. Furthermore, whenever a fluid exchange is entered into Caveman, the overall volume of the cavern is changed by that amount; in the case of raw water, an additional 15% of the water volume is added to the cavern. This happens on a "daily" basis in the program. In Adagio, the cavern volume is increased only when a predesigned, meshed block of salt is removed from the calculation. It is not surprising that there is going to be greater discrepancy between Caveman and Adagio during times of frequent fluid movement and raw water injection.

In conclusion, Cavemen's calculation results could not be consistent with those from the BH geomechanical model. However, it could be used as a reference for examining the calculation results of the model. Since the simulation results up to the early 2000s agree well with Cavemen's results, the results calculated from this model could be used to examine the structural integrity of caverns in BH dome.

REFERENCES

Ballard, S. and Ehgartner, B.L. (2000). *Caveman Version 3.0: System for SPR Cavern Pressure Analysis,* SAND2000-1751, Sandia National Laboratories, Albuquerque, NM 87185-0750.

Bérest, P., Béraud, J. F., Gharbi, H., Brouard, B., and DeVries, K. (2015). "A very slow creep test on an Avery Island salt sample". In: *Rock Mechanics and Rock Engineering* 48.6, pp. 2591–2602.

Bérest, P., Blum, P. A., Charpentier, J. P., Gharbi, H., and Valès, F. (2005). "Very slow creep tests on rock samples". In: *International Journal of Rock Mechanics and Mining Sciences* 42.4, pp. 569–576.

Butcher, B.M. (1997). *A Summary of the Sources of Input Parameter Values for the WIPP Final Porosity Surface Calculations*, SAND97-0796, Albuquerque, NM: Sandia National Laboratories.

Düsterloh, U., Herchen, K., Lux, K.-H., Salzer, K., Günther, R.-M., Minkley, W., Hampel, A., Argüello Jr, J. G., and Hansen, F. D. (2015). "Joint Project III on the comparison of constitutive models for the thermomechanical behavior of rock salt. III. Extensive laboratory test program with argillaceous salt from WIPP and comparison of test results". In: *Proc. 8th Conference on the Mechanical Behavior of Salt*. Ed. by L. Roberts, K. D. Mellegard, and F. D. Hansen, pp. 13–21.

Ehgartner, B., S. Ballard, M. Tavares, S. Yeh, T. Hinkebein, and R. Ostensen. (1995). *A Predictive Model for Pressurization of SPR Caverns,* Fall Meeting Solution Mining Research Institute, October 23-24, San Antonio, TX

Ehgartner, B.L. and Bauer, S. (2004), *Large Scale Salt Deformation: Comments on Subsidence using thermal, creep and Dissolution modeling to assess volumetric strain*, SAND2004-0095C, Sandia National Laboratories, Albuquerque, NM 87185.

Hansen, F. D. (2014). Micromechanics of Isochoric Salt Deformation. In: *48th US Rock Mechanics/Geomechanics Symposium*. American Rock Mechanics Association.

Hart, D.B. (2018). *Month-by-month raw water movements from 1997 to 9/29/2017*, e-mail to B.Y. Park on 7/18/2018, Excel spread sheets, Sandia National Laboratories, Albuquerque, New Mexico.

Hoffman, E.L. and Ehgartner, B.L. (1992). *Evaluating the Effects of the Number of Caverns on the Performance of Underground Oil Storage Facilities,* SAND92-2183C, Sandia National Laboratories, Albuquerque, New Mexico.

Hogan, R.G. (1980). *Strategic Petroleum Reserve (SPR) Geological Site Characterization Report Bayou Choctaw Salt Dome,* SAND80-7140, Sandia National Laboratories, Albuquerque, New Mexico.

Hosford, W. (1972). A generalized isotropic yield criterion. In: *Journal of Applied Mechanics*, 39.2, pp. 607–609.

Lama, R.D. and V.S. Vutukuri (1978). *Handbook on Mechanical Properties of Rocks – Testing Techniques and Results*, Series on Rock and Soil Mechanics, Vol. 3, No.2, Trans Tech Publications.

Linn J.K. (1997). Memorandum to R.E. Myers, November 25, 1997 with attachment on *SPR Ullage Study* by B.L. Ehgartner, Sandia National Laboratories, Albuquerque, New Mexico.

Magorian, T.R., and J.T. Neal (1988). *Strategic Petroleum Reserve (SPR) Additional Geologic Site Characterization Studies Big Hill Salt Dome*, Texas, SAND88-2267, Sandia National Laboratories, Albuquerque, NM.

Munson, D.E. and P.R. Dawson. (1982). *A Transient Creep Model for Salt during Stress Loading and Unloading.* SAND82-0962, Sandia National Laboratories, Albuquerque, New Mexico.

Munson, D.E., A.F. Fossum, and P.E. Senseny. (1989). *Advances in Resolution of Discrepancies between Predicted and Measured in Situ WIPP Room Closures.* SAND88-2948, Sandia National Laboratories, Albuquerque, New Mexico.

Munson, D.E., (1998). *Analysis of Multistage and Other Creep Data for Domal Salts,* SAND98-2276, Sandia National Laboratories, Albuquerque, New Mexico.

Park, B.Y., B.L. Ehgartner, M.Y. Lee, and S.R. Sobolik. (2005). *Three Dimensional Simulation for Big Hill Strategic Petroleum Reserve (SPR)*, SAND2005-3216, Sandia National Laboratories, Albuquerque, NM.

Park, B.Y. and B.L. Ehgartner. (2012). *Interface Modeling to Predict Well Casing Damage for Big Hill Strategic Petroleum Reserve*, SAND2012-1206, Sandia National Laboratories, Albuquerque, New Mexico.

Park, B.Y. (2014a). Interbed Modeling to Predict Wellbore Damage for Big Hill Strategic Petroleum Reserve. *Journal of Rock Mech Rock Eng (2014) 47:1551-1561.* DOI 10.1007/s00603-014-0572-2

Park, B.Y. (2014b). *Geomechanical Analysis to Predict the Oil Leak at the Wellbores in Big Hill Strategic Petroleum Reserve*, SAND2014-0669, Sandia National Laboratories, Albuquerque, NM.

Park, B.Y., Sobolik, S.R., & Herrick, C.G. (2014). Wellbore Deformations and Proposed Steel Casing Size for Remediation in Big Hill Strategic Petroleum Reserve. SAND 2014-1846 C, *Rock Mechanics for Natural Resources and Infrastructure, SBMR 2014 – ISRM Specialized Conference 09-13 September, Goiania, Brazil.* © CBMR/ABMS and ISRM, 2014.

Park, B.Y. and B.L. Roberts, (2015). *Construction of Hexahedral Elements Mesh Capturing Realistic Geometries of Bayou Choctaw SPR site,* SAND2015-7458, Sandia National Laboratories, Albuquerque, New Mexico.

Park, B.Y. (2017). *Geomechanical Simulation of Bayou Choctaw Strategic Petroleum Reserve - Model Calibration,* SAND2017-2103, Sandia National Laboratories, Albuquerque, New Mexico.

Park, B. Y., S.R. Sobolik, and C.G. Herrick. (2018). Geomechanical Model Calibration Using Field Measurements for a Petroleum Reserve. *Journal of Rock Mechanics and Rock Engineering,* ISSN 0723-2632, https://doi.org/10.1007/s00603-017-1370-4

Park, B.Y. (2018). *Geomechanical Simulation of Big Hill Strategic Petroleum Reserve - Model Calibration,* SAND2018-13783, Sandia National Laboratories, Albuquerque, New Mexico.

Park, B.Y. (2019). *Geomechanical Simulation of Big Hill Strategic Petroleum Reserve - Calibration of Model Containing Shear Zone*, SAND2019-11696, Sandia National Laboratories, Albuquerque, New Mexico.

Park, B.Y. (2020). *Geomechanical Analysis Using M-D Viscoplastic Material Model – Big Hill*, Letter to Diane Willard, DOE-SPR on 7/31/2020, Sandia National Laboratories, Albuquerque, New Mexico.

Park, B.Y. (2021). *Milestone 1.2a1: Apply contact surface module into BH model*, Letter report to Diane Willard, DOE-SPR, dated 9/30/2021, Sandia National Laboratories, Albuquerque, New Mexico.

Reedlunn, B. (2016). *Reinvestigation into Closure Predictions of Room D at the Waste Isolation Pilot Plant*. Tech. rep. SAND2016-9961. Albuquerque, NM, USA: Sandia National Laboratories. doi: 10.2172/1333709.

Reedlunn, B. (2018). *Enhancements to the Munson-Dawson Model for Rock Salt*, SAND2018-12601, Sandia National Laboratories, Albuquerque, New Mexico.

Reedlunn, B., Arguello, J.G., and Hansen, F.D. (2021). A reinvestigation into Munson's model for room closure in bedded rock salt, *International Journal of Rock Mechanics & Mining Sciences* 151 (2022) 105007. https://doi.org/10.1016/j.ijrmms.2021.105007 .

Salzer, K., Günther, R.-M., Minkley, W., Naumann, D., Popp, T., Hampel, A., Lux, K.-H., Herchen, K., Düsterloh, U., Argüello Jr, J. G., and Hansen, F. D. (2015). "Joint Project III on the comparison of constitutive models for the thermomechanical behavior of rock salt. III. Extensive laboratory test program with clean salt from WIPP". BGR (Federal Institute for Geosciences and Natural Resources). isbn: 978-3-9814108-6-0. In: *Proc. 8th Conference on the Mechanical Behavior of Salt*. Ed. by L. Roberts, K. D. Mellegard, and F. D. Hansen, pp. 3–12.

Sobolik, S.R. (2015). *Analysis of Cavern and Well Stability at the West Hackberry SPR Site Using a Full-Dome Model,* SAND2015-7401, and Sandia National Laboratories, Albuquerque, New Mexico.

Sobolik, S.R. (2020). *FY20 Milestone 1.4d1: Impact of Cavern Roof Shape on Salt Stress*, Letter report to Diane Willard, DOE-SPR, dated October 12, 2020, Albuquerque, New Mexico.

Wawersik W. R. (1985). Memorandum to R.R. Beasley, January 3, 1985, *Creep Measurements on Big Hill Salt*, Sandia National Laboratories, Albuquerque, NM.

This page left blank

DISTRIBUTION

Email—Internal

Name	Org.	Sandia Email Address
Benjamin K. Cook	8910	bkcook@sandia.gov
Kyung Won Chang	8912	kchang@sandia.gov
Donald M. Conley	8912	dconley@sandia.gov
David Hart	8912	dbhart@sandia.gov
Joseph Hogge	8912	jhgge@sandia.gov
Carolyn L. Kirby	8912	clkirby@sandia.gov
Anna C. Snider Lord	8912	acsnide@sandia.gov
David Lord	8912	dllord@sandia.gov
Dylan Michael Moriarty	8912	dmmoria@sandia.gov
Barry L. Roberts	8912	blrober@sandia.gov
Tonya S. A. Ross	8912	tsross@sandia.gov
Steven R. Sobolik	8912	srsobol@sandia.gov
Todd Zeitler	8912	tzeitle@sandia.gov
Technical Library	1911	sanddocs@sandia.gov

Email—External

Name	Company Email Address	Company Name
Wayne Elias	wayne.elias@hq.doe.gov	U.S. Department of Energy Office of Fossil Energy Washington, DC
Diane Willard	diane.willard@spr.doe.gov	U.S. Department of Energy SPR Project Management Office New Orleans, LA

Hardcopy—Internal

Number of Copies	Name	Org.	Mailstop
5	Carolyn L. Kirby	8862	MS0750
3	Byoung Y. Park	8862	MS0751

This page left blank

Sandia National Laboratories is a multimission laboratory managed and operated by National Technology & Engineering Solutions of Sandia LLC, a wholly owned subsidiary of Honeywell International Inc. for the U.S. Department of Energy's National Nuclear Security Administration under contract DE-NA0003525.